THE STUDY OF PERPENDICULARLY MAGNETIZED CoFe/Pd MULTILAYERS FOR DOMAIN WALL MOTION

MENG ZHAOLIANG

(B. ENG. (HONS), HUAZHONG UNIVERSITY OF SCIENCE AND TECHNOLOGY)

A THESIS SUBMITTED

FOR THE DEGREE OF DOCTOR OF PHILOSOPHY

DEPARTMENT OF ELECTRICAL AND COMPUTER ENGINEERING

NATIONAL UNVERSITY OF SINGAPORE

2016

DECLARATION

I hereby declare that the thesis is my original work and it has been written by me in its entirely. I have duly acknowledged all the sources of information which have been used in this thesis.

This thesis has also not been submitted for any degree in any university previously.

MENG ZHAOLIANG

08 March 2016

ACKNOWLEDGEMENTS

I would like to have this chance to thank all the persons who helped me in many ways during my Ph.D periods**.** First of all, I would like to express my utmost gratitude to my supervisor Professor Teo Kie Leong and my mentor Dr. Han Guchang for providing me this precious opportunity to engage into the field of academic research. I am really grateful for their continuous guidance, support, patience and encouragement throughout the last five years of my Ph.D candidate.

I also would like to thank my co-supervisor Dr. Qiu jinjun for his continued support, encouragement and experimental assistance. I would like to extend my gratitude to Dr. He Shikun for teaching me the art of the scientific research and accompanying with me for the research experiments. I am grateful to Zhang Lijuan for guiding me the skill of the scientific writing with patience and encouragement. I also cherish the moments with my seniors Dr. Zheng Yuhong, Dr. Ryan, Dr. Manoj, Dr. Ren Lizhu, Dr. Lu Hui, Dr. Yupu and my colleagues Qijia, Liu Yifan for the fruitful discussion and entertainment in the lab, which made the research much more enjoyable. I would like to extend my thanks to each member of in Advanced Memory Lab and Data Storage Institute (DSI) for their technical and domestic support to my Ph.D project.

Finally, I would like to thank my family for their kind understanding, love, support and blessings over these years.

TABLE OF CONTENTS

SUMMARY

Co-based multilayers with perpendicular magnetic anisotropy (PMA) have been intensively studied due to their potential application in domain wall (DW) based devices for the next generation memories and logic systems. We focus the studies of DW motion in a CoFe/Pd multilayer-based nanowire with strong PMA. Firstly, we investigate the magnetic properties of CoFe/Pd multilayers deposited by sputtering technique. Our results show that high PMA, low saturation magnetization (M_s), narrow DW width (λ) and high spin polarization (P) can induce low threshold current density (J_{th}) for DW motion in CoFe/Pd superlattice-like multilayer films. Next, we fabricate the DW-based nanowires using the CoFe/Pd multilayers and study the DW motion. We show that DW motion can be driven by a low J_{th} with small bias field. The combination of non-adiabatic spin-transfer-torque and the spin orbit torque is found to be the main contribution to the current induced DW motion. Secondly, we study the magnetization reversal and magnetic interlayer coupling in CoFe/Pd superlattice-based synthetically antiferromagnetic (SAF) structure. Our results indicate that a large exchange coupling field can be achieved at room temperature and exhibit a strong dependence on the annealing temperature. We further fabricate the perpendicularly magnetized nanowires based on the CoFe/Pd superlattice-based SAF structure. The J_{th} and DW velocity (v) are then systematically studied. A minimum J_{th} = 9.2×10^{10} A/m^2 and a maximum v = 150 m/s under a driving current density J = 1.5×10^{12} A/m^2 for DW motion are observed, which can be attributed to the exchange

coupling torque (ECT) generated in the SAF structure. The strength of ECT is dependent on both of J_{ex} and the strong spin-orbit torque mainly generated by the Ta layer. Our findings pose challenges as well as opportunities for future studies of CoFe/Pd multilayer for DW-based devices.

LIST OF TABLES

LIST OF FIGURES

LIST OF PUBLICATIONS

[1]. **Z. L. Meng**, S. K. He, L. S. Huang, J. J. Qiu, T. J. Zhou, C. Panagopoulos, G. C. Han and K. L. Teo, "Current induced domain wall motion in antiferromagnetically coupled ($Co_{70}Fe_{30}$/Pd) multilayer nanowires", *Appl. Phys.Lett.* **109**, 142403 (2016).

[2]. **Z. L. Meng**, S. K. He, J. J. Qiu, T. J. Zhou, G. C. Han and K. L. Teo, "Domain wall motion in ultrathin $Co_{70}Fe_{30}$/Pd multilayer nanowires with perpendicular anisotropy", *J. Appl. Phys.* **119**, 083905 (2016).

[3]. **Z. L. Meng,** J. J. Qiu, G. C. Han and K. L. Teo, "Enhanced interlayer exchange coupling in antiferromagnetically coupled ultrathin ($Co_{70}Fe_{30}$/Pd) multilayers", *J. Appl. Phys.* **118**, 243903 (2015).

[4]. **Z. L. Meng**, D. T. Ngo, M. Kumar, J. J. Qiu, G. C. Han and K. L. Teo, "Domain wall motions in perpendicularly magnetized CoFe/Pd multilayer nanowire" *J. Phys. D: Appl. Phys.* **47**, 345001 (2014).

[5]. D. T. Ngo, **Z. L. Meng**, T. Tahmasebi, X. Yu, E. Theong, L. H. Yeo, A. Rusydi, G. C. Han and K. L. Teo, "Interfacial tuning of perpendicular magnetic anisotropy and spin magnetic moment in CoFe/Pd multilayers" *J. Magn. Magn. Mater.* **350**, 42 (2014).

[6]. J. J. Qiu, **Z. L. Meng**, Q. J. Yap, Y. Yang, N. L. Geok and G. C. Han, "Perpendicular magnetic anisotropy in face-centered cubic (111) $Co_{90}Fe_{10}$/Pt superlattices", *Magn. Lett, IEEE.* **6**, 1 (2015).

[7]. J. J. Qiu, **Z. L. Meng**, Y. Yang , J. F. Ying , Q. J. Yap and G. C. Han. "Effect of roughness on perpendicular magnetic anisotropy in $(Co_{90}Fe_{10}/Pt)_n$ superlattices", *AIP Advances*. **6**, 056123 (2016).

LIST OF CONFERENCES

Oral presentation

[1]. **Z. L. Meng**, J. J. Qiu, Y. Yang, J. F. Ying, Q. J. Yap and G. C. Han (2016): "Effect of roughness on perpendicular magnetic anisotropy in $(Co_{90}Fe_{10}/Pt)n$ superlattices", 13th Joint MMM/Intermag Conference, January 11-15, San Diego, California, USA.

[2]. **Z. L. Meng**, D. T. Ngo, M. Kumar, J. J. Qiu, G. C. Han and K. L. Teo (2014): "Control of domain wall motion by magnetic field and electric current in CoFe/Pd multilayer nanowires", Magnetics Symposium 2014, September 22-23, Singapore.

[3]. **Z. L. Meng**, D. T. Ngo and K. L. Teo (2013): "Perpendicularly magnetized CoFe/Pd multilayer films for spin-transfer torque applications", IEEE International Nanoelectronics Conference (INEC), 2-4 January, Singapore.

Poster presentation

[1]. **Z. L. Meng**, S. K. He, J. J. Qiu, T. J. Zhou, G. C. Han and K. L. Teo (2015): "Current induced domain wall motion in perpendicularly magnetized ultrathin $(Co_{70}Fe_{30}/Pd)_n$ nanowire", IEEE International Magnetics Conference May 11-15, Beijing, China.

[2]. **Z. L. Meng**, D. T. Ngo, M. Kumar, J. J. Qiu, G. C. Han and K. L. Teo (2013): "Domain wall motions in perpendicularly magnetized CoFe/Pd multilayer nanowire ", 58th MMM Conference, November 5-8, Denver, Colorado, USA.

[3]. **Z. L. Meng**, D. T. Ngo, T. Tahmasebi, G. C. Han and K. L. Teo (2013): "CoFe/Pd multilayer films with strong perpendicular magnetic anisotropy and modifiable magnetic properties", 12th Joint MMM/Intermag Conference, January 14-18, Chicago, Illinois, USA.

Chapter 1 Introduction

1.1 Background

1.1.1 Spintronics and their applications to storage devices

Nowadays, electronic devices immensely affect our lives either directly or indirectly from the electronic meter till billion-transistor powerful processors. In most electronic devices, the information is expressed using the existence or absence of electric charges as "1" and "0" in binary digits. As the technology has rapidly developed over the past half century, smaller and faster new devices appear in the technology market almost every day. However, with size of electrical devices being scaled down, the physical limits will prevent further development of the microelectronics industry with the size of individual bits approaching to the dimension of atoms. Therefore, intensive studies have been carried out to explore another property of the electron — spintronics (the abbreviation of spin based electronics), which is used to carry information through the spin of the electron [1].

The spin of the electron is the rotation of electrons around its axis. There are two types of spin; namely spinning clockwise and spinning counter-clockwise direction, which are defined as spin down and spin up, respectively. Electrons have spin of a sort in which their magnetic direction can point either “up” or “down”. As a result, different spin directions can be used to represent binary bites — ones and zeros in the field of data storage. The movement of spin can also carry information among devices

[2]. This shed a light on a new generation of memory altogether with traditional spin-dependent effect that arises from the interaction between the spin of electron and the local magnetization of material. In principle, manipulating spin is faster and requires less energy for the directional migration in comparison with charge by both external magnetic field and spin-polarized current. Another advantage of spin over charge is that spin exhibits longer coherence or relaxation time than the charge. This means that the spin can maintain its state for a long time, whereas the charge will easily destroy its stable state by scattering or colliding with defects, impurities or other charges. Therefore, the application of spintronics has the promising advantages for the microelectronic devices with non-volatility, higher capacity, lower power consumption and higher speed.

In magnetic materials, there is an unbalanced number of spin-up and spin-down electrons (it is spin-polarized) providing researchers an ideal platform to study the spin of the electron. Spintronic devices employ the magnetic material to utilize the spin of the charges and sometimes it is also called as magneto-electronic. The research on the transport of a spin-polarized current taking place in magnetic materials has provided us with our current enormous data storage capabilities on the spintronics based memory, such as hard disk drives (HDDs), which are integrated in almost every personal's life.

The HDDs are the two-dimensional storage devices, in which the directions of tiny magnetic regions in a magnetic thin films deposited on glass disk are used to store digital data. A mechanical recording head is placed a few nanometers above

these magnetic regions to read and write the data bits. As the size of the magnetic data bits being scaled down by around nine orders of magnitude, the very tiny magnetic region will result in the physical limits for writing and reading data bits. These problems are difficult or extremely expensive to solve, which dramatically suppress the improvement in the storage capacity of the magnetic disk. In order to further extend the storage capacity, a novel non-volatile memory — magnetic random access memory (MRAM) [3] has been proposed to replace the conventional static RAM and HDDs since 1990s. MRAM is a new type of spin based memory and its operation is based on creating and manipulating spin-polarized electrical currents [4]. MRAM has already been successfully commercialized with specially sensitive sensors of small magnetic fields capable of operating at ambient temperature and above.

The giant magneto-resistive (GMR) effect with the metallic spacer was discovered in 1988 [5]. The discovery of giant magneto-resistive (GMR) spin valve sensors has had an important impact on hard disk sensors [5-7]. The areal density of the hard disk increases up to 10 times in a short span of time [8]. Current is spin-polarized when flowing through the spin valve due to the spin dependent diffusive scattering and spin dependent quantum mechanical tunneling for the respective metallic and insulating spacers. For insulating spacer layers, these magneto-resistive sensors are generally regarded as magnetic tunnel junctions (MTJs). The Al_2O_3-based MTJ is developed in 1991 [9] as well as MgO-based MTJ is evolved at beginning of the 21st century [10]. These MTJs enabled the most recent

improvements in the storage capacity of magnetic disk drives by making it possible to shrink the magnetic bit area by a factor of 1,000 [8].

In 1995, MTJs are firstly proposed to work as magnetic memory cells in MRAMs [11]. In 1999, a first MTJ-based MRAM device is successfully fabricated [12]. MRAM is the promising candidate for high-speed and high storage-density non-volatile memory but it also shows a number of disadvantages such as many fabrication steps, which is a major obstacle with the size of memory cell being scaled down below 10 nm because of thermal stability. In order to overcome these obstacles, racetrack memory based on the current induced domain wall motion [13] has been recently proposed to make a new generation of non-volatile memory with high speed and high capacity.

1.1.2 Magnetic domain walls

Weiss predicted the existence of magnetic domain in ferromagnets and proposed the concept of magnetic domain in 1906 [14]. Magnetic domains are tiny regions in which all the microscopic magnetic moments are aligned parallel to each other. In ferromagnetic materials, magnetic domains are randomly distributed, and the net magnetization is the sum over all magnetization of domains.

In magnetism, domain walls (DWs) are boundaries in magnetic materials to separate the magnetic domains with diverse directions of magnetization. DWs have been intensively studied for many years because of its significant role in magnetization reversal process of magnetic bulk and thin film materials.

In ferromagnetic materials, the exchange energy prefers a DW with wide width, while the magneto-crystalline anisotropy energy favors a narrow DW width. The exact DW width is a compromise of these two competing energies. For a 180° DW, the DW width is expressed by,

$$\lambda = \pi\sqrt{A/K} \tag{1.1}$$

The energy per area of a DW is

$$E_{\omega} = 4\sqrt{AK} \tag{1.2}$$

where A is the exchange stiffness constant and K is the magnetocrystalline anisotropy constant. For Co based materials, A is around 10^{-11}J/m and K is in the order of 10^5~ 10^6 J/m^3. This results in the width of DW to be about tens of nanometers for Co based materials and the energy of DW is about 10^{-3} ~ 10^{-2} J/m^2. A typical value of DW width is in the range of 10 nm to 100 nm for most ferromagnetic materials.

The width of DW also varies with different types of DW. The DWs can be classified into two basic types depending on the way that the spins rotate from one domain to the neighbored ones. In a Bloch wall, the spins rotate in the plane of the domain wall and in a Néel wall, the spins rotate in a plane perpendicular to the wall as shown in Fig. 1-1 [15]. In addition, the types of DW are also dependent on the sample thickness for thin-film samples. Furthermore, for patterned thin-film samples (such as nanowires), the type of DW is also dependent on the geometry of samples.

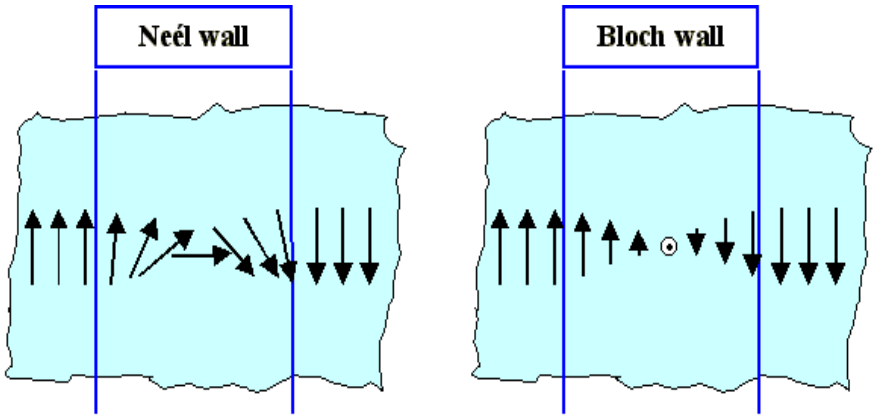

Fig. 1-1 Magnetization vector plots of N éel and Bloch wall.

In thin-film nanowires with in-plane magnetic anisotropy (IMA), there are two basic types of DWs, i. e. head-to-head and tail-to-tail DWs as shown in Fig 1-2.

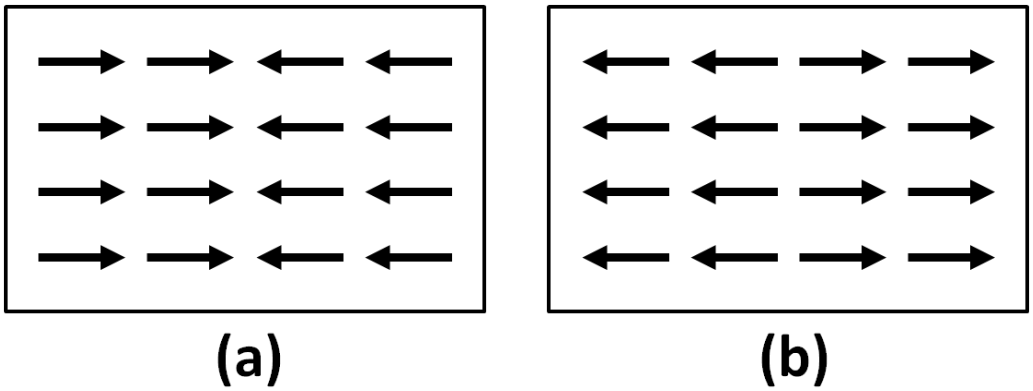

Fig. 1-2 Magnetization vector plots of a) a head-to-head and b) a tail-to-tail domain wall in a thin magnetic wire.

Additionally, DWs are also classified by the structures, which are vortex and transverse DWs, as shown in Fig. 1-3 [15]. It is important to note that for current-driven DW motion, different domain-wall types require different critical current density and they may move at different speed.

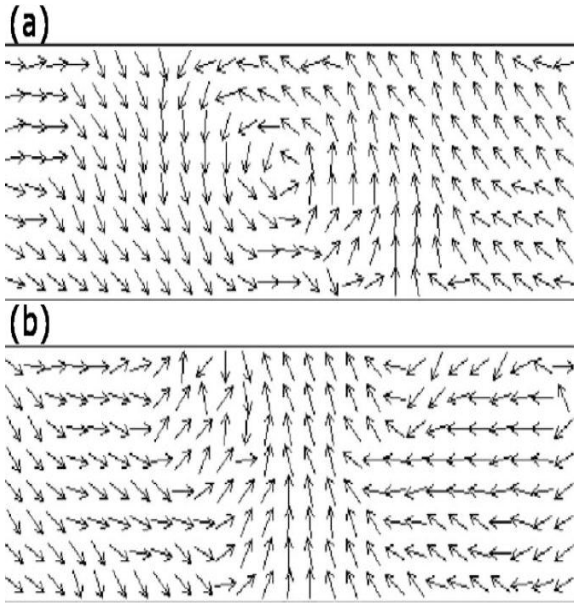

Fig. 1-3 Magnetization vector plots of (a) a vortex domain wall and (b) a transverse domain wall in a thin magnetic wire.

1.1.3 Magnetic domain wall based racetrack memory

Racetrack memory (RM) combines the best of two devices currently used extensively to store data; random access memory (RAM), which is fast and reliable, and the HDD, which is cheap. The storage method is similar to a HDD. The basic structure of racetrack memory (RM) is shown in Fig. 1-4 [16]. The racetrack memory is constructed into a 3-dimensional structure, which is different from the majority of existing storage technologies. The 3D-structured RM exhibits higher density capacity than that of nearly all other solid-state memories. In the racetrack memory, the digital data are stored in the tiny magnetic domains which are separated by the domain walls in 3-D array structured nanowires. The red and blue colors represent the direction of the magnetization along the nanowire. The boundary between the magnetic domains is the DW. In principle, spin-polarized current is applied to drive magnetic DWs

propagation up and down along the nanowire without displacing any atoms at all. The data is read out from a read device, possibly a MTJ, which is located near the substrate. The writing of data is performed by nucleating these tiny domains in the wire and the information is stored in the wire by driving these domains into the wire using a spin-polarized current. When a DW is passed through this lateral magnetic nanowire, DW is associated with a large localized magnetic stray field, which can be used to set the magnetization direction of the targeted bit in the racetrack.

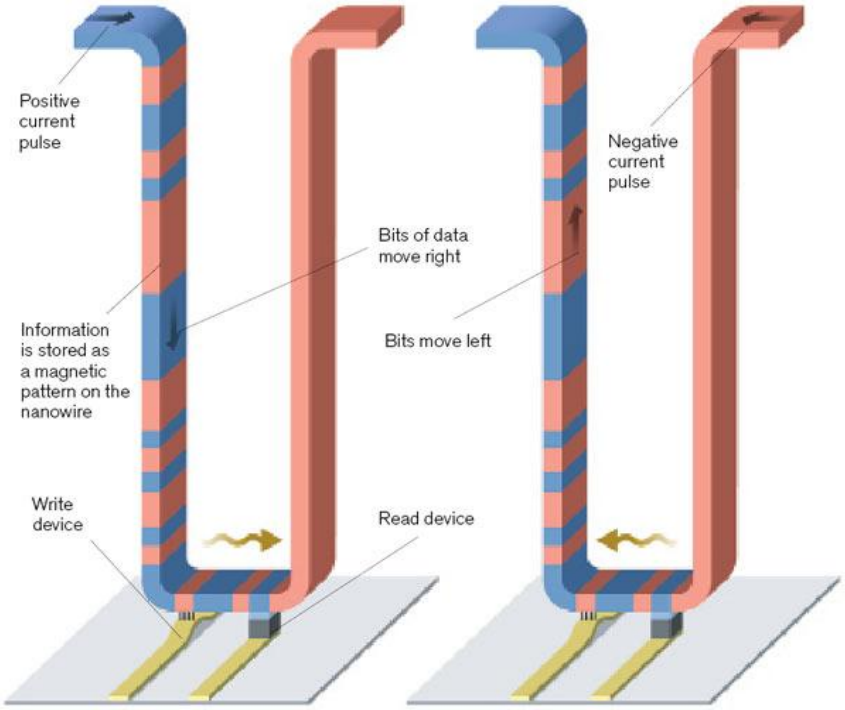

Fig. 1-4 Schematic illustration of the magnetic racetrack memory [16].

The direct influence of a spin-polarized current on the magnetization was theoretically predicted in the 1980s by Luc Berger [17] and was called spin transfer torque (STT). In 1996, Slonczewski [18] predicted that when a spin-polarized current passes through DWs, the spin angular momentum is transferred from the conduction electrons to the local magnetization in the DW. This will lead to a reaction force,

spin-transfer torque, STT, on the local magnetization and consequently reverse the direction of magnetization, which can be used to drive the DW motion. In order to either read or write one bit, the targeted bit has to be moved to the reading or writing device, respectively. To achieve this goal, a single current pulse need to drive all the data bits (DWs) to move together, resulting in the targeted bit reaches the reading or writing element without disturbing the other stored bits. A single current pulse excitation to drive all the DWs' motion in a synchronized mode is required.

The key point to the operation of RM is the STT effect induced all DWs motion in the same direction (along the direction of the electron flow). It is still a novel and challenging research field for commercial application and the new physics involved into the current-induced DW motion (CIDWM) is still needed to be further studied. It is noteworthy that the proof-of-principle of the RM in the application of a DW shift register has already been reported in devices using both in-plane and perpendicularly magnetized materials [16]. There are still some important parameters, such as threshold current density, domain wall width and domain wall velocity, which will largely influence the performance of the CIDWM in the magnetic films, need to be further understood. In addition, the issue in the fabrication process and the huge current densities on the motion of magnetic domain walls are also needed to be addressed.

1.1.4 Perpendicular magnetic anisotropy (PMA)

Ferromagnetic materials exhibit intrinsic “easy” and “hard” directions of the

magnetization. This magnetic anisotropy is one of the most important properties of magnetic materials. An individual layer in a multilayer stack become thinner, the role of interfaces and surfaces may dominate that of the bulk. This is the case in many magnetic multilayers, where a perpendicular interface contribution to the magnetic anisotropy is capable of rotating the easy magnetization direction from in the film plane to perpendicular to the film plane. The perpendicular magnetic anisotropy (PMA) is a result of a magnetic anisotropy at the interface which considerably differs from the magnetic anisotropy in the bulk. This type of magnetic anisotropy is called interface or surface anisotropy [19]. For multilayers, PMA was first observed in 1985 by Carcia et al in the Co/Pd system [20] and later on in several other Co-based multilayers: Co/Pt [21], Co/Au [22], and Co/Ru [23].

Multilayer films with PMA have attracted much interest due to their promising applications in spintronics and magnetic memory fields [19]. The PMA films with high M_s have been used for bit-patterned media recording technology [24]. In spintronics, the PMA films have been exploited in low-energy devices, such as spin-transfer-torque MRAM [25], nanowire memory [13] and spin logic devices [26]. The PMA films are applied to create spin-torque devices operating with low energy consumption.

Among the STT applications in MRAM, the first STT switching of the perpendicular magnetization is demonstrated with a giant magnetoresistance (GMR) element [27-29]. The first verification of STT switching of the p-MTJ was published in 2007 [30].

In addition, the PMA films with unique magnetic properties have been extensively concentrated for spin-torque domain walls (DWs) nanowire devices (non-volatile memory, spin logic devices, etc). Materials with perpendicular magnetic anisotropy (PMA) exhibit narrower DWs (Δ ~10 nm) as compared with IMA (Δ ~100 nm), which are favorable for high density magnetic storage of racetrack memory [31]. In addition, micro-magnetic simulation results [32, 33] predict that the energy barrier required to drive DWs in precessional motion is smaller by an order of magnitude in PMA films than in IMA ones. However, one of the most important issues of such devices with PMA is to reduce magnetization-switching current density, of which the threshold current density (J_{th}) is essentially governed by the intrinsic parameters of the films [34]:

$$J_{th} \propto \frac{\alpha M_s \lambda}{|\beta - \alpha| P} \tag{1.3}$$

where α, β, M_s, λ and P are the Gilbert damping factor, non-adiabatic spin transfer parameter, saturation magnetization, domain wall width and spin polarization of the film, respectively. A high effective magnetic anisotropy (K_{eff}) is favorable for the small λ and high β. Therefore, a high PMA film with low M_s, low damping constant α, narrow DW and high spin polarization P would be desirable for a spin-torque DW device working with low current density.

1.2 Motivation

The magnetic DW motion driven by the spin polarized current in nanowires has been a subject of great interest due to its potential application in the field of emerging

data storage devices, such as racetrack memory (*RM*). In this context, the high capacity density, reasonably low current density to control the DW motion, high DW velocity for high speed devices and strong structure stability for long-term usage are the primary concerns for practical application.

For high capacity density, the narrow and elementary DWs are the main motivation to fundamentally study in these materials. Magnetic films with perpendicular magnetic anisotropy (PMA) have been recently proposed to replace the in-plane film for the application of DW motion due to its superior properties. PMA films exhibit narrower DWs as compared with IMA ones, which are favorable for high density magnetic storage. For typical PMA multilayer films, such as Co/Ni and Co/Pt, the effective magnetic anisotropy (K_{eff}) as well as the heat dissipation performance can be improved by appropriately tuning the thickness of sublayers (i.e. Co, Ni or Pt) and the repeated number of bilayers (i.e. Co/Ni [35] or Co/Pt [21]). The drawback, however, is a high intrinsic DW pinning naturally occurring in these materials. This DW pinning is due to the sensitivity of the narrow DWs to any structural inhomogeneities. The pinning strength increase the potential barrier to be overcome for motion of DWs. The DWs easily get pinned by small fluctuation of the local energy of the DW associated with these inhomogeneities. The strong pinning strength not only leads to an enhanced stochastic effect, but also requires a rather high driving current density in the order of 10^{12} A/m^2 for current-induced DW motion [36]. The pinning strength strongly depends on the magnetic material properties and the geometry of the nanowire. So far, this has lead to only a few reports of purely

current-driven DW motion and most of these reports show results where the motion by current is necessarily assisted by a magnetic field. As a result, it is important to reduce pinning strength as well as driving current density in order to realize DW based device.

A prototype of RM introduced by Parkin *et al.* (as discussed in Sec. 1.1.5) using NiFe nanowire has been proposed [13, 37]. This version provides ultrahigh storage density over commercial HDD and fast access speed comparable to the fastest DRAM. However, NiFe-based devices require high current density ~ 3×10^{12} A/m^2 to drive the motion of DWs. For the effect to be observed, the current density needs to be of the order of 10^{12} A/m^2. This amounts to around 10^8 A/cm^2. Due to the heating effect of the associated enormous total current, the devices would melt long before such current densities are reached [38, 39]. This is an enormous value and thus one of the major motivation for the research field is to decrease the threshold current density. Therefore, one needs to drastically decrease the driving current density required for DW motion and find efficient ways to minimize the heating effect. This is exactly what happens when devices reach dimensions in the nanometer range. Many efforts need to be made to reduce the current density.

For the DW velocity (v), it is expected that v is highly dependent on the STT efficiency for the DW motion [31]. It is important to understand the physical principle for enhancing the STT efficiency in order to increase the DW velocity. Therefore, this development will be greatly facilitated by a complete understanding of the physics behind the current-induced DW motion.

There are several important aspects that need to be addressed to make a viable racetrack memory. In this thesis, CoFe/Pd-based multilayers was chosen as a research subject. In comparison with other Co based multilayers, such as Co/Pt (M_s ~ 600-700 emu/cc, λ ~ 10-20 nm, α ~ 0.1-0.3) [40, 41], Co/Ni (M_s ~ 800 emu/cc, λ ~ 10-30 nm, α ~ 0.04)[42], the CoFe/Pd multilayers in our study possess a smaller M_s (220-700 emu/cc), λ (6-15 nm) and α (0.015-0.1) [43-46], which are also significant to reduce J_{th} of DW motion and increase the STT efficiency in the nanowire devices. Moreover, the high post-annealing stability of superlattice-like CoFe/Pd structure films has been observed, which can enhance the stability of the device for long-time usage [45]. Furthermore, the influences of magnitude of the current density and non-adiabatic torque on the DW velocity in CoFe/Pd multilayers based nanowires have also been systematically studied.

On the other hand, as the lateral dimension of DW memory bites being scaled down for high-density capacity, the dipolar fringing field from the neighbouring magnetic domains increases dramatically and results in strong interaction between adjacent DWs. This will degrade the performance of the device and limit the data density for RM. An efficient solution is to use a synthetic antiferromagnetic (SAF) structure, which consists of two ferromagnetic (FM) layers separated by a nonmagnetic spacer layer. Therefore, the magnetic property and DW motion in CoFe/Pd multilayers based SAF structure nanowires are also needed to investigated.

1.3 Objectives

The objectives of the research work described in this thesis are listed as follows.

(i) To investigate magnetic properties of CoFe/Pd-based multilayers and its related synthetically antiferromagnetic (SAF) structure.

(ii) To investigate the displacement of DW driven by electric current and magnetic field in perpendicularly magnetized nanowires patterned on CoFe/Pd-based multilayer films by anomalous Hall-effect measurement.

(iii) To understand the important parameters (i.e. M_s, α, β) on the threshold current density and the DW velocity, we systematically study the influences of magnitude of the current density and non-adiabatic torque on the DW velocity in the CoFe/Pd multilayers based nanowires.

1.4 Outline of this thesis

This thesis is organized as follows:

Chapter 1 provides a brief introduction on the basic knowledge of magnetic domains (DW) and the origin of DW formation. The DW based devices for the next generation memories and logic systems is also introduced.

Chapter 2 gives a literature review on the explanation of phenomenon that magnetic field and spin-polarized current driven DW motion. The performance of current induced DW motion in typical in-plane and PMA materials are also reviewed.

Chapter 3 describes the experimental techniques to characterize magnetic thin

films and fabricate the nanowires. The transport measurement for DW motion using the Hall effect is also presented.

Chapter 4 presents the magnetic properties of $(CoFe/Pd)_n$ multilayers with thickness of CoFe and Pd sublayers are larger than monolayer. The study of DW motion induced by current and H in the perpendicularly magnetized nanowires patterned on the $(CoFe/Pd)_n$ multilayers with thickness of CoFe and Pd sublayers are larger than monolayer are also presented.

Chapter 5 presents the characterization of monatomic $(CoFe/Pd)_n$ superlattice-like film and the study of DW motion induced by current and H in the perpendicularly magnetized nanowires patterned on monatomic $(CoFe/Pd)_n$ superlattice-like films.

Chapter 6 presents the study of magnetization reversal and magnetic interlayer coupling in $(CoFe/Pd)_n$ superlattice based synthetic antiferromagnetic (SAF) structure.

Chapter 7 presents the low current density induced DW motion in perpendicularly magnetized nanowires patterned on the $(CoFe/Pd)_n$ superlattice-based synthetically antiferromagnetic (SAF) structure with high DW velocity.

Chapter 8 summarizes the findings in this thesis and provides recommendations for future work.

Chapter 2 Review of domain wall motion

This chapter gives a short overview of the theory of magnetization dynamics induced by magnetic field and the spin polarized current. The influence of the magnetic and electronic transport properties of the materials on the spin transfer effect in DWs is also discussed. The results of current induced DW motion in the various IMA and PMA materials are also presented.

2.1 Theory of domain wall motion

2.1.1 Field driven domain wall motion

In ferromagnetic materials, the magnetization direction of specimen can be controlled by both of the static and dynamic magnetic fields (H). Under applied H, the magnetic domain, which is magnetized in the same direction with H, grows whereas the magnetized domain with reversed magnetization direction shrinks. Therefore, the DW separating these two domains then propagates under H**.** Although it is understood that the DW motion is mainly determined by the direction of H, the actual DW dynamics driven by H is a more complicated process. This is because H can generate a torque perpendicular to both H and magnetic moment. This torque would deform the internal DW magnetization, which sequentially induces other torques to affect DW dynamics.

In principle, the magnetic moment dynamics under H can be expressed using the Landau-Lifschitz-Gilbert (LLG) equation [47]:

$$\frac{dm}{dt} = -\gamma(m \times H_{eff}) + \frac{\alpha}{M_s}(M \times \frac{dm}{dt}) \quad (2.1)$$

where m is the magnetic moment, M is the magnetization vector, γ is the gyromagnetic ratio, M_s is the saturation magnetization of the material, α is the Gilbert damping constant, and H_{eff} is the effective field. The H_{eff} includes the effect of the anisotropic, dipolar and exchange interactions as well as external magnetic field acting on M. The first term in Eq. (2.1) is the magnetic moment precessing around H_{eff}. The second term represents the damping term, which leads to the relaxation of the magnetic moment towards the direction of H_{eff} and finally align in the direction of H_{eff}. The damping strength is quantified by α.

Figure 2-1 schematically presents the DW propagation driven by H in in-plane and perpendicularly magnetized nanowires patterned on the thin films, respectively [48]. Figure 2-1 (a) shows the in-plane magnetized material. If the nanowire width is narrow enough, then a type of transverse DW is formed due to the equilibrium DW configuration. Firstly, H generates a field-induced torque $-\gamma(m \times \mathrm{H})$ to drive the magnetic moments out of the plane of films so that out-of-plane magnetic free poles are created on the surface of films. Sequentially, these free poles generates a demagnetizing field H_d and an additional torque $-\gamma(m \times H_d)$ produced by H_d eventually drives the DW motion.

For the DW motion driven by H, the DW velocity v is linearly proportional to the amplitude of H when H is smaller than the threshold $\mathrm{H_w}$. $v = \mu \mathrm{H}$, where μ is the DW mobility.

The μ can be expressed as

$$\mu = \frac{|\gamma|\lambda}{\alpha} \tag{2.2}$$

where λ is the DW width.

On the other hand, when H > H_w, a constant canting angle cannot be maintained in DW magnetization and the magnetic moment starts to precess around the nanowire axis. In this case, dynamics of DW is determined by the damping torque $\alpha(m \times \frac{dm}{dt})$. The DW velocity can be described as $v \propto \alpha^2 \mu H$.

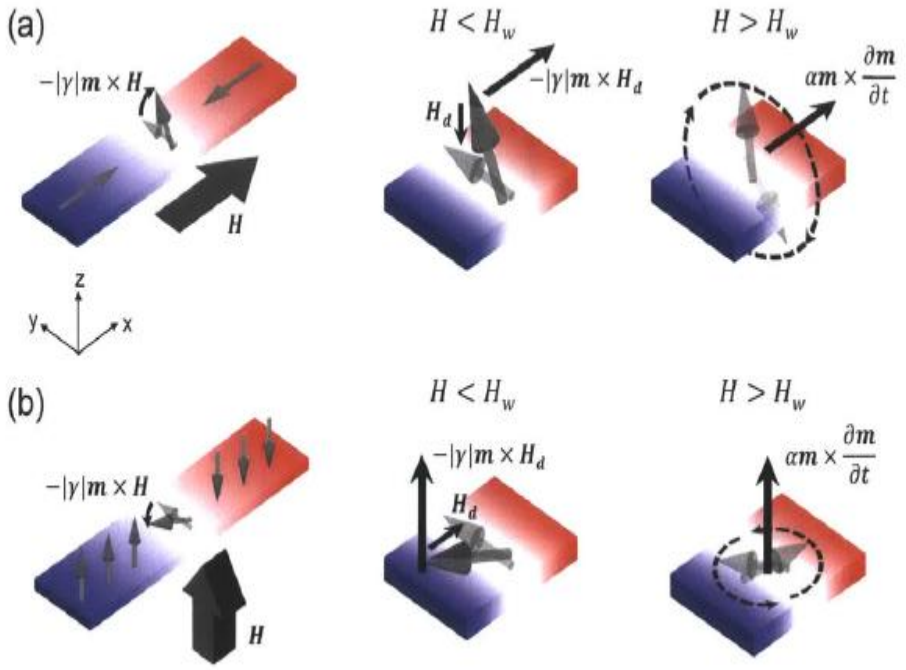

Fig. 2-1 DW propagation driven by H in in-plane (a) and perpendicularly (b) magnetized nanowires patterned on the thin films, respectively. The H_w is Walker field and DW dynamics under the cases of H > H_w and H < H_w are shown [48].

In addition, H_w is defined as Walker field [49], above which the DW velocity drops substantially. The regime where *v* decreases with H is generally named as "Walker breakdown". Figure 2-2 shows the non-monotonic variation of *v* dependent on H in micro-magnetic calculations and experiment for in-plane permalloy nanowires [50, 51].

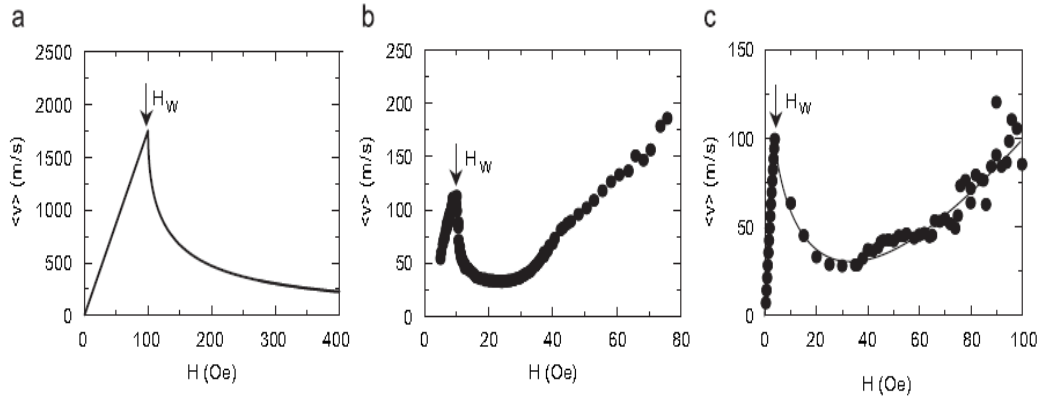

Fig. 2-2 (a) Calculated *v*-H curve using the 1D model for a 500 nm×20 nm permalloy wire. (b) Computed *v*-H curve using LLG numerical simulations for a 200 nm×20 nm permalloy wire. (c) Measured *v*-H curve for a 490 nm×20 nm permalloy nanowire [50].

The DW motion driven by H in the perpendicularly magnetized nanowire can also be understood in the same way as in-plane films. In this case, the magnetic moments in the DW are initially canted to an off-angle in-plane under H perpendicular to the plane of films as shown in Fig. 2-1 (b). This produces a partially Néel-like configuration and therefore a demagnetizing field. When $H < H_w$, the torque $-\gamma(m \times H_d)$ generated from the demagnetizing field drives the DW motion. When $H > H_w$, the damping torque $\alpha(m \times \frac{dm}{dt})$, causes a full precession for DW motion through a periodic transformation between Bloch and Neel configurations within the plane of nanowire.

On the other hand, the energy barrier for driving precessional DW motion is significantly smaller for PMA materials in comparison with in-plane ones. This causes a lower value of H_w and thus a higher DW velocity in the low field regime with identical α. This can be explained by the fact that the magnetic moments in DW energetically prefer to cant perpendicularly instead of being in Néel-like configuration.

2.1.2 Current driven domain wall motion

Berger, *et al.* first introduces the spin transfer torque effect, in which the spin from electrons transfer their angular moment to the local magnetization of a DW and control the DW motion at the end of the seventies [52]. When a naturally polarized current passes through the DW, the exchange interaction aligns the spin polarization direction of conducted electrons along the local magnetization direction. As the exchange interaction conserves the total spin, this angular momentum has to be transferred to the local magnetization, which is identical to a torque acting on the magnetization. This results in a DW motion along the direction of the electron flow. As this effect is independent of the thickness of film, it dominates for thin films over the hydrodynamic drag effect that originates from the Lorentz force [17].

The interaction between a spin polarized current and a magnetic DW strongly depends on the relation between the DW width and the length scale describing the transfer of spin angular momentum, i.e. the Fermi wavelength or the Larmor precession length depending on the model and the assumptions used, which is typically a few nm in 3d metals [53-57]. Two limits can be distinguished. When the DW width is very wide, the conduction electron spins adiabatically follow the local magnetization. In the case of a narrow DW, nonadiabatic effects might occur. These two limits are discussed as follows.

The time-resolved evolution of magnetic moments with spin-polarized current can be expressed using the LLG equation incorporating STT terms, which includes both the adiabatic [58] and non-adiabatic torques [59].

$$\frac{dm}{dt} = -\gamma(m \times H_{eff}) + \frac{\alpha}{M_s}(M \times \frac{dm}{dt}) - u\frac{dm}{dx} + \beta u(m \times \frac{dm}{dt}) \qquad (2.3)$$

where the third and fourth terms are adiabatic and non-adiabatic STT, respectively. The term β is non-adiabaticity factor. Figure 2-3 schematically presents the dynamics of magnetization described by Eq. (2.3). When the spin-polarized current flows into ferromagnetic films, spin-polarized current interacts with the local magnetization and leads to a spin direction change of the outgoing electron compared with the incident electron. The difference in spin polarization causes two torques exerted on the local magnetization, which are spin-transfer torque and another field-like torque perpendicular to the plane of incident electron. In Fig. 2-3, the magnetic moment (m) precesses about the direction of H_{eff}. The green arrow illustrates the damping torque to drive m toward the direction of H_{eff}. The red arrow is the spin-transfer torque and its direction is opposite to the damping torque, which drives the magnetization reverse. The light-blue arrow is the effective field torque with an electron spin polarization collinear with the effective field.

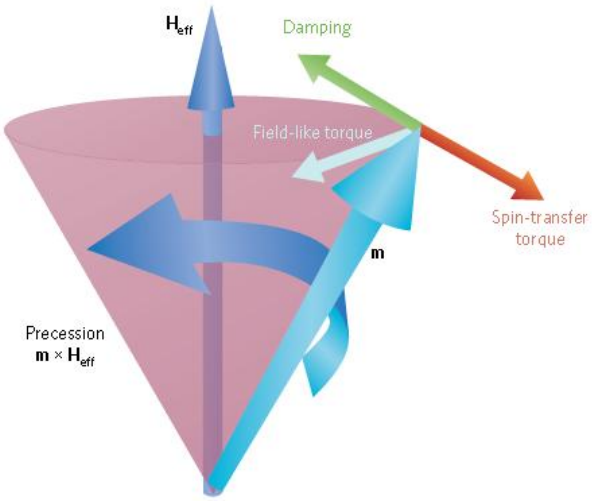

Fig. 2-3 Illustration of the LLG equation.

In addition, the spin drift velocity *u* is also introduced in Eq. 2.3 and *u* is defined as

$$u = \frac{g\mu_B PJ}{2eM_s} \tag{2.4}$$

where μ_B is the Bohr magneton, *e* is the electron charge, *J* is the current density to the direction of electron flow, g is the gyromagnetic ratio and *P* is the spin polarization of current. In the STT effect, the DW moves in the direction of the electron flow, and this mechanism involving the spin angular momentum conservation is known as adiabatic STT [60]. Figure 2-4 schematically presents the DW propagation driven by adiabatic spin-transfer torque in in-plane and perpendicularly magnetized nanowires patterned on the thin films, respectively. As the directions of the adiabatic STT torque and damping torque damping term are opposite**,** adiabatic STT torque together with damping torque, cant the DW magnetization and produce a demagnetizing field H_d**.** When the adiabatic torque (i.e. spin-polarized current density) is not large enough, the canted DW magnetization will stop due to the balance between demagnetizing torque $-\gamma(m \times H_d)$ and adiabatic STT torque at an equilibrium DW canting angle. The DW can be driven to propagate only when the adiabatic STT torque is larger than the demagnetizing torque. The DW moves via rotating its magnetization about the x-axis in a corkscrew-like way with large adiabatic STT torque**.**

However, this adiabatic STT torque only drives the motion of DWs in a precessional mode. Below the threshold current, which is sufficiently to generate the precess motion, the conduction electrons will deform DWs structure instead of

inducing a lateral displacement. This threshold energy is the "intrinsic barrier" for adiabatic STT driven DW motion [61].

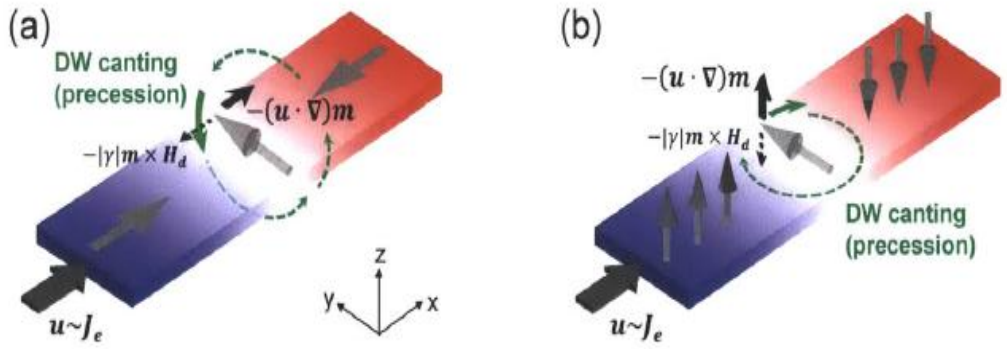

Fig. 2-4 DW propagation driven by adiabatic spin-transfer torque in in-plane (a) and perpendicularly (b) magnetized nanowires patterned on the thin films, respectively [48].

We note that the measured threshold current density J_{th} ($\sim 10^{12}$ A/m^2) for DW motion in permalloy nanowire is much smaller than the calculated J_{th} ($\sim 10^{13}$ A/m^2). One of the reasons is that J_{th} is assumed to be only driven by adiabatic torque. Furthermore, J_{th} is claimed to change with the pinning strength of DW due to defects [13].

Another kind of STT torque — non-adiabatic torque [62] is proposed to explain the result that the measured J_{th} is much smaller than the calculated J_{th}. Figure 2-5 schematically shows the DW propagation driven by non-adiabatic spin-transfer torque in in-plane and perpendicularly magnetized nanowires patterned on the thin films, respectively. It is found that the symmetry of non-adiabatic STT acting on a DW is identical to that of H driving a DW motion [59]. Therefore, the non-adiabatic torque drives DW propagation at a current density smaller than the J_{th} derived by adiabatic torque. It is expected J_{th} is only determined by the intrinsic pinning for adiabatic

torque. On the other hand, the non-adiabatic term is dependent on the extrinsic pinning. Therefore smaller J_{th} is required for DW motion in perfectly defect-free materials. Moreover, DW velocity can be dramatically increased due to the nonadiabatic torque via rigid translation, rather than lossy precession that is accompanied with the adiabatic torque. For these reasons, nonadiabatic STT has been intensively investigated both theoretically and experimentally.

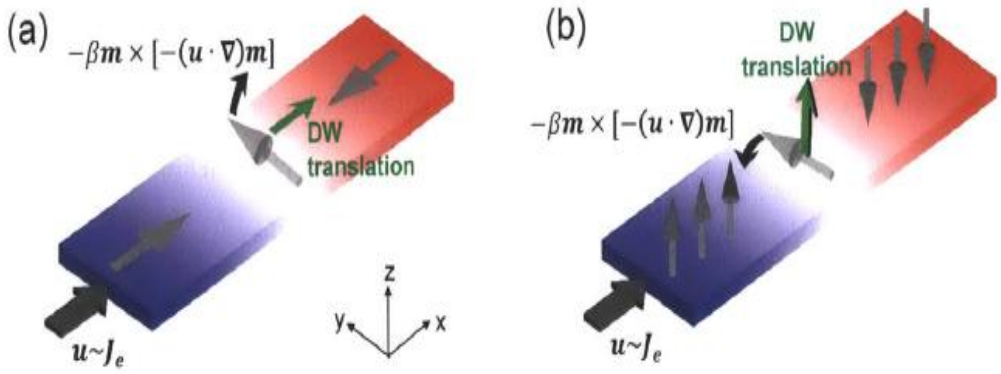

Fig. 2-5 DW propagation driven by non-adiabatic spin-transfer torque in in-plane (a) and perpendicularly (b) magnetized nanowires patterned on the thin films, respectively [48].

Similar to field-driven DW motion affected by the Walker-field threshold (Fig. 2-5), the nonadiabatic torque drives a DW through rigid translation at a small current, whereas it drives a DW through precession at a large current. When the nanowire is defect-free, Walker breakdown will appear in the current-driven DW velocity curves with sufficiently large β as shown in Fig. 2-6. Based on the simulation model [59]**,** the DW velocity dependent on J below the precessional threshold J_{th} is expressed as

$$v = \frac{\beta}{\alpha} u \tag{2.5}$$

where

$$u = \frac{\mu_B P}{e M_s} J \tag{2.6}$$

For the precessional regime of DW motion ($J > J_{th}$), the DW velocity is given [31] by

$$v = \frac{1+\alpha\beta}{1+\alpha^2}u \tag{2.7}$$

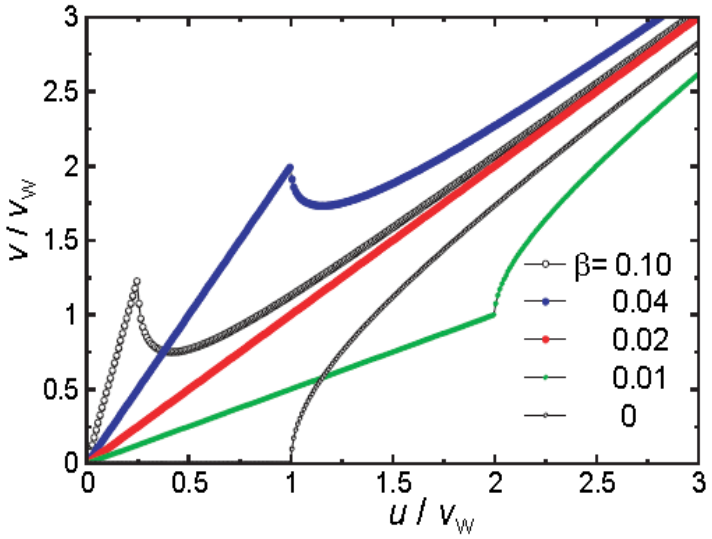

Fig. 2-6 Simulated DW velocity (v) as a function of spin drift velocity (u) with various values of nonadiabatic spin-transfer torque. α=0.02 [59].

From the microscopic point of view, the contribution of adiabatic and nonadiabatic terms depends on the DW characteristic width of a given material. When DW width is wide, the electron spin can adiabatically follow the local spin direction as the electrons transverse the DW. As DW width is narrow, the spatial magnetization gradient across the DW will become very large. This causes the formation of a finite mis-tracking angle between the electron spin and local spins and result in spin-flip scattering of the electrons and a nonadiabatic torque acted on the DW [63].

However, there is also a controversy regarding the magnitude of non-adiabatic torque β. This incomplete understanding of non-adiabatic torque makes it difficult to engineer and investigate the evolution of magnetic textures in ferromagnetic materials using current driven STTs. Therefore much more detailed research need to be done to derive the exact magnitude of β for future study.

2.1.3 Thermally activated domain wall motion

Thermal activation also affects the DW motion. Martinez *et al.* [64] found that even the driving force (either field or current) is smaller than the determined threshold, thermal activation will cause a non-zero DW velocity through micro-magnetic simulations. On the other hand, thermal activation has a neglectable effect on the DW velocity when the driving force is stronger than the pinning force. In the thermally activated regime, it is found that the DW velocity exponentially depend on the driving force. Duine *et al.* [65, 66] and Tatara *et al.* [67] also investigated the function of thermal activation. In the pure adiabatic case, the DW motion can be observed with a current density lower than threshold current density at zero field since thermally activated jump of the DW angle ψ over the demagnetizing energy barrier. However, this effect only occurs in systems with a small DW demagnetizing energy such as in the magnetic semi-conductor (Ga,Mn)As and has little impact in metallic systems.

Schieback *et al.* [68] dealt with the situation differently. They introduced the thermal effect using a Landau-Lifschitz Bloch (LLB) equation [69] where the magnetization modulus is not assumed to be constant and is temperature dependent. Hence, besides the usual precession and relaxation, the LLB equation contains another term which controls the longitudinal relaxation. Under this assumption, the DW internal structure is strongly affected by the local disorder at small H or current. In this regime, the DW propagation process is similar to an interface in a disordered medium and results from the competition between the elastic energy of the DW that tends to keep the domain line straight and the disorder which tends to roughen it. The

dynamics of a DW driven by an external magnetic field H in this regime was shown to follow a law of the form [70, 71]:

$$v = v(\mathrm{H_{dep}})exp\left[-\frac{\mathrm{U_c}}{\mathrm{k_B T}}(\frac{\mathrm{H_{dep}}}{\mathrm{H}})^{\eta}\right] \quad (2.8)$$

where H_{dep} is the depinning field from the pinning force. The U_c is a constant describing the pinning energy and η is a constant characteristic of the disorder and of the dimensionality of the system, which equals to 1/4 in ferromagnetic metals.

To further understand the current driven DW motion in this regime, the Duine *et al.* [65, 72] expressed the DW velocity scaling by considering extrinsic pinning as

$$lnv \propto -\frac{\epsilon_{el}}{\mathrm{k_B T}}(\frac{\mathrm{J_{th}}}{J})^{\mu_c} \quad (2.9)$$

where ϵ_{el} is the elastic energy and μ_c is the critical exponent. The main results of their calculations was that the exponent characterizing the creep regime strongly depends on the presence of a dissipative spin transfer torque. In ferromagnetic metals, μ_c is found equal to 1/4 for $\beta \neq 0$ as is in the case of field driven DW motion.

2.1.4 Spin Orbit Torques and Dzyaloshinskii Moriya Interaction

Recently, it has been observed experimentally that DWs in certain ferromagnetic nanowires can move at a significantly larger speeds on the order of ~400m/s and that their direction is opposite the direction of electron flow [73]. These phenomena have been seen in ultrathin ferromagnets sandwiched between a heavy metal and an oxide layer, e.g. Pt/Co/AlO_x [74] as well as in structures such as Pt/CoFe/MgO [75]. This observation cannot be explained using conventional STT, and therefore new torques have been introduced: the field-like torque and the Slonzewski-like torque. These two

additional torques are known to originate fundamentally from spin orbit interactions at the interfaces between ferromagnets and heavy metals or ferromagnets and oxides. The LLG equation can also be modified to include these additional torques on a magnetic moment [76]

$$\frac{dm}{dt} = -\gamma(m \times H_{eff}) + \frac{\alpha}{M_s}(M \times \frac{dm}{dt}) - \tau_F \sigma \times m + \tau_T M \times (\sigma \times m) \qquad (2.10)$$

where H_{eff} includes effective fields from spin-orbit interactions and σ is the unit vector in-plane and orthogonal to the applied current, and τ_F and τ_T are the field-like torque and the Slonzewski-like torque coefficients, respectively. These torques are usually represented as effective fields where that of the field-like torque has a direction that depends on the direction of the applied current and that of the Slonczewski-like torque (or damping-like torque) points (anti-) parallel to the damping torque for magnetization vector. These two torques can cause the same qualitative and quantitative changes in DW dynamics, causing controversy regarding the dominant physics behind experimentally observed DW dynamics.

The first observation of this phenomenon was made by Miron *et al.* [73, 74, 77] showing a strong current-induced Rashba field transverse to the nanowire in an asymmetric Pt/Co/AlOx structure. The first estimation of the Rashba effective field was approximately 1 T, enough to overcome the materials' anisotropy field, and the calculated efficiency was extremely large, ~1 T/10^8 A/cm^2 [77]. Because the Rashba effective field is effectively an in-plane transverse field, it alone cannot propel DWs' motion, therefore, Miron *et al*. [74] [77] have attributed the extraordinary motion to a combination of the Rashba effect and a strong non-adiabatic STT. They have stated

that the DW is in the Bloch configuration at rest and that the strong effective fields from the Rashba effect can lock the Bloch configuration such that only rigid translation can occur at high DW velocities.

However, the mechanism of a strong field-like torque still involves relatively large non-adiabatic STT, which is not well understood. In parallel to this approach, Liu *et al.*[75, 78] have performed a series of experiments using similar heavy metal/ultrathin ferromagnet/oxide structures and proposed an alternative spin orbit mechanism based on the spin Hall effect. In short, the spin Hall effect is the effect wherein a pure spin current is generated orthogonal to a charge current in a heavy metal with strong spin orbit coupling (e.g. Pt, W, or Ta). The bulk metals preferentially scatter spins of opposite direction, leading to spin accumulation at the edges [79]. When an ultrathin ferromagnetic layer is placed in contact with a heavy metal, scattered spins can be injected into a ferromagnet, exerting an additional torque. This effective torque from the spin Hall effect is called the Slonzewski-like torque which acts as an effective field, H_{SL}, causing either a damping or anti-damping effect. The spin Hall effect was first predicted by Dyakonov and Perel *et al.*[80] and Hirsch *et al.*[81], and spin accumulation was first experimentally observed in semiconductors by Kato *et al*[82]. The ratio of the charge current to the spin current, which measures the efficiency of vertical spin injection, is called the spin Hall angle, θ_{SH}. The sign and magnitude of spin Hall angle depend on the structure and composition of the heavy metal layer.

Liu *et al.*[75] have also demonstrated current-induced switching in Pt/Co/AlO_x,

which is the same structure as used by Miron *et al.*[74] for their Rashba model, and concluded that the strong spin Hall effect is responsible for the switching. Later experiments have showed that the DWs in ferromagnets grown on Ta and Pt move in opposite directions for the same direction of applied current, which has since been explained by taking into account the opposite signs of the spin Hall angle in Ta and Pt [75, 78]. However, even in this spin Hall model, the Slonzewski-like effective field cannot drive a Bloch DW. When we use the magnetization vector pointing Bloch configuration in Eq. 2.10, the effective torque from spin Hall effect (or Rashba effect), τ_T (or τ_F), is zero. Therefore, the Néel configuration is required for DW motion driven solely by the spin Hall effect. However , the orgin of Néel DW configurations is needed to further understand. Recently, a interfacial spin orbit interaction, the Dzyaloshinskii-Moriya Interaction (DMI) [83, 84] has been proposed, which can stabilize Néel-type DWs in ultrathin sputtered film stacks with asymmetric interfaces, such as Pt/CoFe/MgO [84] or Pt/CoFe/AlO_x [83] at room temperature.

The DMI is dominant in materials with a broken inversion symmetry in their lattice or at interfaces in engineered material structures, which will induc the chiral magnetic configurations [85]. DMI is known to originate from large spin orbit coupling. Unlike the exchange interaction that aligns neighboring spins in an (anti-)parallel configuration, DMI prefers a perpendicular spin arrangement in order to minimize its cross product. The DMI can arise in both bulk material as well as at interfaces between a ferromagnet and another material with large spin orbit coupling, e.g. heavy metals.

2.2 Characterization of domain wall motion

In this section, we introduce some of the experimental techniques that are commonly used for detection and characterization of DW motion in magnetic nanowires. The choice of the technique to be used depends on the DWs properties that one wants to study. For instance, magnetic microscope techniques are used to detect the presence of the DWs in a certain section of the wire, while anomalous Hall effect or magneto-optical Kerr effect (MOKE) measurements can be used to detect the DW position and the DW dynamics.

2.2.1 Anomalous Hall effect measurement

In 1879, Edwin H. Hall [86] found that when the current passes through a conductor, which is placed in a magnetic field, the Lorentz force "pushes" its electrons against one side of the conductor. The phenomenon is known as Hall effect. Later, Hall *et al.* [87] also reported that the "pushing electricity" effect is ten times larger in ferromagnetic iron than in nonmagnetic conductors. The stronger effect that Hall discovered in ferromagnetic conductors came to be known as the anomalous Hall effect (AHE) [88].

The AHE is usually used to characterize DW motion in magnetic systems with PMA [34, 36, 89]. Such measurements require the sample to be patterned into a Hall cross geometry. The AHE occurs in solids with broken time-reversal symmetry, typically in a ferromagnetic phase, as a consequence of spin-orbit coupling [90]. The AHE allows us to detect magnetization variation with a sensibility of the same order

as micro-Squid techniques [91]. The Hall resistivity ρ_H in homogeneous thin films of ferromagnetic metals can be written in a perpendicularly magnetic field H [88],

$$\rho_H = R_{OHE}\mu_0 \mathrm{H} + R_{AHE}\mu_0 M_s \tag{2.11}$$

where M_s is the perpendicular saturation magnetization. R_{AHE} and R_{OHE} are the anomalous and ordinary Hall coefficients, respectively. The first term is the ordinary Hall effect and the second term is the AHE. Then measuring in a Hall cross the time variation of ρ_H during magnetization reversal from $-M_s$ to $+M_s$ allow us to study the dynamics of reversal. Besides, the time variation of the Hall signal when the DW is passing from a wire of constant lateral width to a Hall cross reveals the influence of lateral size on DW propagation [92]. In this thesis we mainly use the AHE to locally detect the DW motion in magnetic nanowires. In the AHE measurement setup, a current is sent through the sample, and the voltage perpendicular to the current is measured. Detection of DW displacements smaller than 1 nm can be achieved due to the large AHE signals [93].

2.2.2 Magnetic microscopy techniques

The magnetic imaging techniques are commonly to detect the spin configuration in DW structure, including magnetic force microscopy (MFM), Lorentz microscopy, scanning electron microscopy with polarization analysis (SEMPA), Kerr microscopy (magneto-optical Kerr effect - MOKE), photoemission electron microscopy (PEEM) and scanning transmission X-ray microscopy (STXM). For magnetic imaging, the last two techniques are used together with X-ray magnetic circular dichroism (XMCD),

which yield the dependence of the absorption coefficient of a magnetic material on the helicity of circularly polarized X-rays and the magnetization direction. The MFM has been widely used to characterize DW structure and DW dynamics in magnetic nanowires with IMA [94, 95] and PMA [96-98]. The major advantage of MFM technique is its simple and fast implementation together with a high resolution of down to 10 nm depending on the details of the system. Electron microscopy techniques are particularly well suitable for mapping the spin structure of a magnetic nanostructures since they provide high resolution with the advantage of being largely non-invasive. Transmission electron microscope can be used to perform Lorentz microscopy [99] or (off-axis) electron Holography [100, 101]. These two techniques take advantage of the fact that the high energy electrons which are accelerated to energies of a few hundreds of keV have both particle and wave like properties. Both techniques have been recently used to study the structure and pinning of DWs at constriction [102, 103] and the structure variation of a DW in a NiFe nanowires with different anti-notches [104].

2.2.3 Optical measurement techniques

Magneto-optical Kerr effect (MOKE) is a very well established technique to study magnetism in thin solid film [105] and it has been successfully adapted to investigate DW motion in magnetic sub-micron sized nanowires [106]. Many experiments on DW propagation have been reported using MOKE microscopy [96, 107]. While the laser spot size on the sample is diffraction limited, MOKE

microscopy has allowed for imaging of nanostructures as small as 30 nm [108]. Moreover, time-resolved experiments using a time-of-flight measurement technique have been carried out to characterize DW propagation in NiFe nanowires [109]. This technique has allowed the Walker breakdown field to be observed in NiFe as well as the periodical transformation of a DW [51].

2.3 Current induced domain wall motion

2.3.1 Current induced domain wall motion in in-plane magnetized nanowires

Current induced DW motion in the thin films with in-plane magnetic anisotropy (IMA) have been intensively investigated theoretically and experimentally in the recent decade. Theoretical models [59, 110] have been developed and a large number of experiments [111-114] have been carried out to understand the mechanism of spin transfer torque exerted on the DW motion in such systems. The IMA material most frequently employed is permalloy ($Ni_{80}Fe_{20}$). It has virtually zero magnetostriction and magnetocrystalline anisotropy, making it very soft with low propagation fields for DWs [31]. Figure 2-7 shows the summary of the threshold current density (J_{th}) in permalloy nanowires with thickness less than 40 nm under zero external magnetic field (H) [115]. It is found that J_{th} are between 5×10^{11} and 3×10^{12} A/m^2 [115]. Klaui *et al.* have reported $J_{th} \sim 5\times10^{11}$ A/m^2 for a 5 nm thick nanowire and 1.3×10^{12} A/m^2 for a 35 nm thick permalloy nanowire [116]. Hayashi *et al.* found a maximum DW velocity $v_{max} \sim 130$ m/s in a permalloy wire using the AMR effect [117].

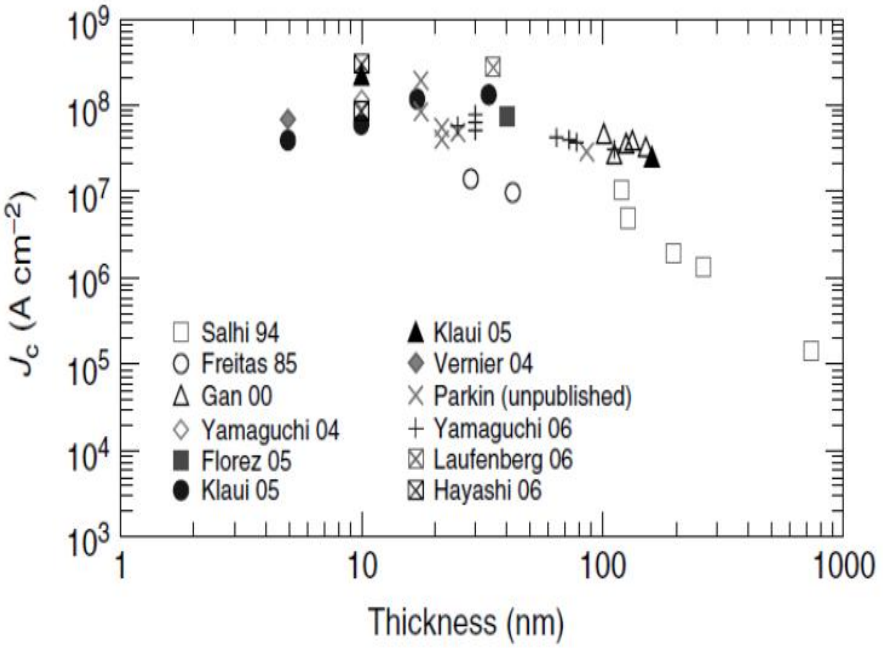

Fig. 2-7 Threshold current density for DW motion in permalloy nanowires dependent on the nanowire thickness [118].

Other in-plane magnetized materials include CoFe [119] and thick FePt films (~ 10 nm) [120]. Tsoi *et al.* found that $J_{th} \sim 10^{11}$ A/m^2 without H in the CoFe nanowires [119]. Ho *et al.* [120] reported the $J_{th} \sim 2.5\times10^{11}$ A/m^2 without H in 380nm-width FePt nanowire and a $v_{max} \sim 18.4$ mm/s is observed under $J = 2\times10^{12}$ A/m^2. The lower velocity in FePt nanowire compared with permalloy is attributed to poorer polarization and spin transfer efficiency in FePt [121].

Although the permalloy nanowire can exhibit high DW velocity of 100 m/s in the region of 10^{12} A/m^2, current induced DW motion in NiFe nanowires encounters serious obstacles for commercial applications. Firstly, high current density (~10^{12} A/m^2) is required to drive the DW motion in permalloy nanowires. The current density in the order of 10^{12} A/m^2 may degenerate the performance of device due to ohmic heating and cause much power consumption. In addition, the DW width in

IMA thin-film nanowires is large (~100 nm). Particularly, vortex DWs width can extend to 1 μm [117]. The large size of DW will limit the storage density. Moreover, the DWs are very flexible and can transform between transverse and vortex DWs when driven at high current densities [122, 123]. For these reasons, the use of in-plane magnetized materials is not ideal for reliable device operation.

2.3.2 Current induced domain wall motion in perpendicularly magnetized nanowires

Materials with perpendicular magnetic anisotropy (PMA) have attracted much attention because they exhibit narrower DWs (Δ ~10 nm) as compared with IMA (Δ ~100 nm), which are favorable for high density magnetic storage [31]. Some types of the perpendicularly magnetized thin films have been proposed as the promising candidates. One of them is multilayer films, in which interfacial anisotropy contributes to strong PMA caused by the electron orbital hybridization between 3d and 4d electrons. Typical multilayers are Co/Pt [124], Co/Ni [42], CoB/Ni [125] and Co/oxide [77]. In all such multilayers, the thickness of ferromagnetic sub-layer should be less than 1 nm so that the perpendicularly interfacial anisotropy dominates over in-plane shape anisotropy. Co(Fe) based multilayers with noble metals such as Pt and Pd can be deposited at room temperature and exhibited large K_{eff} (~1×10^7 erg/cc). Single layer films with high perpendicular magnetocrystalline anisotropy is another type of PMA films, such as amorphous TbFeCo film [126], $L1_0$-ordered CoPt and FePt films [29, 127]. The $L1_0$-ordered CoPt and FePt exhibit large magnetocrystalline

anisotropy (> 1×10^7 erg/cc) and high temperature annealing stability. Nevertheless, the large surface roughness and relatively high temperature required during the deposition process (> 500 ℃) pose great challenges in fabrication of nanowire devices with CoPt or FePt alloy. In addition, micro-magnetic simulation results [32, 33] predict that the energy barrier required to drive DWs in precessional motion is smaller by an order of magnitude in PMA films than in IMA ones. The intrinsic J_{th} for DW motion through adiabatic torque is then substantially smaller in PMA nanowires.

A large number of experiments on current induced domain wall motion in out-of-plane magnetized structures were carried out in the presence of an external magnetic field. In the PMA materials, the DW is sensitive to the intrinsic local pinning sites due to the DW width is very small and matches the size of pinning sites [128]. In a magnetic film, such pinning may arise from nanoscale defects such as atomic steps, grain boundaries, surface roughness, local variation of the thickness/composition, variation in stress [129]. These lead to random fluctuations of the anisotropy [130] or the exchange interaction. Such pinning strongly affects the DW dynamics for small H, which is then thermally activated and characterized by discrete jumps between metastable states that are separated by the typical length scale between pinning sites (a few tens of nanometers).

In a PMA thin films, two major regimes have been identified depending on the amplitude of H applied along the easy axis according to the depinning field H_{dep} [70, 71]. At low magnetic field ($H < H_{dep}$), the domain wall velocity is described by a creep law [34, 124]:

$$v = v_0 \exp\left[-\left(\frac{U_0}{k_B T_d}\right)\left(\frac{H_{dep}-H_J}{H}\right)^{\frac{1}{4}}\right] \quad (2.11)$$

where v is the DW velocity, v_0 is a velocity prefactor, U_0 is the scaling energy constant, k_B is the Boltzmann constant, T_d is the device temperature and H_J is the effective field from the spin transfer effect. The modified expression is valid in the limit $H_J < H_{dep}$.

For $H > H_{dep}$, the viscous regime is introduced with a velocity proportional to H:

$$v = \mu H \quad (2.12)$$

where μ is the mobility of the DW. The amplitude of H_{dep} depends on the magnetic properties of the material and the amplitude of the pinning strength. In high anisotropy PMA multilayer, H_{dep} usually reaches several tens of mT [131]. Such values can be higher than the Walker field preventing the observation of the steady high mobility viscous regime.

Additionally, the nonadiabatic torque is expected to be a dominate factor for DW motion in the PMA films [31]. The effect of the nonadiabatic torque on the DW dynamics is predicted to be equivalent to an external magnetic field [59, 65, 132] so that the relative changes caused by the current induced DW dynamics can be used to probe nonadiabatic effects. In order to further understand the effect of the nonadiabatic torque, experiments were carried out to explore how current and field affect the pinning potentials of the DW.

It is found that the depinning field (H_{dep}) for driving DW motion strongly dependent on the injected current density *J* in previous reports [40, 89, 133-135] . The H_{dep} linearly decreases with increasing *J*. The slope of the H_{dep} - *J* curve is described

as

$$\epsilon = \mu_0 \Delta H_{dep} / \Delta J \quad (2.13)$$

where ϵ is named as "efficiency". The ϵ obtained in the PMA materials is much larger than it is observed in permalloy (5×10^{-15} T·m^2/A) [136]. According to the dependence of the H_{dep} with *J*, Boulle *et al.* [133] found the $\epsilon = 6\pm1.5\times10^{-15}$ T·m^2/A in the perpendicular magnetized $(Co/Pt)_3$ multilayers nanowire. Using the 1-D DW dynamics simulation, the non-adiabatic torque exerted on the DWs as an effective H can be described [59] as

$$\epsilon = \beta P h / 2 e M_s \lambda. \quad (2.14)$$

where P is the spin polarization, M_s is the saturation magnetization and λ is the domain wall width.

The non-adiabatic efficiency $\beta \sim 0.35\pm0.08$ is derived in the $(Co/Pt)_3$ multilayers nanowire. On the other hand, Fukami *et al.* [134] and Koyama *et al.* [42] observed in narrow (70 – 200 nm) $(Co/Ni)_n$ multilayers nanowire, the J_{th} does not depend on H. This can be explained by a depinning process which is driven by the adiabatic torque in these narrow wires. The adiabatic torque is favor to reduce J_{th} because of the small demagnetizing field in the narrow nanowires. Table 2.1 shows the values of the experimental efficiency (ϵ) and β obtained from current induced DW motion (CIDWM) in the presence of an external H. Burrowes *et al.* observed β = 0.022 ± 0.002 in Co/Ni multilayer and β = 0.06 ± 0.03 in FePt [137]. Feigenson *et al.* found an experimental value of β = 0.48 for $SrRuO_3$ films [138]. Miron *et al.* measured an efficiency $\epsilon = 8\times10^{-14}$ T·m^2/A in a Pt/Co(0.6 nm)/AlO_x multilayer which leads to β =

2.9 [93]. This result can be attributed to the presence of a Rashba spin–orbit coupling (RSO). The RSO is expected in two-dimensional (2D) systems with broken inversion symmetry as in Pt/Co/AlO_x. The RSO leads to a strong effective magnetic field on the conduction electron, whose directions depends on their k vector. As conduction electrons have different k vector on the Fermi surface, this leads to additional spin relaxation and thus enhances β. The presence of a Rashba field in this structure was proved later on by domain nucleation experiments [77] and measurements of the magnetization tilt induced by the Rashba field using the extraordinary Hall effect [139].

Table 2-1. The values of the experimental ϵ and β for different materials obtained from current induced DW motion (CIDWM) in the presence of an external H.

Materials	ϵ (10^{-14} T·m^2/A)	β
$(Co/Pt)_3$ [133]	0.6 ±0.15	0.35 ±0.08
$(Co/Ni)_4$ [137]	1.5	0.022 ±0.002
$SrRuO_3$ [138]	100	0.48
FePt [137]	30	0.06 ±0.03
Pt/Co/AlO_x [93]	8	1.9
Pt/CoFe/MgO [140, 141]	5	4
Pt/Co/Pt [142]	2	0.75

According to the results, one can identify three groups depending on the efficiency. A first one, composed of $(Co/Pt)_n$ and $(Co/Ni)_n$ with extreme values, ϵ is of the order of 10^{-14} T·m^2/A. A second one, composed of $SrRuO_3$ and FePt with narrow DW walls and a much higher efficiency. A third group is composed material with a combination of the spin Hall effect (or Rashba effect) and a strong

non-adiabatic STT, such as Pt/Co/AlO_x [93]， Pt/Co/Pt [142] and Pt/CoFe/MgO [140] with intermediate value of ϵ and high value of β.

Furthermore, it is important to understand the threshold current density (J_{th}) at zero H, since the practical racetrack memory will be used in the absence of H. In practical experiments, the J_{th} to move the DWs in the nanowire is given by [34]:

$$J_{th} \propto \frac{\alpha M_S \lambda}{|\beta - \alpha| P} (H_{dep} - H) \quad (2.15)$$

where H_{dep} is the depinning field for driving the DW motion. A PMA film allows the Bloch-type wall to be formed. The Bloch wall has a very narrow thickness, which can enhance the spin-torque efficient and reduces the critical current density. From the Eq. (2.15), it is also found that, to get a low J_{th}, besides the narrow DW width, a low saturation and a high spin polarization are desirable. Table 2.2 compares some typical materials used for magnetic nanowire devices.

In addition, the nanoscale inhomogeneties present in some PMA films, in particular, the structure defects from interface intermixing have a strong pinning effect on the narrow DWs, resulting in a relatively large threshold H — depinning field (H_{dep}) for driving DW motion. For typical PMA multilayer films, such as Co/Pt [143], Co/Ni [144], generally exhibit a strong H_{dep} > 350 Oe. The strong H_{dep} not only leads to an enhanced stochastic effect, but also requires a rather high driving current density in the order of 10^{12} A/m^2 for current-induced DW motion [36]. As a result, it is important to reduce H_{dep} in order to further decrease J_{th} for future DW application.

Table 2-2. Magnetic parameters of some typical magnetic thin films.

Materials	M_s (emu/cc)	λ (nm)	P (%)	α	Anisotropy	J_{th} ($\times 10^{11}$A/m^2)
NiFe [13, 37]	800	200-600	0.4-0.5	0.05	IMA	30-50
$(Co/Pt)_n$ [40]	600-700	10-20	0.56	0.1	PMA	8-9
$(CoFe/Pt)_n$ [145]	1400				PMA	14.3
$(Co/Ni)_n$ [42, 144]	780	10-30	0.7	0.04	PMA	4.5-6
FePt [137]	1100	1-10			IMA	10-50
TbFeCo [126]	300	4-10	<0.4	0.03	PMA	5
Ta/CoFeB/MgO	1200	10	0.71	0.01	PMA	6.2
Pt/Co/AlO_x [93,	1100	4-5	0.6		PMA	10
Pt/Co/Pt [142, 148]	1200-1300	6-12		0.15	PMA	>5
Pt/$(Co/Tb)_n$ [149]	1500-2000				PMA	1.5

Table 2.3 shows the J_{th}, minimum DW velocity v_{min}, depinning field (H_{dep}), and DW motion direction of some typical PMA materials. The v_{min} is generally obtained by dividing the DW displacement by the length of the pulse. According to the results shown in Table 2.3, the magnetic materials can be classified into different groups. The first group includes ultrathin magnetic multilayer films. J_{th} ranges from 3 to 15×10^{11}A/m^2 due to the variation of H_{dep} in the different films. Another group consists of $SrRuO_3$ and TbFeCo with much lower J_{th} in the range of 10^{10} A/m^2. Although different materials are considered, the result for the multilayer films suggest an approximate dependence of the J_{th} on H_{dep}. Ravelosona *et al.* [34] and Li *et al.* [150] reported in $(Co/Pt)_n$ and TbFeCo nanowires an approximately linear dependence of J_{th} on H_{dep}, which is consistent with a depinning controlled by the nonadiabatic torque. However, a different variation was reported in narrow $(Co/Ni)_{4,5}$ nanowires [42, 144],

where the J_{th} was found to be independent of external pinning nor on the external field.

Koyama *et al.* [42] also studied the dependence of J_{th} on the wire width in the range of 40 to 300 nm. They observe a minimum J_{th} for a given width of the wire corresponding to the transition from a Bloch to a Néel DW where the DW demagnetizing field is minimum. This behavior is clearly consistent with an 'intrinsic pinning' behavior where the depinning process is driven by the adiabatic torque in this case. The J_{th} associated with the adiabatic torque can be lower than the one associated with the nonadiabatic torque for narrow wire due to the small DW demagnetizing field. The nonadiabatic torque plays thus a minor role in these experiments.

The DW moves in the direction of the electron flow are mainly observed by most authors. However, Moore et al. [147] and Lee et al. [151] observed respectively in Pt/Co(0.6 nm)/Al_2O_3 and Pt/Co(0.3 nm)/Pt a DW motion in the direction opposite to the electron flow. In these studies, the nonadiabatic torque was identified to be the main driving force on the domain wall motion. Liu *et al.* [75] utilized the combination of the spin Hall effect to explain this result. The chiral dependency of DWs in ultra-thin PMA films has been proposed to further understand the phenomenon. It is well known that there are two types of DW exist in ultra-thin films, which are Néel and Bloch walls. In Bloch walls, the magnetization is perpendicular to the current direction. However, the relative orientation of the magnetization and current gradually varies in Néel walls. The magnetostatic interaction favors the formation of Bloch

walls. In case of Néel walls, there is no preference of chirality due to the spatial inversion symmetry. However, Ryu *et al*. [83] and Beach *et al.* [84] proposed that there exists a mechanism called Dzyaloshinskii–Moriya interaction (DMI) that breaks the spatial inversion symmetry introducing chirality in the systems they studied. DMI favors the formation of Néel walls over Bloch walls. Together with the spin Hall effect and Slonczewski spin torque, the DMI pushes all of the chiral walls rapidly in the same direction [152]. This provides a revolutionary approach to control domain walls in perpendicular systems.

Table 2-3. The values of J_{th}, and minimum DW velocity v_{min}, depinning field (H_{dep}), and DW motion direction of some typical PMA materials. Direction '-*e*' stands for a current induced DW displacement in the direction of the electron flow, and '*e*' in the direction of the current.

Materials	**J_{th} ($\times 10^{11}$A/m^2)**	**v_{min} (m/s)**	**v_{max} (m/s)**	**H_{dep} (mT)**	**Direction**	**Ref**
$(Co/Ni)_n$	4.5-6	4	60	40-62.5	-*e*	[42, 144]
$(CoFe/Pt)_5$	14.3	1.5	50	70	-*e*	[145]
CoCrPt	10	0.048	0.2	50	-*e*	[97]
$SrRuO_3$	780	10-30	90	10	*e*	[138]
TbFeCo	0.46-0.59	~0.01	40	100-220	-*e*	[126]
$Pt/Co/AlO_x$	10	0.6	400	~10	*e*	[73, 147]
Ta/CoFeB/MgO	6.2	10	50	5	-*e*	[146]
Pt/Co/Pt	0.83-1.8	~10^{-4}	~10^{-2}	No	*e*	[151]
Pt/TbFeCo	1.3	3	80	No	*e*	[153]
$Pt/(Co/Tb)_n$	1.5	0.02	70	No	*e*	[149]

As shown in the Table 2.3, the Co based multilayers film possess high DW velocity. However the J_{th} is still large due to the high H_{dep} in these films. In another

group, although the much lower J_{th} is observed in $SrRuO_3$ and TbFeCo films, the DW velocity is too low to be applied in the future spin-DW devices. On the other hand, when the spin Hall effect is appled to induced DW motion, a high DW velocity with relative low J_{th} have been achieved for DW motion. Therefore, we need to further find out a novel type of materials with both low J_{th} and high DW velocity.

Chapter 3 Experimental details on the growth and characterizations

This chapter describes the fabrication and characterization techniques used to synthesize, characterize and measure the thin films as well as fabricate patterned devices used in this thesis. We introduce the techniques following the processing flow of the devices.

3.1 Thin film deposition by ultra-high vacuum sputtering technique

The ultrahigh vacuum magnetron sputtering [154] are used to grow thin films and deposit the electrodes in our studies. Sputtering is a deposition process using the kinetic energy conversion, in which atoms are ejected from a solid target material and deposit on the substrate through collision of the target generated by energetic particles [155]. In principle, physical sputtering is a momentum transfer process between atoms and ions through collisions in the materials. It is a technique to deposit thin films of target material on the surface of substrates. Sputtered films possess prominent purity, density, adhesion and uniformity.

Figure 3-1 illustrates the basic components of magnetron sputtering system. A strong magnetic field was generated from permanent magnets placed under the target materials. This field causes the travelling electrons to spiral along magnetic flux lines near the targets. This arrangement confines the plasma near the target area without

causing the damage to the thin films being formed on the substrate, and maintains the stoichiometry and thickness uniformity of the deposited thin film. Substrates are firstly placed into the vacuum chamber and the chamber pressure is then pumped down to its process pressure. When applying a large voltage, the inert gas Ar is ionized (e.g. $Ar \rightarrow Ar^{+} + e^{-}$), causing a plasma or glow discharge. The ions from this plasma are accelerated towards to the target materials (the material to be deposited) when a negative charge is applied to the target materials. the target material is bombarded by the accelerated ions through energy transmission and is ejected in the form of neutral particles - either individual atoms, clusters of atoms or molecules. After these neutral particles are ejected, they will travel in the chamber and are deposited as a thin film onto the surface of the substrate. This process is the fundamental principles of the sputtering deposition.

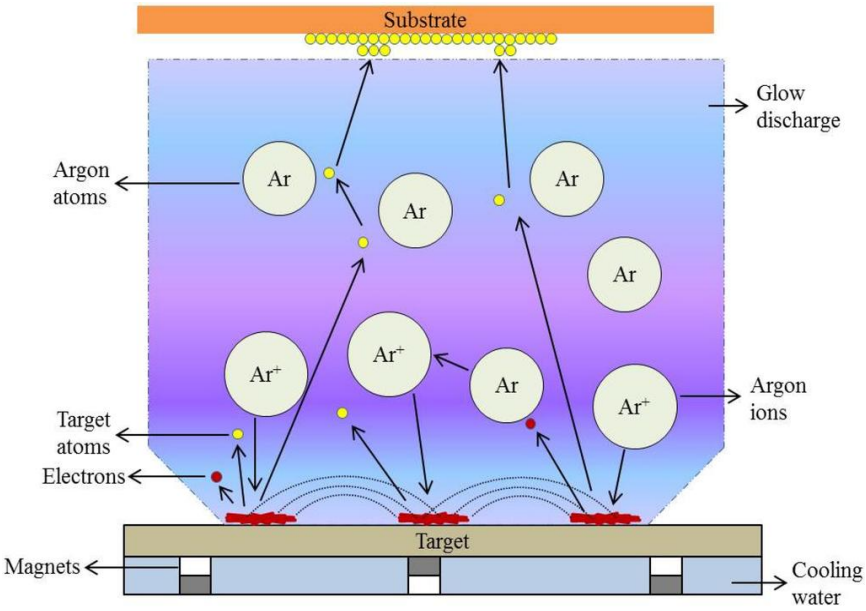

Fig. 3-1 A schematic diagram of the basic components of magnetron sputtering system [156].

In addition, the sputtering technique also offer the chance to deposit oxidized and nitrided alloys either with reactive sputtering methods or with RF guns. The charge

accumulation of the ions on the oxide targets causes the plasma to die off. To avoid this issue, a radio frequency (RF) ac-voltage is applied to the target material to suppress the charges generation on the top surface. However, the RF-power based deposition method provides a very slow deposition rate compared to that of DC-deposition

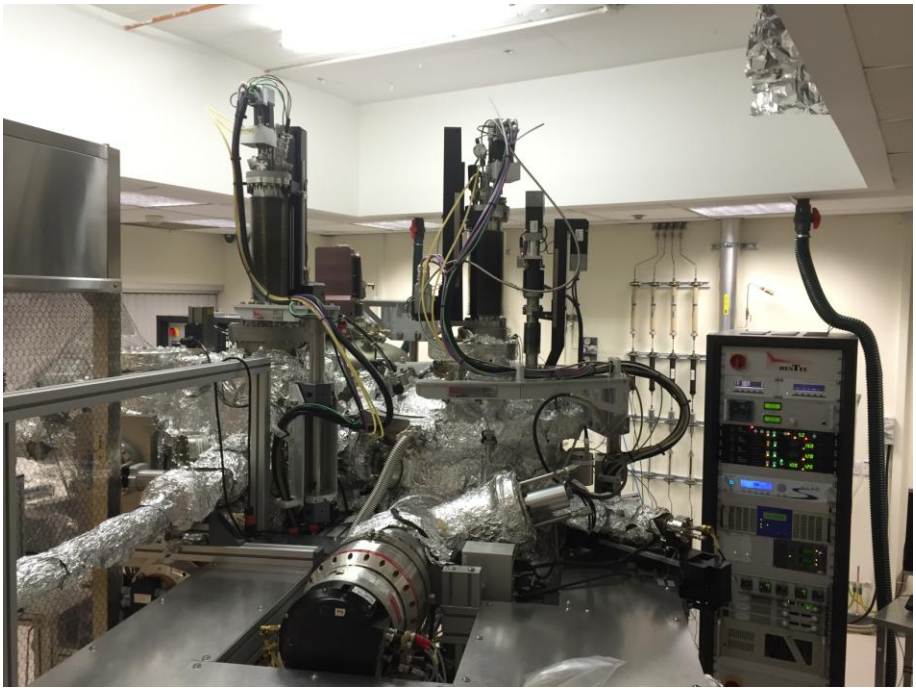

Fig. 3-2 BESTEC Chimera deposition system used for magnetron sputtering.

The sputter tool BESTEC Chimera deposition system as shown in Fig. 3-2 used in our experiment consists of 9 targets deposition chamber. It can be used for either DC or RF sputtering. The RF option allows for the deposition of insulating materials. The base pressure of the system after a bake out is 7×10^{-10} Torr. There is no detectable difference observed between the magnetic properties of our films before or after a bake-out. Therefore, the samples in our experiment are deposited with a base pressure of 2.5×10^{-9} Torr. During sputtering, the Ar pressure in the chamber is fixed

to a constant pressure (typically 1.5 mTorr). The vertical position of the manipulator is set at 130 mm above the substrate to achieve the best uniformity of the film. The manipulator rotation speed is set at 45 rpm.

3.2 Characterization of structural properties

The structural properties of materials can be characterized using XRD and AFM. XRD is used to investigate the lattice structure of sample and the surface morphology can be studied using AFM. The MFM is an essential tool in this thesis since it allows a direct observation of the magnetic domain structure and thus the DWs.

3.2.1 X-ray diffraction (XRD)

X-ray diffraction (XRD) is one of the important techniques to investigate the crystal structure. Figure 3-3 shows the Bragg's Law is the underlying principle for X-ray diffraction. Based on this law, X-rays that are reflected from the adjacent lattice planes will experience constructive interference only when the path difference between them is an integer multiple of the X-ray's wavelength. Bragg's Law is given by

$$2d\,sin\,\theta = n\lambda \tag{3.1}$$

where d is the spacing between the adjacent lattice planes, λ is the wavelength of incident X-ray, n is an integer and θ is the angle between incident X-ray beam and scattering plane.

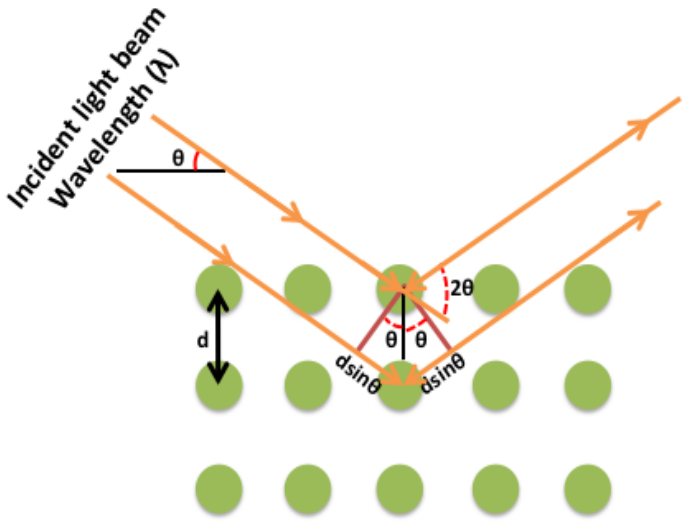

Fig. 3-3 Schematic diagram of Bragg's diffraction law [157].

Figure 3-4 shows basic features of a typical XRD experiment. The XRD experiment includes three primary elements: a sample holder, an X-ray tube, and an X-ray detector. X-ray is produced in a cathode ray tube using the following procedures. Firstly, electrons are generated through heating the filament and then a large voltage is applied to accelerate the electrons toward a target material. X-ray spectra can be generated when electrons have sufficient energy to cast inner shell electrons out from the target material. These X-rays are parallel and directed onto the sample. The intensity of the reflected X-rays is recorded when detector and the sample are rotated. When the geometry of the incident X-rays colliding the sample accords with the Bragg's Diffraction Law, constructive interference appears and a peak in intensity can be detected. A detector records and processes this X-ray signal and converts the signal to the output data for the computer or monitor. The geometry of an X-ray diffractometer is such that the sample rotates in the path of the collimated X-ray beam at an angle θ while the X-ray detector is mounted on an arm to collect the

diffracted X-rays and rotates at an angle of 2θ [158].

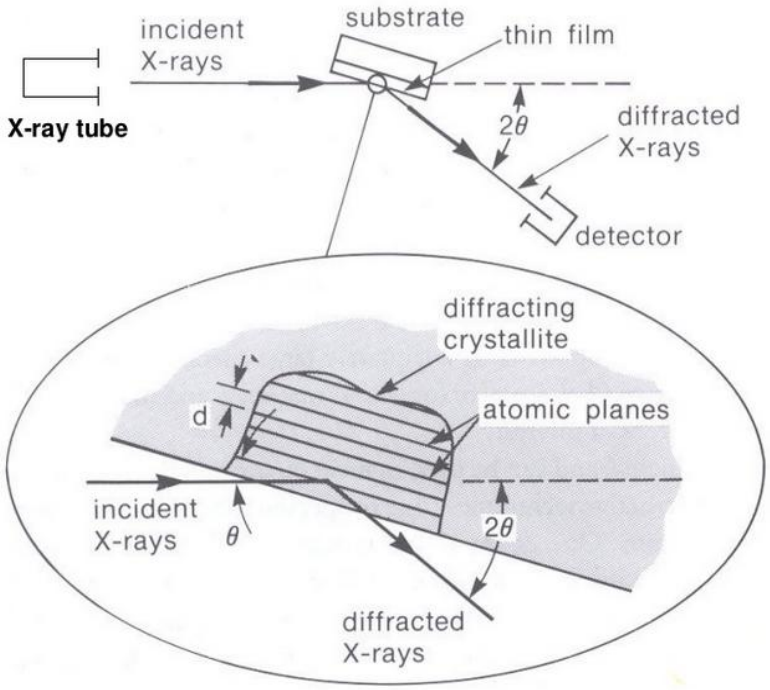

Fig. 3-4 Basic features of typical XRD experiment [159].

3.2.2 Atomic force microscopy (AFM)

The atomic force microscopy (AFM) is one type of scanning probe microscopy with high resolution on the order of fractions of 1 nm. The AFM is used to image the surface of almost any materials with a probe and operate by measuring force between a probe and the sample. Figure 3-5 demonstrates the schematic diagram of AFM. The AFM includes a cantilever with an atomically sharp tip at its end. When the tip is brought close to the surface of sample, an attractive force is generated between the tip and the sample surface. This force causes a deflection of the cantilever based on Hooke's law. As the probe tip scans forth and back above the specimen surface, the tip will rise and fall according to the different features on the surface. The deflection is measured using a laser spot reflected from the top surface of the cantilever into an

array of photodiodes. As the tip goes up and down, the laser hits different parts of the sensor. With the information the sensor collects, an image of the surface can be recreated.

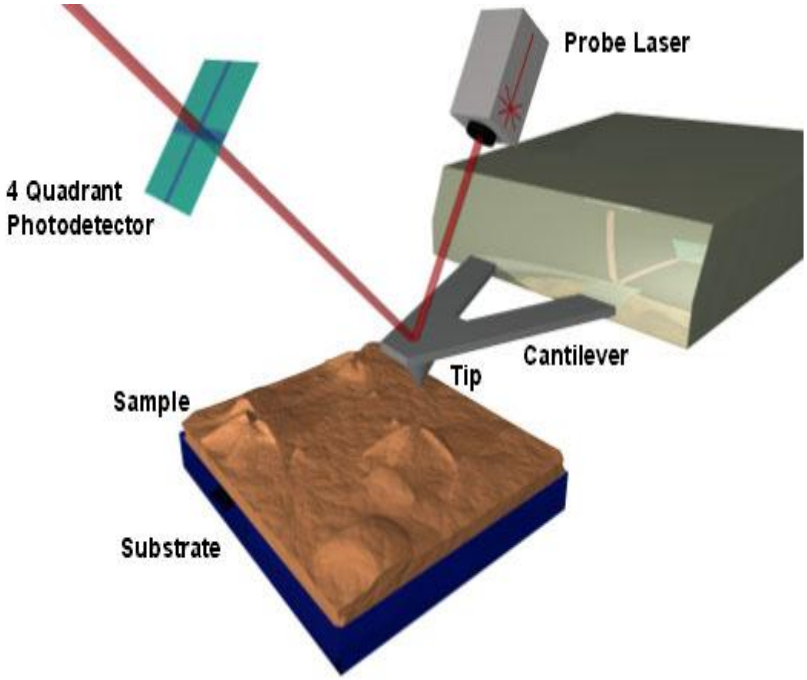

Fig. 3-5 Schematic diagram of AFM [160].

3.2.3 Magnetic Force Microscopy (MFM)

Magnetic Force Microscopy (MFM) as shown in Fig. 3-6 has been used for characterization reading and writing heads as well as recording media due to its ability to provide information about the magnetic configuration in a sample with resolution in the sub-100-nm range. The MFM basic operation is very similar with AFM. Instead of a non-magnetic tip for AFM, a magnetic tip is mounted in a cantilever. When the tip is brought close to the surface of sample, the tip-sample magnetic interaction causes a deflection of the cantilever. This deflection is also measured by using a laser spot reflected from the cantilever into an array of

photodiodes. Piezoelectrics are used to control the position of the sample. MFM characterization of specimens was detected in two steps. In the first step, which is named as "trace", the cantilever utilizes short range forces, such as Van der Waals, to record the topography of specimens. In the second step, which is named as "retrace", the interaction between the stray field of the sample and the magnetic moment of the tip are recorded using the cantilever.

The first "trace" step is usually carried out using a mode known as tapping mode. In this mode the cantilever is oscillated at or close its resonating frequency and the interactions between tip and the surface of the sample cause change in the oscillation amplitude. In order to keep the oscillation amplitude constant, a piezoelectric actuator is used to control the height of the cantilever above the sample. Adjustments made to keep a set cantilever oscillation amplitude reproduce the topography of the surface of the sample. In the second "retrace" step, the changes in the oscillation frequency provide information about magnetic tip-sample interaction. In the MFM, the force from the stray field exerted on the magnetic tip can be modeled by the following equation:

$$F = m \cdot \nabla H_s \tag{3.2}$$

where m is the tip moment and H_s is the field from the sample at the tip. There are two types of tips. In the first type (Type 1), the stray field from the sample does not alter the tip magnetization. In the second type (Type 2), the tip does not show a hysteresis behavior and has a high and constant susceptibility whose moment is directionally proportional to the field experienced. Type 1 tips are usually sensitive to changes in

the out-of-plane direction whereas Type 2 tips can image the in-plane magnetization. However, for this type of tip the application of a bias field is required in order to distinguish the changes in-plane of the magnetization.

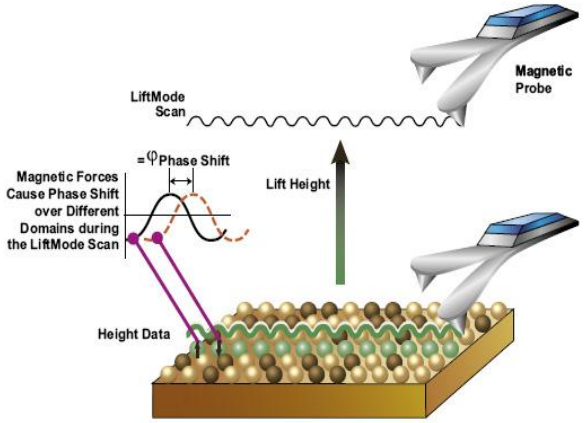

Fig. 3-6 Schematic diagram of Magnetic Force Microscopy (MFM) [161].

The MFM signal at a type 1 tip is given by the expression:

$$F_z = m_z \frac{\partial M_z}{\partial z^2} \tag{3.3}$$

This assumes that the tip is magnetized in the z axis, and thus it has a constant m_z. For the magnetic characterization presented throughout this experiment, a scanning AFM/MFM was used with a standard CoCr tip with a coercivity of 400Oe and a magnetic moment of 1×10^{-13} emu.

3.2.4 Scanning Electron Microscope (SEM)

A scanning electron microscope (SEM) is a kind of electron microscope that generate the image of the specimen by emitting and accelerating a beam of electrons from a source as well as focusing electrons through a sequence of magnetic lenses to interact with atoms in the sample. The focused electron beam scans the sample surface by using scanning coils and these electrons experience repeated absorption

and scattering as they impact to the sample. The interactions with the atoms of sample are explored and utilized to generate the image of sample. The interactions are classified into three types, namely backscattered electrons (elastic, high energy), secondary electrons (inelastic, low energy), and emitted X-rays.

The low-energy secondary electrons are explored to manifest the topography of the sample while scanning the electron beam. This generates an intensity distribution corresponding to the topography of the sample. The high-energy electrons are used to explore the atomic-number of the target materials. Finally, the emitted X-rays are used to obtain the chemical composition of the sample since they originate from element specific electron transitions within the electron shells. The main advantage is the high-resolution specified to be sub-nm and the non-destructive nature of the technique. Figure 3-7 shows a scanning electron micrograph of a device used in our experiment.

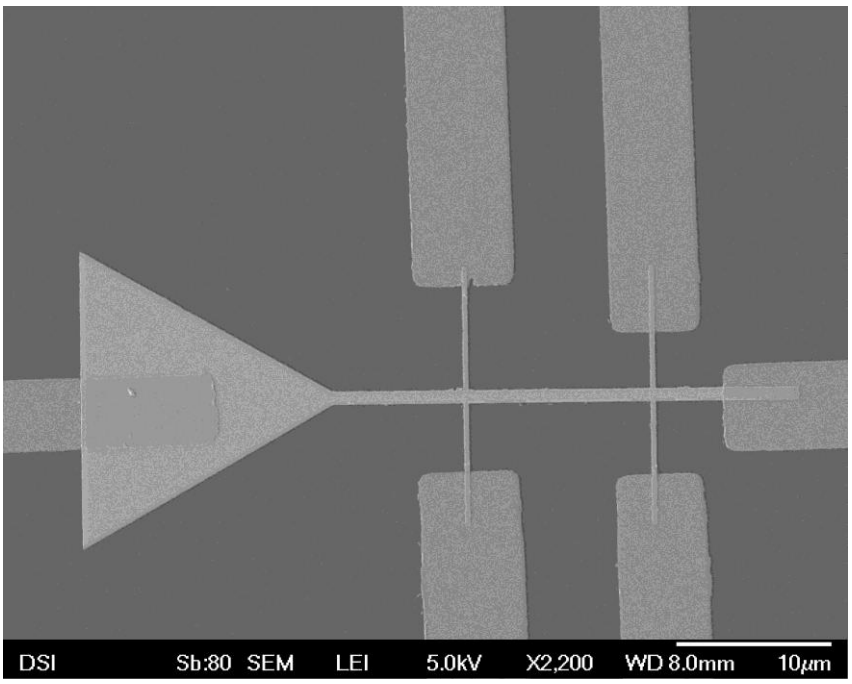

Fig. 3-7 Scanning electron micrograph of a functional device with nanowire width of 800 nm.

3.2.5 Transmission Electron Microscope (TEM)

The TEM allows the imaging of the crystallographic structure of a sample at an atomic scale [162]. The working principle of TEM is similar to that of a light microscope except that electron is used instead of light to achieve atomic resolution. An accelerated beam of electron transmits through the thin specimen to form an image which is magnified and displayed on fluorescent screen or detected using a CCD camera. The transmitted electrons undergo elastic and inelastic scattering which provide crystallographic information such as diffraction patterns and spatial variation in intensity which differentiates crystal defects and secondary phases, respectively. A schematic of a basic TEM system is shown in Fig. 3-8.

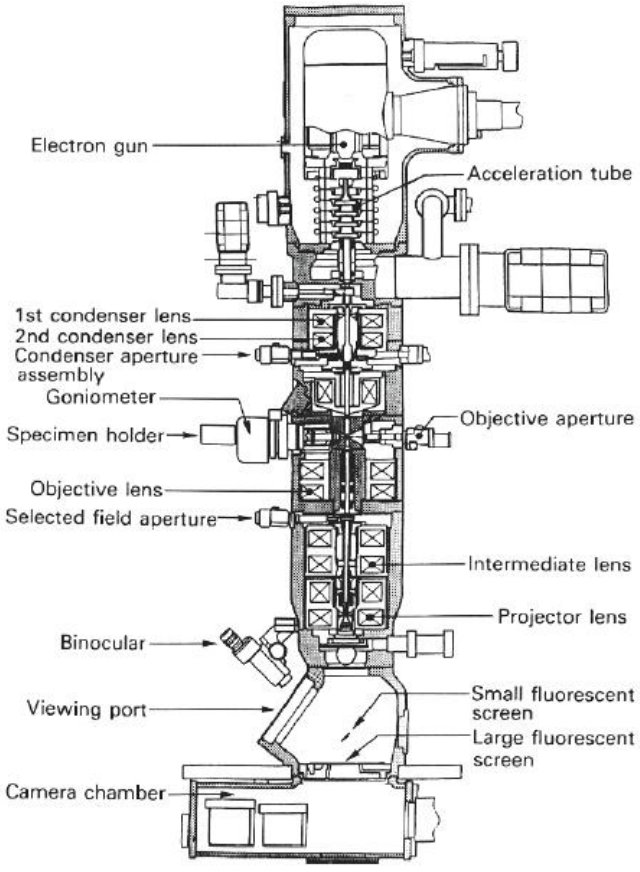

Fig. 3-8 Diagram outlining the internal components of a basic TEM system [162].

In order to determine the crystal structure of each layer the selective-area electron diffraction (SAED) patterns can be analyzed. Electron diffraction patterns can be equated with reciprocal lattice patterns. It is often possible to index an electron diffraction pattern by noting its symmetry. A reciprocal lattice has the same symmetry as its real lattice. The TEM system (JEOL 2300) used was also equipped with EDS which allows elemental analysis. It detects the X-ray emitted when an electron from a higher energy shell fills a lower energy empty shell whose electron has been excited by the incident electron beam. Similar to XPS, it creates spectral lines that are specific to individual elements and thus capable of determining chemical composition and elemental mapping of specific regions.

3.3 Characterization of magnetic properties

3.3.1 Alternating gradient magnetometer (AGM)

The Alternative Gradient Magnetometer (AGM) as shown in Fig. 3-9 allows magnetic measurements on thin film samples. The principle is based on the detection of the oscillation amplitude of a sample fixed on a quartz probe which vibrates in a small alternative gradient field.

The sample is placed at the end of a fiber, then the sample is subjected to a fixed DC field plus an alternating field gradient, generated by and appropriate coil pair. The field gradient produces an alternating force on the sample, which causes it to oscillate and flexes the fiber. If the frequency of vibration is tuned to a resonant frequency of the system, the amplitude of vibration increases by a factor equal to the quality factor Q of

the vibrating system, which can be of the order of 100. A piezoelectric crystal is used to generate a voltage proportional to the amplitude of vibration, which in turn is proportional to the sample moment [14]. The device has a good sensitivity and can measure samples with a total magnetization as small as 10^{-6} emu. Magnetic field can be swept between -2T to 2T. Due to the high resonance frequency (typically some Hz's hundreds) the acquisition time is short (some minutes). The measurements can be done with a field parallel or perpendicular to the film plane.

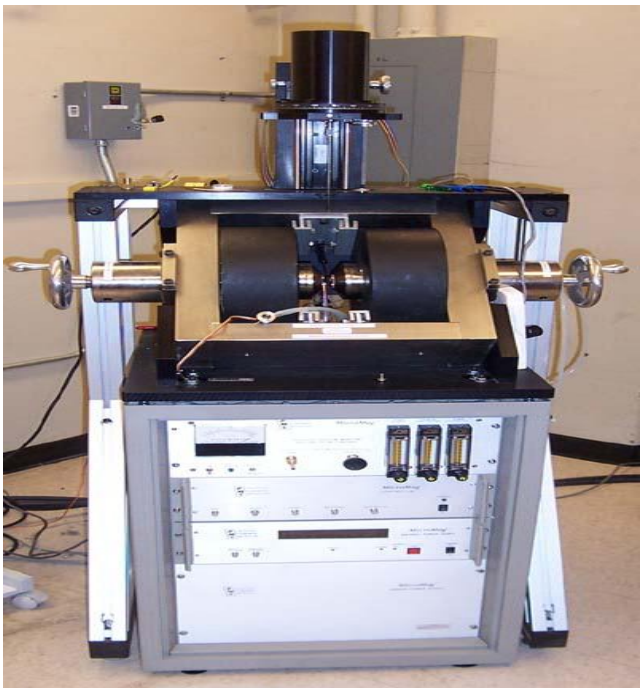

Fig. 3-9 The alternating gradient magnetometer (AGM) system.

3.3.2 Ferromagnetic resonance (FMR)

Ferromagnetic resonance (FMR) is a spectroscopic technique to detect the magnetization of ferromagnetic materials from the magnetic moments of dipolar-coupled but unpaired electrons. It is used for deecting spin dynamics and spin

waves. [163] FMR arises from the precessional motion of the magnetization M of a ferromagnetic material in an external magnetic field H. The H exerts a torque on the sample magnetization which causes the magnetic moments in the sample to precess. The precession frequency of the magnetization depends on the magnetization direction of the material, the strength of the H, as well as the macroscopic magnetization of the sample. [163]

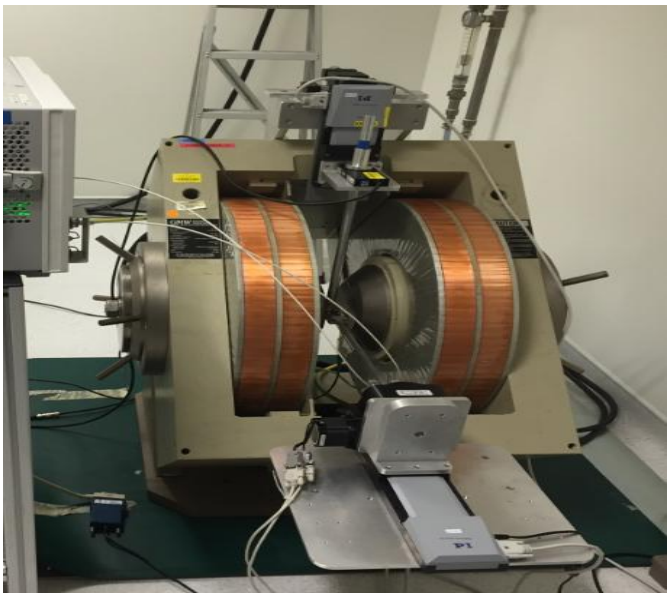

Fig. 3-10 The ferromagnetic resonance (FMR) system.

The basic setup for an FMR experiment is a microwave resonant cavity with an electromagnet as showin in Fig. 3-10. The resonant cavity is fixed at a frequency in the super high frequency band. A detector is placed at the end of the cavity to detect the microwaves. The magnetic sample is placed between the poles of the electromagnet and the H is swept while the resonant absorption intensity of the microwaves is detected. When the magnetization precession frequency and the resonant cavity frequency are the same, absorption increases sharply which is indicated by a decrease in the intensity at the detector.

3.4 Nanofabrication of magnetic nanowire

3.4.1 Electron beam lithography (EBL)

Electron Beam lithography (EBL) is one of most important techniques used in the forming extremely fine patterns at the nanoscale. Briefly, this technique scans a beam of electrons over a surface covered with a resist film (e.g. PMMA). The exposure of the resist film to an electron beam modifies its chemical composition and this makes the exposed areas susceptible to be dissolved in a solvent substance. The latter is known as development of the pattern. The final transfer of the patterns exposed to an electron beam onto a substrate is known as lift-off and takes place after the deposition of a material that reproduces the exposed pattern.

In our experiment, magnetic nanowires are patterned by electron beam lithography, using the Elionix ELS-7700 system as shown in Fig. 3-11. This system is equipped with a ZrO/W thermal field emission electron gun (Schottky emitter). With an acceleration voltage up to 75kV, this fine e-beam system can achieve a minimum feature dimension of 2 nm, which enables us to achieve line widths on the order of 10 nm or less.

Fig. 3-11 Elionix 7700 75kV e-beam lithography system.

3.4.2 Lift-off and etching method

The process flow to fabricate structures using electron beam lithography with etching or lift-off method is depicted in Fig. 3-12. The exposure of a sensitive resist with an electron beam is the core of the EBL process. The resist is often a polymer dissolved in a liquid solvent, which is coated onto a surface and baked to form an even thin layer. During electron beam exposure, the solubility of the resist is altered, causing a dissolution variation with areas that are non-exposed. Following this, the pattern is developed using a liquid developer. Lastly, the combination with processes, like dry or wet etching, lift-off of evaporated material, and/or electro-deposition completes the fabrication of structure. In our study, we mainly use the lift-off method.

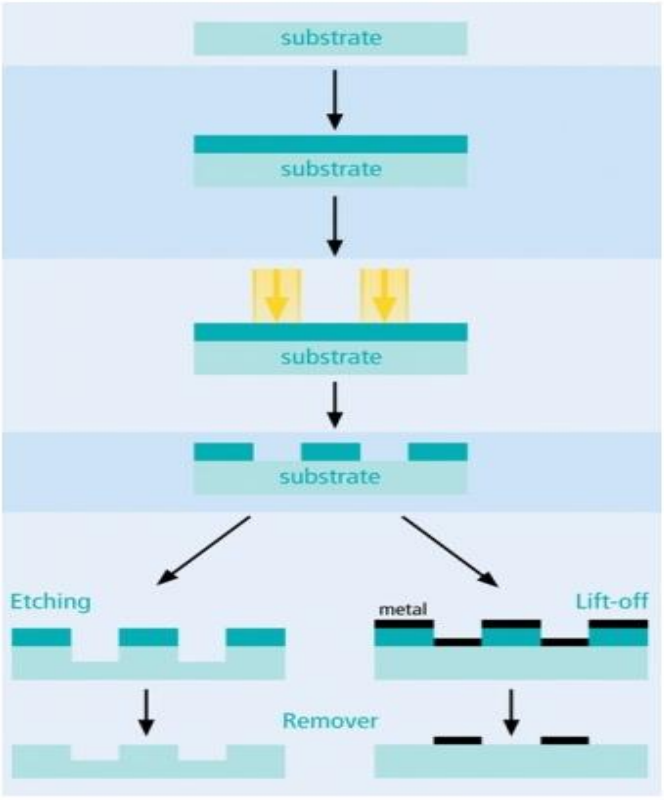

Fig. 3-12 The process flow to fabricate structures using electron beam lithography with etching or lift-off method.

The magnetic nanowires and Hall-bars are fabricated using the following process steps.

1. Sample is cleaned in acetone and IPA for 5 minutes each in an ultrasonic (US) bath.
2. E-beam resist PMMA 495 (polymethyl methacrylate) is applied to cover the plane of the substrate by spin coater. The sample is rotated in the spin coater with a speed of 6000 rmp for 60 s. A hard bake is then performed at 180 ℃ for 180s.
3. E-beam lithography is used to make pattern in the E-beam resist.
4. Sample is developed for 60 s in a mixture of IPA and MIBK (methyl isobutylketone) with a combination ratio of 3:1.
5. After film deposition, sample is immersed in acetone for 1 hour to lift-off the

evaporated material.

3.5 Transport measurement

An electrical transport measurements setup has been built and automated. The setup and its components are shown in Fig. 3-13. It consists of a variable rotatable probe station between the poles of a fixed electromagnet. The magnetic field at the sample can be controlled by a lakeshore electromagnet power supply (Model 648), allowing smooth and fast bi-polar magnetic field control up to 0.7 T. The field is directly measured by a Lakeshore 475 Hall probe mounted on the nearby probe station between the two electromagnets and calibrated to the field at the sample position.

Individual devices can be addressed through a BNC distribution board as shown in Fig. 3-13 (c) where every contact can be connected in parallel to ground (shunted) by a 10 kΩ resistor to prevent electrostatic discharge. A current source (Keithley 6221DC-AC) is used to directly measure the devices. The output signals are measured by a lock-in amplifier (Stanford Research 830) which differentially lock-in to the AC-frequency set by the Keithley 6621 current source. The output of the lock-in amplifier is recorded by a control program for time-resolved measurements. We use another current source (Keithley 6221DC-AC) in the setup to apply pulse current to create the DW in the nanowire.

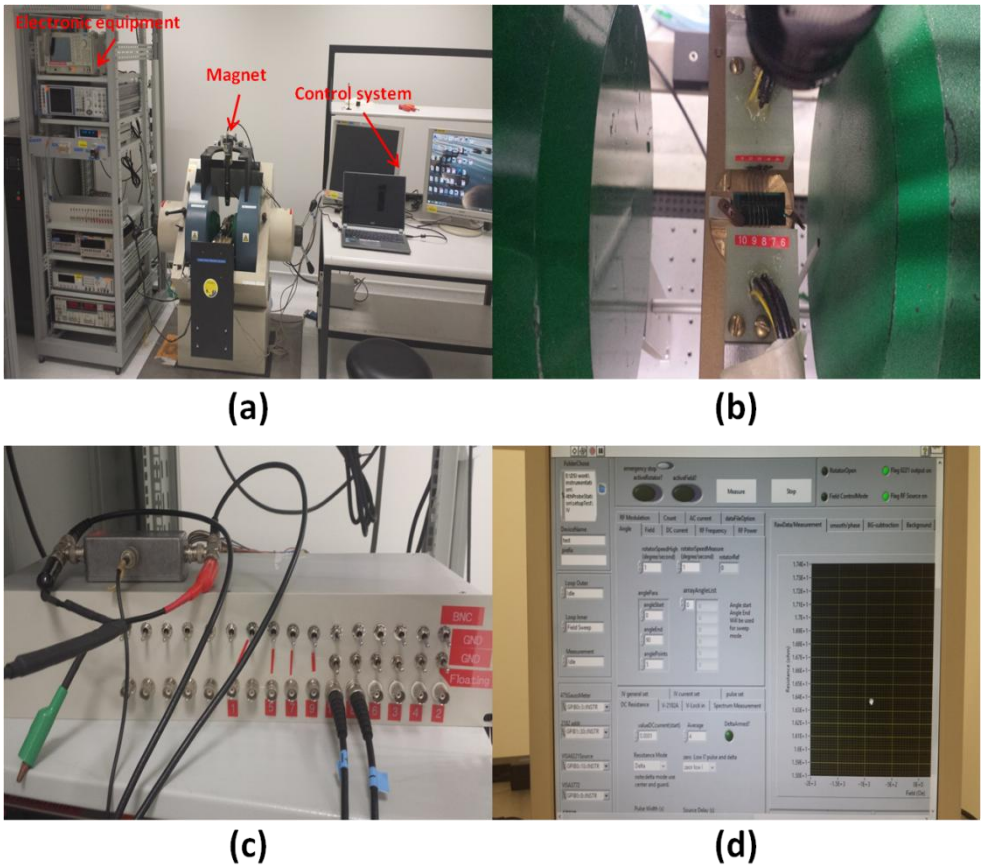

Fig. 3-13 Transport measurement setup: (a) The complete setup of transport measurement systems. Left is electronics rack with the testing instruments, the magnet is in the middle, Right is the control system and the monitor to display the samples; (b) Measurement probe station between the poles pieces of an electromagnet. The sample is placed on the sample holder; (c) BNC distribution board; (d) The control interface displayed on the monitor.

Chapter 4 Characterization of CoFe/Pd multilayers and their application for domain wall motion

In this chapter, we study the magnetic properties of $(CoFe/Pd)_n$ multilayer films as a function of non-magnetic layer Pd thickness. This study highlights the effect of surface/interfacial magnetism to the magnetic properties of the film. In addition, the magnetic properties of $(CoFe/Pd)_n$ multilayer films as functions of magnetic layer CoFe thickness and repeated number *n* are also investigated to understand the optimized PMA. We show that strong effective PMA K_{eff}, controllably low saturation magnetization M_S, narrow DW width λ and high spin polarization *P* can induce low threshold current density for DW motion in CoFe/Pd multilayer films.

Additionally, we demonstrate the motion of magnetic DWs in $(CoFe/Pd)_n$ multilayer nanowire induced by a low current density at a realistic level for practical applications. Nonadiabatic torque with a high non-adiabatic coefficient is ascribed to be the main contribution to the DWs motion.

4.1 Deposition conditions and magnetic characterization methods

In our experiment, CoFe/Pd-based multilayers with the structure of $Si/SiO_2/Ta(3\ nm)/Pd(3\ nm)/[CoFe(t_{CoFe})/Pd(t_{Pd})]_n/Ta(3\ nm)$ were grown on thermally oxidized Si substrates by using DC magnetron sputtering in an ultrahigh vacuum chamber. Figure 4-1 shows a schematic diagram of the stack structure of CoFe/Pd multilayers in our study. The composition of the CoFe layers was fixed at $Co_{70}Fe_{30}$ (at. %). The first set

of experiment was designed to investigate the effects of interfacial magnetic moment on PMA. The t_{CoFe} was fixed at 0.4 nm with n = 6. The t_{Pd} was varied from 1 to 2 nm in step of 0.2 nm (i.e. t_{Pd} = 1.0, 1.2, 1.4, 1.6, 1.8, 2.0 nm). The second set of experiment was carried out to find out the optimized PMA. The t_{CoFe} was varied from 0.25 to 0.5 nm in step of 0.05 nm (i.e. t_{CoFe}= 0.25, 0.3, 0.35, 0.4, 0.45, 0.5 nm) at each t_{Pd} in the range of 1 to 2 nm. The n was varied from 4 to 16 in step of 2. The base pressure was better than 2.5×10^{-9} Torr and Ar working pressure was maintained at 1.5 mTorr during deposition. The magnetic properties of the films were characterized using an alternating gradient force magnetometer (AGM) with a maximum magnetic field of 20 kOe at room temperature.

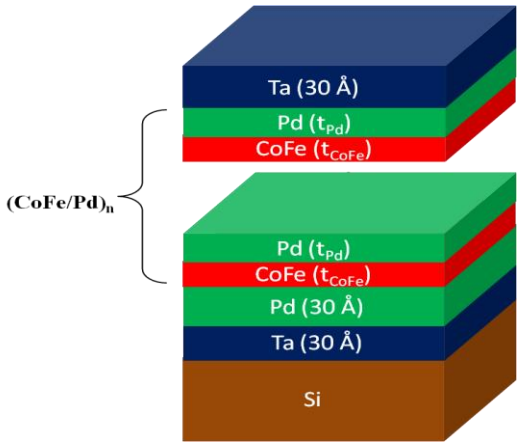

Fig. 4-1 Schematic diagram of the (CoFe/Pd)n multilayers structure.

The X-ray magnetic circular dichroism (XMCD) and X-ray absorption spectroscopy (XAS) at Fe $L_{3,2}$ and Co $L_{3,2}$ edges [164] were conducted by measuring the variation of sample current dependent on photon energy at the SINS beam line under help of Dr. A. Rusydi in the Singapore Synchrotron Light Source (SSLS) . Elliptically polarized light with a degree of circular polarization (DCP) = 80 and an energy resolution of 0.25 eV were employed for the XMCD measurements. In order

to obtain the orbital and spin magnetic moments perpendicular to the plane of film, the incident light was perpendicular to the surface of the sample, and the incident direction is the same as perpendicular magnetization direction of the sample. A magnetic field H of ±10 kOe was applied to magnetize the sample along the perpendicular direction. The XCMD was carried out by varying the direction of H as well as maintaining the helicity of the light. The thin films of Co and Fe were also measured as references to calibrate the XMCD results. The XMCD was measured with spin polarization in the easy-axis magnetization direction of perpendicular magnetic moments by the magnetometer measurements. The LLG micro-magnetic simulator was used to simulate the micro-magnetic domain structure [165].

4.2 Magnetic properties of CoFe/Pd multilayers

Figure 4-2 shows the magnetic-hysteresis (M-H) loops measured on two directions for CoFe(0.4 nm)/Pd(t_{Pd}) multilayers (t_{Pd} = 1.0 — 2.0 nm); parallel (dashed line) and perpendicular (opened cycle) to the plane of the film. The M-H loops measured in the in-plane of the film exhibit a hard axis behavior of the magnetization reversal denoted by S-shape loops. The easy-axis loops as measured in the out-of-plane direction are reflected by the square-shape M-H loops. The smooth M-H loops indicate that unique magnetic properties occur over the film as a single phase behavior due to strong ferromagnetic coupling between the magnetic CoFe layers. These results confirm that the magnetic anisotropy of such CoFe/Pd multilayer has been well aligned normal to the film plane.

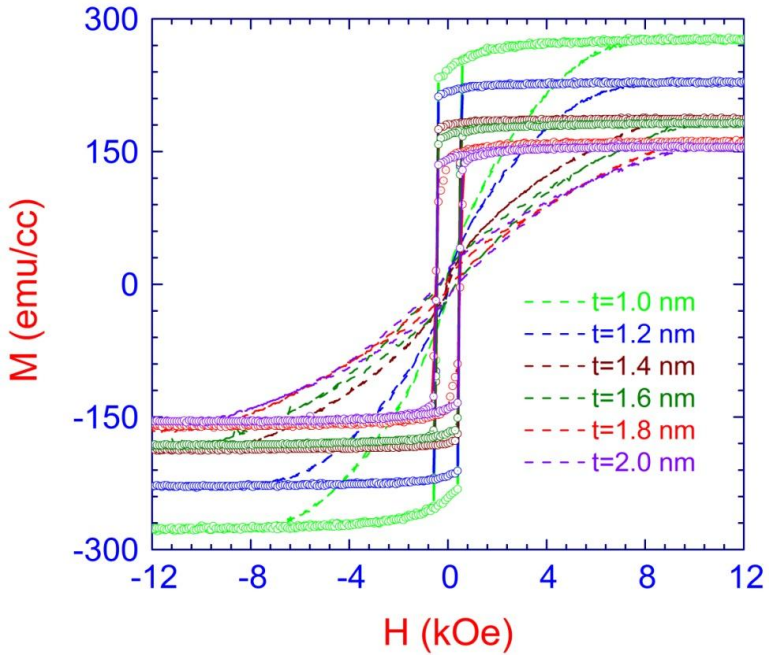

Fig. 4-2 Magnetic hysteresis (M-H) loops of the CoFe/Pd multilayers with different Pd spacing thickness. The loops with circle dots are measured out-of-plane of the films, and the dash lines denote the in-plane loops.

It is noted that $Co_{100-x}Fe_x$ films deposited on Ta/Pd seed layer with Fe concentration above 22% exhibited body-centered cubic (bcc) (110) structure and the magnetic anisotropy of such a film prefer to be IMA [166]. On the other hand, the thick Pd seed layer would cause a fcc (111) texture in the CoFe layer that promote the PMA [167]. Figure 4-3 shows the XRD spectra for Ta(3 nm)/Pd(3 nm)/[CoFe(0.4 nm)/Pd (1.2 nm)]$_6$ multilayers. It has been observed that the CoFe/Pd multilayer samples have primary fcc (111) texture. The Pd seed layer is beneficial to induce fcc (111) texture in the ultra thin CoFe films and generate high PMA for CoFe/Pd multilayers. The previous report [167] have attributed the fcc (111) texture in CoFe layer to the interfacial anisotropy of the CoFe/Pd interface, which is possibly a significant factor dominating the PMA of the CoFe/Pd multilayers.

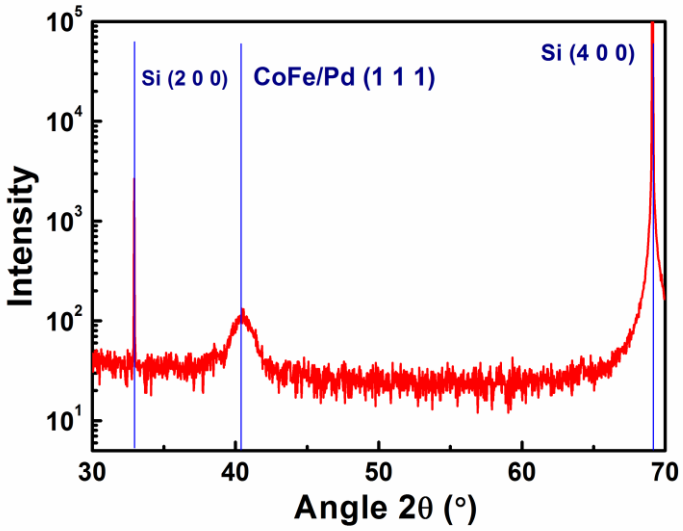

Fig. 4-3 XRD of Ta(3 nm)/Pd(3 nm)/[CoFe (0.4 nm)/Pd (1.2 nm)]$_6$ multilayers.

It is important to know the variation of PMA in the CoFe/Pd multilayers as a function of Pd sublayer thickness. Figure 4-4 (a) shows the saturation magnetization, M_s, of the CoFe/Pd multilayers as a function of Pd sublayer thickness. The value of M_s was obtained through dividing magnetic moment (m) by the total volume of the $Co_{70}Fe_{30}$/Pd multilayers. The reason for using the total volume of CoFe/Pd multilayers in calculating M_s is that the PMA arises from the interface anisotropy, which originates from the spin orbit coupling between CoFe and Pd atoms. The interface anisotropy is dependent on the Pd thickness [168]. Additionally, even for Pd thickness larger than 1 nm, it would affect the interlayer coupling[169] and domain nucleation between adjacent CoFe layers [170], which then influence the M_s and K_{eff}. It is found that M_s reduces with increasing thickness of Pd sublayer. When t_{Pd} = 1 nm, the measured value of M_s is around 280 emu/cc, whereas M_s decreases to 155 emu/cc as the t_{Pd} is increased to 2.0 nm. These values of M_s (155 to 280 emu/cc) are dramatically smaller than that in other common Co-based PMA films, such as Co/Ni

multilayers (660 emu/cc) [25], Co/Pt multilayers (~900 emu/cc) [131], perpendicular magnetized CoFeB/MgO films (1200 emu/cc) [171], but comparable with ferrimagnetic TbFeCo film [126]. The M_s of the studied CoFe/Pd multilayers is definitely much lower than that of pure fcc-$Co_{70}Fe_{30}$ alloy film (1200 emu/cc) [172]. This decrease in M_s can be attributed to the weakening of interlayer ferromagnetic coupling as increasing the distance between adjacent CoFe layers and the variation of the interfacial magnetic moments with t_{Pd}. These factors will be discussed in the Sec. 4.5 with XMCD and XAS measurements.

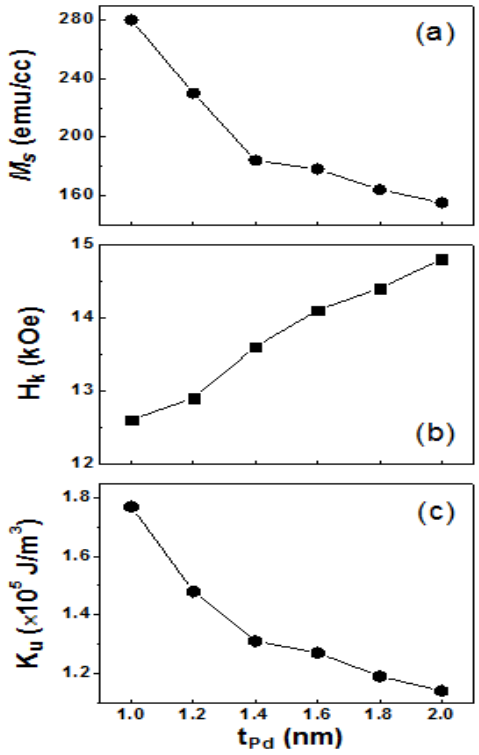

Fig. 4-4 The dependence of (a) the saturation magnetization M_s, (b) anisotropy field H_k and (c) the uniaxial anisotropy K_u as a function of Pd sublayer thickness.

In contrast to the variation tendency of the M_s, the anisotropy field (H_k) increases almost linearly as a function of t_{Pd} as shown in Fig. 4-4 (b) from 12.6 kOe to 14.8 kOe. The H_k can be obtained from the M-H loops as $H_k = H_s + 4\pi M_s$ (H_s is the saturation

field) [146]. From H_k and M_s, the uniaxial anisotropy K_u is determined as $K_u = H_k \cdot M_s/2$. Figure 4-4 (c) shows variation of K_u dependent on t_{Pd}. It is found that K_u decreases with increasing t_{Pd}. As t_{Pd} increases from 1.0 to 2.0 nm, the K_u decreases from 1.77×10^5 J/m^3 to 1.14×10^5 J/m^3.

Additionally, the exchange interaction length can be derived from the value of M_s through the following equation:

$$l_{ex} = \sqrt{2A/\mu_0 M_s^2} \tag{4.2}$$

where A is the exchange constant. Assuming A ~ 10 pJ/m (typically for Co-based magnetic thin films) [46] and M_s varies from 155 to 280 emu/cc, the value of l_{ex} is deduced to be in the range of 7-12 nm. This value is around the overall thickness of the multilayers, confirming the thin magnetic layers are ferromagnetically coupled to each other over the total thickness of multilayers.

It is expected that the non-adiabatic torque plays a dominant role in the narrow DWs due to higher magnetization gradient [31]. The DW width is estimated by using the relation [131] :

$$\lambda \approx \pi\sqrt{A/K_{eff}} \tag{4.3}$$

where K_{eff} is effective perpendicular magnetic anisotropy. The K_{eff} is determined as $K_{eff} = H_s M_s/2 = K_u - 2\pi M_s^2$, where H_s is the anisotropy field which the hard axis and easy axis M-H loops superposed [146]. It can be found that the higher K_{eff} is beneficial to induce smaller λ and higher non-adiabatic torque for driving DW motion. Therefore it is important to study the variation of K_{eff} dependent on t_{CoFe} and t_{Pd} in the CoFe/Pd multilayers.

To further understand the optimized PMA of CoFe/Pd multilayers, K_{eff} and M_s of CoFe/Pd multilayers in the as-deposited state with different thickness of Pd and CoFe sublayers were measured. The repeated number of CoFe/Pd multilayers was fixed at n = 6. The t_{CoFe} was varied from 0.25 to 0.5 nm in step of 0.05 nm (t_{CoFe} = 0.25, 0.3, 0.35, 0.4, 0.45, 0.5 nm) at each t_{Pd} in the range of 1 to 2 nm with step of 0.2 nm (t_{Pd} = 1.0, 1.2, 1.4, 1.6, 1.8, 2.0 nm).

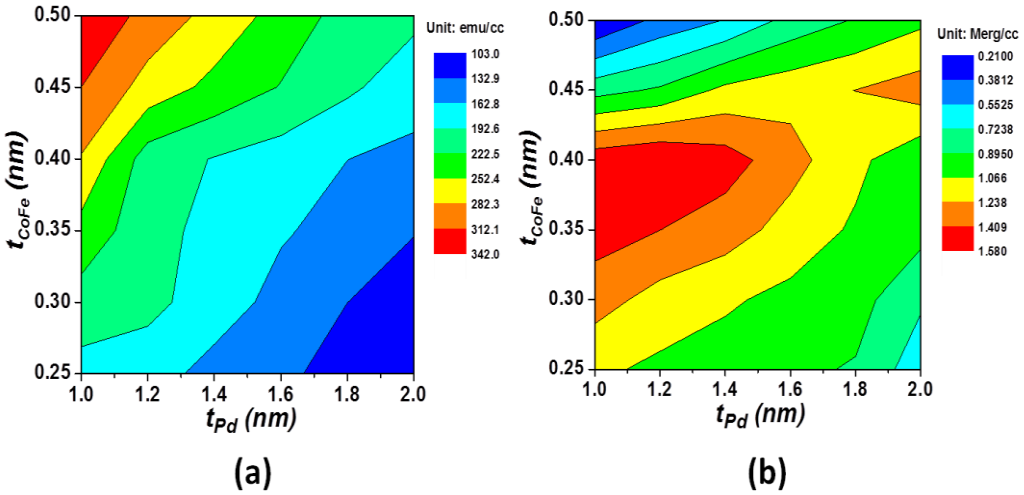

Fig. 4-5 M_s (a) and K_{eff} (b) in [CoFe (t_{CoFe})/Pd (t_{Pd})]$_6$ multilayer samples as a function of the thickness of CoFe sublayer (t_{CoFe}) ranging from 0.25 nm to 0.5 nm and the thickness of Pd sublayer (t_{Pd}) ranging from 1 nm to 2 nm, respectively.

Figure 4-5 (a), (b) illustrate the variation of M_s and K_{eff} in the [(CoFe(t_{CoFe})/ Pd(t_{Pd})]$_6$ multilayers with t_{CoFe} and t_{Pd}. The minimum value of M_s is achieved at t_{CoFe} = 0.25 nm and t_{Pd} = 2nm. On the other hand, the maximum K_{eff} is obtained when t_{CoFe} = 0.4 nm and t_{Pd} = 1.2 nm. When t_{CoFe} > 0.4 nm, the shape anisotropy caused by the CoFe sublayers would enhance the IMA and reduce the interfacial anisotropy induced PMA. Thus, PMA starts to decrease with t_{CoFe} increases beyond 0.4 nm. When t_{CoFe} < 0.4 nm, the total magnetic moment of CoFe magnetic layers is reduced with decreasing t_{CoFe}, which would cause a decrease in K_{eff}. Therefore, when t_{CoFe} = 0.4 nm

and t_{Pd} = 1.2 nm, K_{eff} achieves a maximum value. In addition, M_s = 194 emu/cc with t_{CoFe} = 0.4 nm and t_{Pd} = 1.2 nm, which is still smaller than other Co-based multilayers, such as Co/Ni multilayers (660 emu/cc) [25], Co/Pt multilayers (~900 emu/cc) [131] and perpendicular magnetized CoFeB/MgO films (1200 emu/cc) [171].

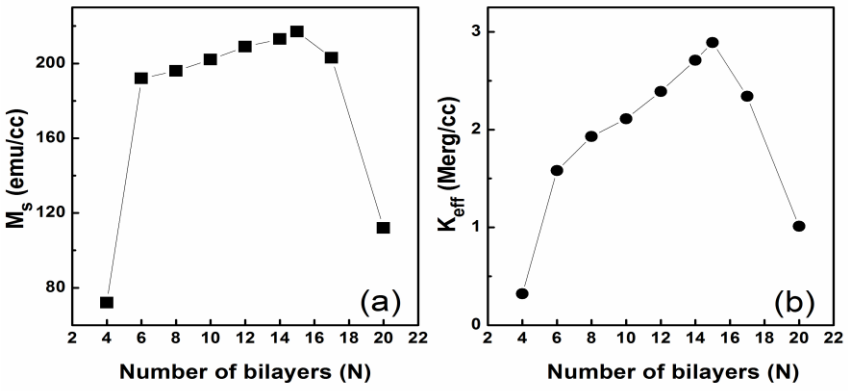

Fig. 4-6 M_s (a) and K_{eff} (b) of [CoFe (0.4 nm)/Pd (1.2 nm)]$_n$ multilayers as a function of n ranging from 4 to 20.

The [CoFe (0.4 nm)/Pd (1.2 nm)]$_n$ multilayers with n ranging from 4 to 20 were deposited to study the effect of n on PMA. Figure 4-6 (a) and (b) show M_s and K_{eff} of [CoFe (0.4 nm)/Pd (1.2 nm)]$_n$ multilayers as a function of n. It is noted that both M_s and K_{eff} gradually increase to their respective maximum values of 228 emu/cc and 2.81×10^6 erg/cc, respectively as n increases from 5 to 15 and then decrease with further increasing n. It is found that PMA is well established in [CoFe (0.4 nm)/Pd (1.2 nm)]$_n$ multilayers films with $n \geq 4$. According to the results shown in Fig. 4-6, the value of M_s changes slightly as n varies from 6 to 18, whereas the value of K_{eff} changes dramatically with n in the range of 6 to 18. The [CoFe (0.4 nm)/Pd (1.2 nm)]$_{15}$ sample exhibits the maximum value of K_{eff}, which is more favorable to reduce

the DW width and increase the efficiency for current induced DW motion. Therefore, the experimental results of the current induced DW motion for the nanowires patterned on [CoFe (0.4 nm)/Pd (1.2 nm)]$_{15}$ films shall be discussed later.

4.3 Micro-magnetic simulations of domain structure

In order to further understand the magnetic anisotropy in our samples, micro-magnetic simulations of domain structure for out-of-plane and in-plane induction components were performed under help of Prof. Michael R. Scheinfein (Arizona State University in Tempe, Arizona). Figure 4-7 illustrates a typical picture of simulated domain pattern in the CoFe/Pd multilayer with t_{Pd} = 1.0 nm at demagnetized state. A stripe-like domain structure is observed in the CoFe/Pd multilayer sample with a well-defined period of about 400 nm. This result is similar to the PMA FePd film previously reported [173], The 400 nm is almost the size of magnetic domains in some Co based PMA multilayers [174]. For the stripe domains, it is significant to consider the quality factor Q, which can be described by the equation [174]:

$$Q = \frac{2K_u}{\mu_0 M_s^2} \tag{4.4}$$

In our CoFe/Pd multilayers, the *Q* factor varies from 3.5 to 7.6. This indicates the anisotropy energy term is dominant to form a sharply defined domain state as shown in Fig. 4-7 (a). Previous reports [173, 175] show that the Bloch-type domain walls extend right up the surface of the films with a weak Néel caps in similar size of the

Bloch walls. It can be found that PMA in the domains is obviously visible via the blue-red color whilst the Néel caps are visualized as the in-plane components located at the domain walls as shown in Fig. 4-7 (b).

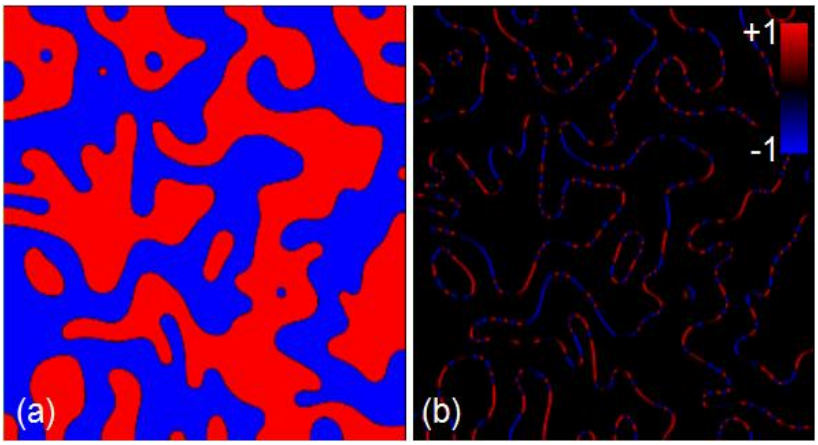

Fig. 4-7 Simulated domain pattern in the CoFe/Pd multilayer with a spacing thickness of 1.0 nm: (a) out-of-plane induction component and (b) in-plane induction components.

4.4 Spin polarization and electronic structure of CoFe/Pd multilayers

In this section, we discuss the spin polarization and electronic structure of the films measured by XAS and XMCD. Figure 4-8 (a) and (b) shows the XAS and XMCD at Fe $L_{3,2}$ (i.e. Fe 2*p* → Fe 3*d* transitions) and Co $L_{3,2}$ edges (i.e. Co 2*p* → Co 3*d* transitions). The transitions are sensitive to spin polarization and electronic structure at the Co 3*d* and the Fe 3*d* bands because of dipole selection rule. Due to the strong core hole spin-orbit coupling, XAS at Co $L_{3,2}$ edges show two main peaks, at ~778 eV for L_3 and ~794 eV for L_2, while XAS at Fe $L_{3,2}$ edges shows two strong peaks, at ~708 eV for L_3 and ~721 eV for L_2 in the CoFe layers. A typical XAS (using circular polarized light with different direction of magnetic field with respect to the normal surface of sample) and XMCD on CoFe layers of the multilayer film with t_{Pd}

= 1.0 nm are shown in Fig. 4-8 (a) and (b). A magnetic field H of ±10 kOe is applied perpendicular to the plane of the film and the XMCD signal is derived by subtracting two XAS signals at the opposite directions of H, which are known as positive and negative fields.

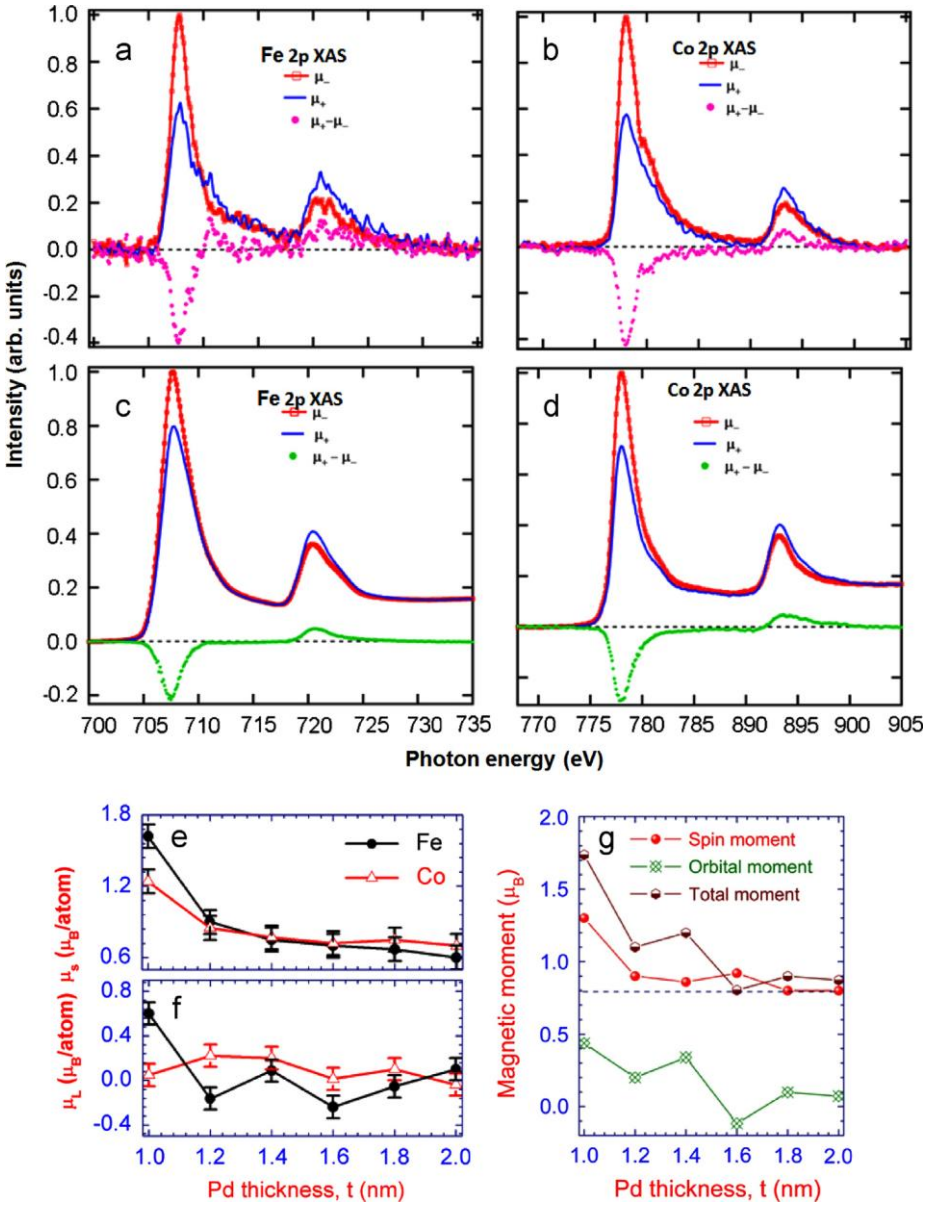

Fig. 4-8 (a,b) X-ray absorption (XAS) and X-ray magnetic circular dichroism (XMCD) spectra of the Fe and Co atoms in the CoFe/Pd multilayer with a spacing thickness of 1.0 nm. (c,d) XAS and XMCD spectra of the Fe and Co atoms in referenced Fe and Co films, respectively. (e) The spin magnetic moment (μ_s) and (f) orbital magnetic moment (μ_L) of Fe and Co atoms as a function of Pd sublayer thickness in the CoFe/Pd multilayers derived from XMCD spectra. (g) Spin magnetic moment, orbital moment and total magnetic moment of $Fe_{70}Co_{30}$ composition as a function of Pd sublayer thickness in the CoFe/Pd multilayers.

We have grown Co and Fe films (~200 nm thick) and used them as reference samples to calibrate and compare XAS and XMCD signals as shown in Fig. 4-8 (c) and (d). In the XMCD signal, strong ferromagnetic properties in the films are observed, which can be referred as two well-defined peaks at both edges, L_3 and L_2 of Co and Fe. This is a strong evidence that the intrinsic ferromagnetism in our CoFe/Pd multilayers essentially comes from the Co 3*d* and Fe 3*d* states. The normalized peak in the XAS signal of the CoFe/Pd multilayer films is the signal (μ_+-μ_-) with pink dotted line in Fig. 4-8 (a,b), which corresponds to the intensity of 0.4 for Co and Fe in the CoFe/Pd multilayer. The normalized peak in the XAS signal of Fe and Co atoms in referenced Fe and Co films is the signal (μ_+-μ_-) with green solid line in Fig. 4-8 (c,d), which corresponds to the intensity of 0.2 for Co and Fe. The intensity enhancement is around two times for Co and Fe in the CoFe/Pd multilayer. This result indicates the strong ferromagnetic interaction between Co-Fe ions in the CoFe lattice. This is well-known as the origin of the high magnetic moment in the Co-Fe alloy system [176].

One of great advantages of XMCD data is its capability to reveal the spin and orbital magnetic moments [177]. By applying the X-ray MCD sum rule [178, 179], we have estimated spin magnetic moment (μ_S) and orbital magnetic moment (μ_L) based on the following equations:

$$\mu_S = -\frac{1}{\cos\theta \times CPD} \times \left(\frac{6\int_{L_3}(\mu_+ - \mu_-)d\omega - 4\int_{L_3+L_2}(\mu_+ - \mu_-)d\omega}{\int_{L_3+L_2}(\mu_+ + \mu_-)d\omega} \right) \times \left(10 - n_{3d}\right) \left(1 + \frac{7\langle T_z \rangle}{2\langle S_z \rangle} \right)^{-1} \quad (4.5)$$

$$\mu_L = -\frac{1}{\cos\theta \times CPD} \times \left(\frac{4\int_{L_3+L_2} (\mu_+ - \mu_-) d\omega}{3\int_{L_3+L_2} (\mu_+ + \mu_-) d\omega} \right) \times (10 - n_{3d}) \quad (4.6)$$

where n_{3d} is the 3*d* electron occupation number, $\langle T_z \rangle$ is the expectation value of magnetic dipole operator, $\langle S \rangle$ is equal to half of the m_{spin} in Hartree atomic units, θ is photon incident angle which is 0^o, and *CPD* is circular polarization degree which is 0.8. Based on band structure calculations [180], the $\langle T_z \rangle / \langle S_z \rangle$ is negligible. From the elementary magnetic moments of Co and Fe atoms, magnetic moments of the $Co_{70}Fe_{30}$ composition in the CoFe/Pd multilayers are calculated by combining those of Co and Fe. The results are shown in Fig. 4-8 (e) - (g).

By normalizing the spin magnetic moment of the CoFe/Pd multilayer films to the reference Co and Fe films, the spin polarization in the CoFe/Pd multilayer films can be estimated. It is assumed that the spin polarization of Fe is 43% [181]. Then, the spin polarization in the studied CoFe/Pd-based multilayers can be qualitatively evaluated to be ~60%, and slightly larger than the spin polarization of the Co-based multilayers (e.g. 56% in Pt/Co multilayer) [182].

Interestingly, the spin magnetic moment and total magnetic moment apparently decrease by varying the Pd spacing thickness as shown in Fig. 4-8 (e) and (g). This is in good agreement with our AGM result as shown in Fig 4-4. In view of the fact that when the thickness of the CoFe magnetic layers is fixed, the decrease in the spin magnetic moment and total magnetic moment can be assigned to the contribution of the interfacial magnetic moment of the CoFe/Pd interfaces, which varies with Pd thickness. This is consistent with the XAS and XMCD results of the Co/Pd

multilayers described above. The magnetic properties were considered to be partially contributed from the hybridization between Pd 4d and Co 3d electrons. The Pd atoms located further away from the CoFe/Pd interface should experience less hybridization and hence less magnetic moment than the Pd atoms located near the interface. If the additional Pd layers are not hybridized as strongly as those at the interface, it will cause the averaged magnetic moment to decrease with increasing Pd thickness [183]. It is noted that XAS and XMCD technique used here is one of the powerful tools to investigate the interfacial properties of the multilayer films.

4.5 Room temperature measurement of domain wall motion

The nanowire with a pattern of 30 μm-long and 300 nm-wide was fabricated on the film with the stack structure of Ta(3)/Pd(3)/[CoFe(0.4)/Pd(1.2)]$_{15}$/Ta(3) (unit in nm) by electron beam lithography and Ar ion-milling. The 300-nm width of nanowire is chosen because the single DW can be formed in the 300-nm-width nanowires as shown by the MFM image in Fig. 4-9.

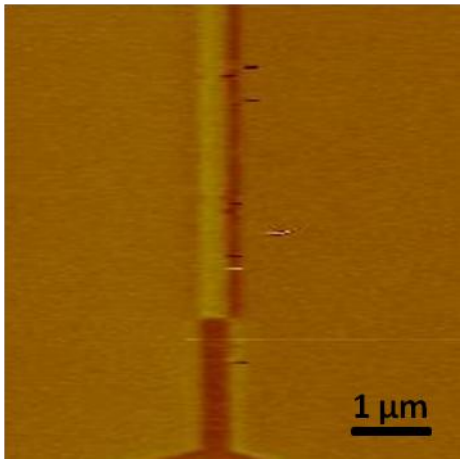

Fig. 4-9 The MFM image showing a single DW is formed at the 300nm-width (CoFe/Pd)$_{15}$ nanowires.

The nanowire structure was then modified with a triangular contact pad and one Hall cross with a width of 300 nm for magnetotransport measurements. The Au electrodes with thickness of 40 nm were deposited on the contact pad and then wired to inject the driving current into the nanowire. The DW motion in the nanowire was detected by means of anomalous Hall effect (AHE) and all measurements were performed at room temperature.

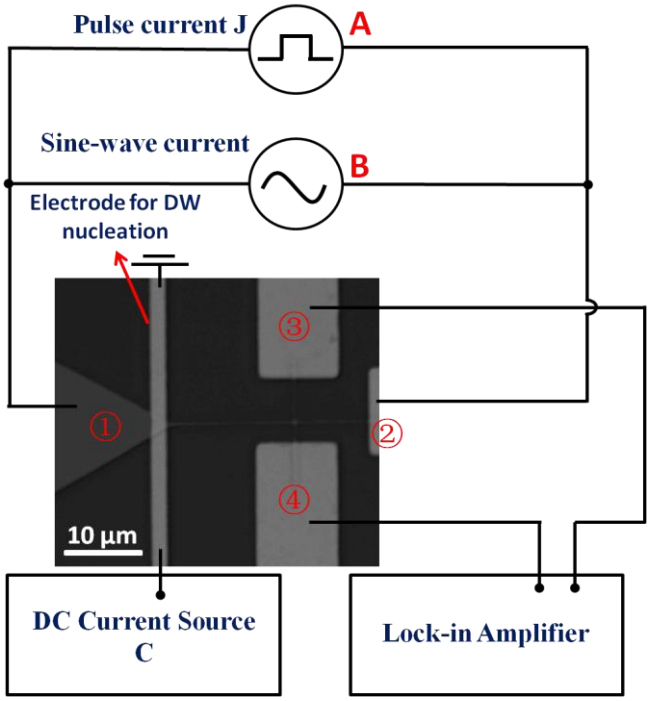

Fig. 4-10 The micrograph of the nanowire device with a width of 300 nm and a schematic diagram of the experimental setup. The Lables 1 to 4 are used to indicate four electrodes, which are connected to the nanowire to detect DW motion through the Hall effect.

Figure 4-10 shows a micrograph of the nanowire device and a schematic diagram of the experimental setup for DW motion measurement. In order to create a single DW in the nanowire, the device was first saturated in one direction using a large positive magnetic field (4000 Oe). The DW was then created in the nanowire using

the local Oersted field generated by applying a large pulsed current from the current source B through the electrode A.

After the single DW was nucleated and pinned at the joint between the triangular contact pad and nanowire, a continuous sine-wave current i_{ac} from the current source A was injected into the nanowire in order to measure the Hall resistance. It was found that the amplitude of i_{ac} = 10 μA with a density in the order of ~ 10^8A/m^2 was too small to drive the DW motion. Next, a pulsed current from the pulse generator together with i_{ac} were injected into the nanowire to drive DW motion under H. The duty cycle and the pulse width (t_p) of the pulse current were fixed at 1/1000 and 5μs, respectively. After each pulse, the lock-in amplifier, which was locked to the frequency of i_{ac}, was used to measure the Hall-effect resistance (R_{Hall}) and detect the DW motion at the Hall cross. The DW velocity is defined as the distance from the electrode to Hall cross (30 μm) divided by the integrated time of current pulses until the switching of R_{Hall} was observed.

4.6 Current induced DW motion at room temperature

Figure 4-11 (a) shows the normalized Hall resistance hysteresis loops (R_H-H) of the CoFe/Pd multilayer nanowire with a width of 300 nm under a sweeping magnetic field (between -1200 Oe and 1200 Oe) perpendicular to the film plane (solid square symbol). The CoFe/Pd multilayer stack structure was Si/SiO_2/Ta(3)/Pd(3)/[CoFe(0.4)/ Pd(1.2)]$_{15}$/Ta(3) (unit in nm). The loop presents a sharp magnetization reversal

behavior and clear squareness, indicating that the magnetization easy-axis is perpendicular to the plane of film and the nanowire has a PMA feature.

In order to determine the H_{dep}, which is the field required to depin the DW from the pinning site [133], the field-switching experiment with DW was conducted as follows. First, DW injection process mentioned above was applied to create and pin the DW in the nanowire as shown by the MFM image in Fig. 4-11 (b). The R_{Hall} was then measured with sweeping H from 0 to -1200 Oe in order to detect the DW motion only under the effect of H. As shown in Fig. 4-11 (a), when the amplitude of H is increased to 755 Oe, the sharp switching of R_{Hall} is observed (solid cycle symbol). We have measured the field-switching experiment 10 times for both positive and negative magnetic field directions and the switching field of 755 ± 1.6 Oe is derived and fixed for both directions. The result indicates that the required H for the DW overcomes the pinning strength and moves freely along the nanowire is $H_{dep} = 755 \pm 1.6$ Oe.

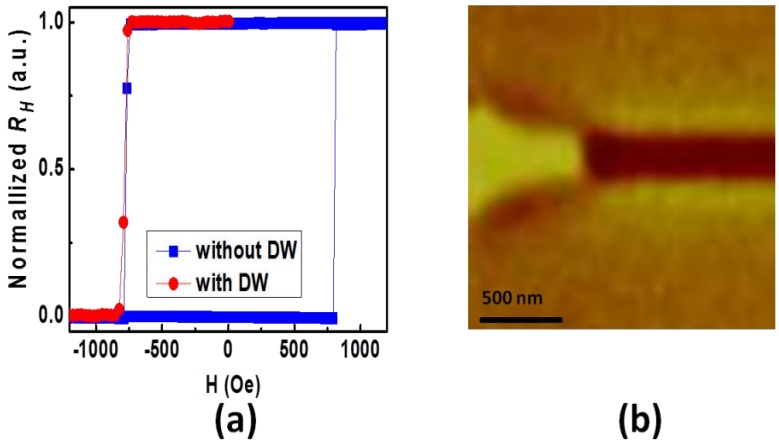

Fig. 4-11 (a) Normalized Hall resistance hysteresis loops (R_H-H) of $(CoFe/Pd)_{15}$ multilayer nanowire with a width of 300 nm under a sweeping magnetic field perpendicular to the film plane without the driving pulse current (solid square symbol); The variation of R_{Hall} under the magnetic field H sweeping from 0 to -1200 Oe for the nanowire after DW injection process (solid cycle symbol); (b) The MFM image shows that the DW was formed by local Oersted field of the injected pulse current at the end of the nanowire.

In addition, the H_{dep} is identical with the previous switching field for R_H-H loop of the nanowire (solid line with solid square symbol in Fig. 4-11 (a)). This can be explained as follows. When H is swept from 1200 Oe to negative field, the nucleation spots and DWs are easily form in the pad prior to the appearance in the wire area due to the shape anisotropy [147, 184] and the nucleation field is smaller than H_{dep}. As H is further increased to H_{dep}, the nucleated DWs in the pad depin from the pinning sites and propagate across the entire nanowire. Therefore, the switching field of R_H-H loop is the same as H_{dep}.

In order to study the effect of the spin polarized current on the DW motion after DW injection, the R_{Hall} as a function of number of driving current pulses under fixed bias magnetic field of 750 Oe (< H_{dep} of 755 Oe) are monitored. Figure 4-12 shows the normalized R_{Hall} as a function of the integrated pulse duration (t) with different current densities and polarities under H = 750 Oe ($t = t_p \times$ pulse number). The positive and negative signs of current density denote the current directions are along and opposite to the DW motion direction (from the electrode A to the Hall cross), respectively. The sudden jump of R_{Hall} as shown in Fig. 4-12 indicates that the spin polarized current facilitates the single DW to depin from the pinning site and drive the DW to move along the nanowire and passes through the Hall cross with H = 750 Oe. The switching of R_{Hall} can only be observed with negative injected current densities. The result indicates that the DW moves in the direction of electrons flow. In addition, it is evident that the switching time for R_{Hall} decreases with increasing current density. This demonstrates that the DW velocity is enhanced by the driving current, which will

be discussed later.

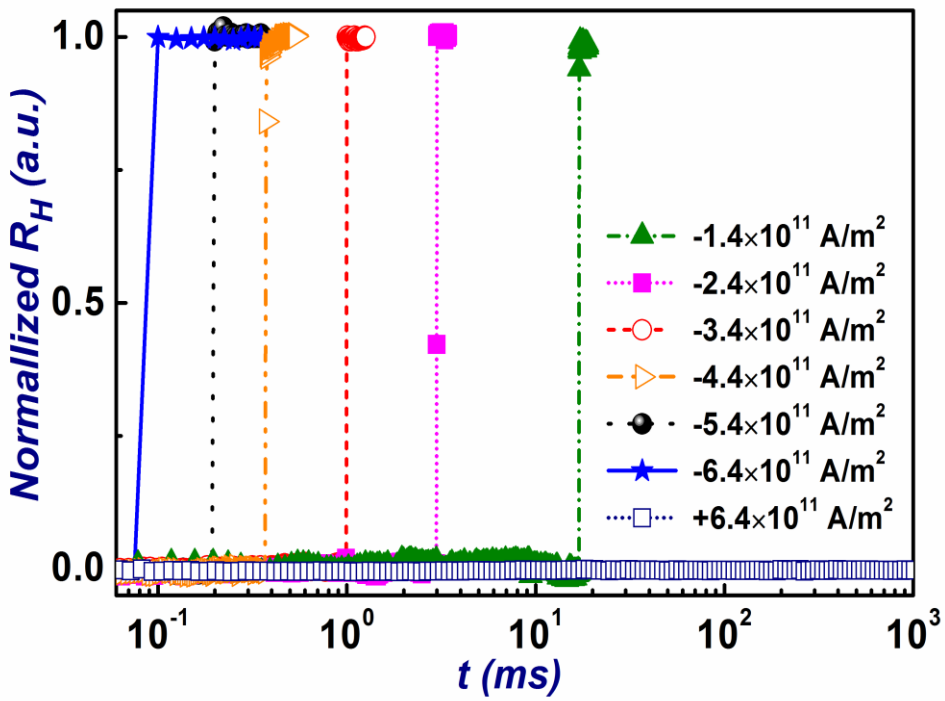

Fig. 4-12 The R_{Hall} as a function of integrated pulse duration t with the different current densities for both current polarities under H = 750 Oe when the multiple pulsed current with t_p=5μs was injected into the nanowire (t= t_p × pulse number). The value of the driving current is ranged from 1.4×10^{11} A/m^2 to 6.4×10^{11} A/m^2. The "+"and "-" symbols mean that the DW is in the same or opposite direction to the current direction, respectively.

Figure 4-13 (a) shows the dependence of the averaged DW velocity (*v*) on driving current density (*J*) measured under H of 750 Oe. It can be found that the *v* increases from 2 μm/s when $J = 1.4\times10^{11}$ A/m^2 to the maximum value of 0.3 m/s with $J = 6.4\times10^{11}$ A/m^2. In addition, it is found that when *J* is below 1.4×10^{11} A/m^2, such as $J = 1.3\times10^{11}$ A/m^2, $v = 0$. This suggests that the DW would not move towards the Hall cross because the effective field generated by both applied pulse current and H are not high enough to depin the DW. We therefore define the threshold current density (J_{th}) as the lowest value of the spin current density to be sufficient to depin the DW from the pinning site and drive the DW to move along the nanowire [184]. Thus J_{th} =

1.4×10^{11} A/m^2 under H = 750 Oe for current induced DW motion in $(CoFe/Pd)_{15}$ multilayer nanowires.

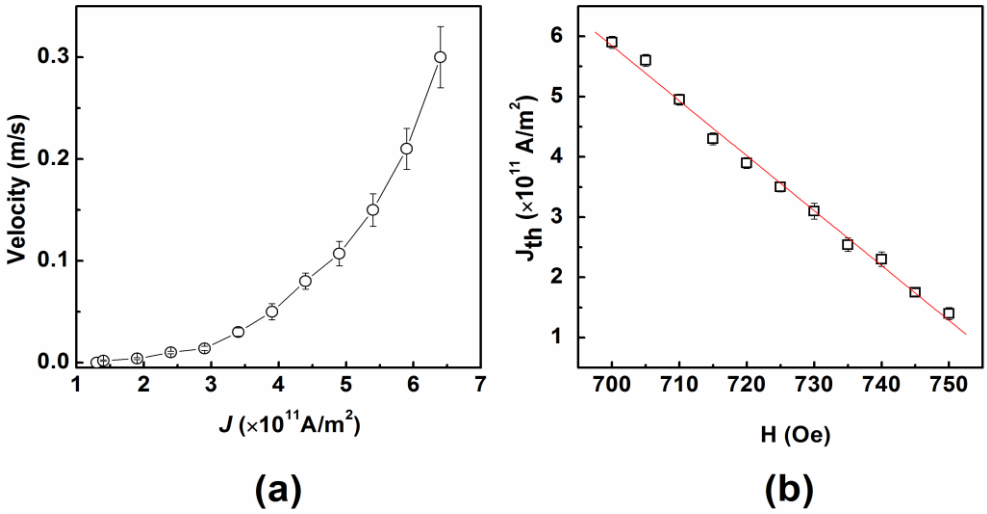

Fig. 4-13 (a) The averaged DW velocity as a function of driving current densities (J) ranging from 1.3×10^{11} A/m^2 to 6.4×10^{11} A/m^2 under H of 750 Oe. (b) J_{th} as a function of magnetic field H. Each data point is the average value of 10 measurements at each current density and magnetic field. The error bars denote the standard deviation of the mean value.

Figure 4-13 (b) shows the variation of J_{th} as a function of H. It is found that the J_{th} decreases linearly with H indicating the spin polarized current produces a field-like effect to assist DW depinning. It is noticed that an even higher J_{th} (~ 7×10^{11} A/m^2) is required for the DW depinning as H is further decreased below 700 Oe. Thus we only show the data for H > 700 Oe since such a high current would burn out the device easily due to the overloading of Joule heating. In order to quantitatively extract the value of spin-torque efficiency, the current-field equivalence model [133] is used. In this approach, the spin-torque efficiency ε can be obtained from the slope of the linear dependence of H on J_{th} ($\epsilon = \Delta H/\Delta J_{th}$) [40]. A value of ε = (1.12 $\pm$ 0.06) $\times10^{-14}$ T m^2/A is derived from Fig. 4-13 (b). If only the non-adiabatic STT effect is dominated

for the DW motion in CoFe/Pd multilayers, a high value of nonadiabatic efficient β = 0.42 $\pm$0.02 can be deduced from the formula [133] $\epsilon = \frac{\beta \mathrm{Ph}\pi}{2\mathrm{eM_s}\lambda}$, which is higher than it is commonly found in other Co-based multilayers, for example β = 0.35 in Co/Pt multilayer film [40]. However, it is known that Ta can generate a strong spin Hall effect (SHE) in some multilayer systems [78, 84]. In the present work, the ultrathin CoFe/Pd multilayer is sandwiched between the top and bottom Ta interfaces and the thickness of top and bottom Ta layers are identical (3 nm). Although the SHE-driven spin torques generated from the top and bottom Ta layers are in opposite directions, the SHE from Ta can not be easily canceled out. Therefore the spin orbit torque (SOT) generated by the SHE in the Ta(3)/Pd(3)/[CoFe(0.4)/Pd(1.2)]$_{15}$/Ta(3) sample will be quantified in the following section.

4.7 Spin orbit torque (SOT) effect on DW motion

In order to quantify the SOT separately, the harmonic Hall voltage measurement with planar Hall effect correction [140, 141, 185-188] are performed for obtaining the first harmonic (V_ω) and the second harmonic ($V_{2\omega}$) Hall voltages. We defined the longitudinal (transverse) direction as the direction along (transverse to) the applied current as shown in Fig. 4-14.

An AC current produces a periodic torque on the magnetized films and causes the z-component of the magnetization (M_z) to change at the driving frequency (ω) [187]. The V_ω and $V_{2\omega}$ are measured with the sweeping external magnetic field along the longitudinal (H_L) or the transverse (H_T) direction. The effective fields with planar Hall

effect correction along the H_L and H_T directions can be obtained from the measured V_ω and $V_{2\omega}$ based on the following expression[186, 188]:

$$\Delta H_{L(T)} = -2\frac{B_{L(T)} \pm 2\xi B_{T(L)}}{1-4\xi^2}, \tag{4.7}$$

where

$$B_{L(T)} = \frac{\partial V_{2\omega}}{\partial H} \Big/ \left.\frac{\partial^2 V_\omega}{\partial H}\right|_{H\,//\,L(T)}. \tag{4.8}$$

The ξ is defined as the ratio of the planar Hall and anomalous Hall resistance ($\Delta R_P/\Delta R_A$), and the $\pm$ sign corresponds to the direction of the out-of-plane magnetization ($\pm M_z$).

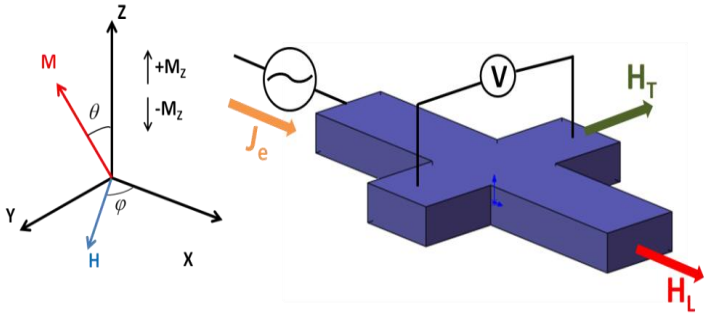

Fig. 4-14 Schematic of experimental setup for measuring the spin-orbit-torque effective fields in both of the longitudinal (H_L) and the transverse (H_T) directions.

We performed the measurements at a fixed frequency f = 133.369 Hz and in the in-plane magnetic field of ± 40 mT. Eq. (4.7) is derived based on the anomalous Hall effect (AHE) and planar Hall effect (PHE) for out-of-plane magnetization system. H_T or H_L varies from -40 mT to 40 mT. Figure 4-15 (a) and (b) show the variations of V_ω and $V_{2\omega}$ as functions of H_L at a current density $J = 3 \times 10^{11}$ A/m^2 for Ta(3)/Pd(3)/[CoFe(0.4)/Pd(1.2)]$_{15}$/Ta(3) (unit in nm) sample, measured both for $\pm M_z$. Figure 4-15 (c) and (d) show the corresponding data for H_T.

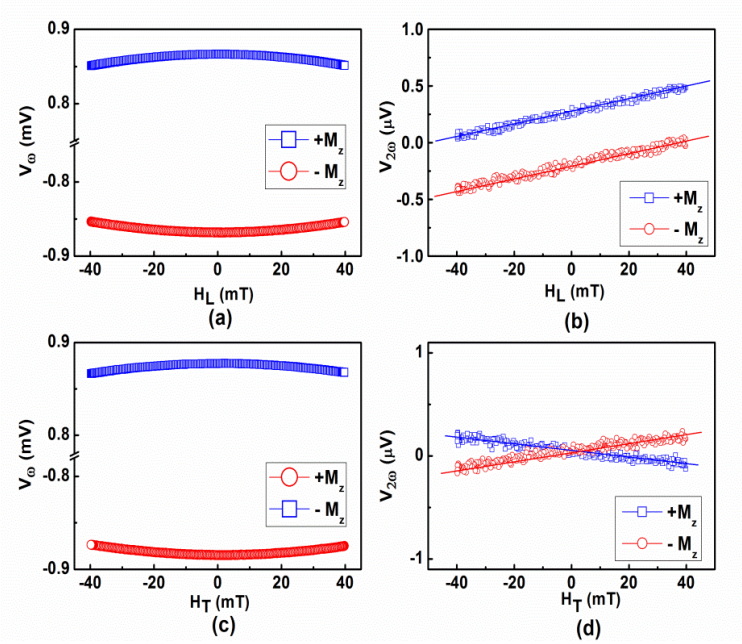

Fig. 4-15 The variation of first harmonic, V_{ω} (a, c) and second harmonic, $V_{2\omega}$ (b, d) Hall voltage as a function of the sweeping magnetic field along either the longitudinal, H_L (a, b) or the transverse, H_T (c, d), direction for the Ta(3)/Pd(3)/$(CoFe/Pd)_{15}$/Ta(3) sample (unit in nm) under $J = 3 \times 10^{11}$ A/m^2.

In order to evaluate ξ value, we performed the planar Hall effect (PHE) correction measurement. Both of the anomalous Hall effect (AHE) and planar Hall effect (PHE) contribute to the spin-orbit torques (SOTs) in the harmonic Hall voltage measurements [140, 186, 187]. Therefore we need to evaluate the AHE and PHE contributions and add the PHE correction to the harmonic Hall SOT measurements.

The ΔR_P and ΔR_A are defined as AHE and PHE resistance, respectively. The measured transverse Hall resistance R_{XY} can be expressed [186, 187] as

$$R_{XY} = \frac{1}{2}\Delta R_A \cos\theta + \frac{1}{2}\Delta R_P \sin^2\theta \sin 2\varphi \qquad (4.9)$$

where the first and second terms are AHE and PHE contributions, respectively. It can be found that when $\varphi = 0°$,

$$R_{XY}^{0} = \frac{1}{2}\Delta R_A \cos\theta \tag{4.10}$$

when $\varphi = 45°$,

$$R_{XY}^{45} = \frac{1}{2}\Delta R_A \cos\theta + \frac{1}{2}\Delta R_P \sin^2\theta \tag{4.11}$$

We define

$$P_{XY}^{0} = \frac{2R_{XY}^{0}}{\Delta R_A} = \cos\theta \tag{4.12}$$

and

$$P_{XY}^{45} = \frac{2R_{XY}^{45}}{\Delta R_A} = \cos\theta + \frac{\Delta R_P}{\Delta R_A}\sin^2\theta . \tag{4.13}$$

Therefore, we obtain

$$\Delta P_{XY} = P_{XY}^{45} - P_{XY}^{0} = \frac{\Delta R_P}{\Delta R_A}\sin^2\theta = \frac{\Delta R_P}{\Delta R_A}\left[1-(P_{XY}^{0})^2\right] \tag{4.14}$$

Figure 4-16 (b) shows the plot ΔP_{XY} as a function of 1- P_{XY}^2 using the data in Fig. 4-16 (a). From Fig. 4-16 (b), the slope gives $\Delta R_P/\Delta R_A = \xi = 0.32$. The same measurement is performed for Ta(3)/Pd(3)/$(CoFe/Pd)_{15}$/Ta(3) sample and $\xi \sim 0.32$ is also obtained. In this case, the PHE correction cannot be ignored and should be taken into consideration.

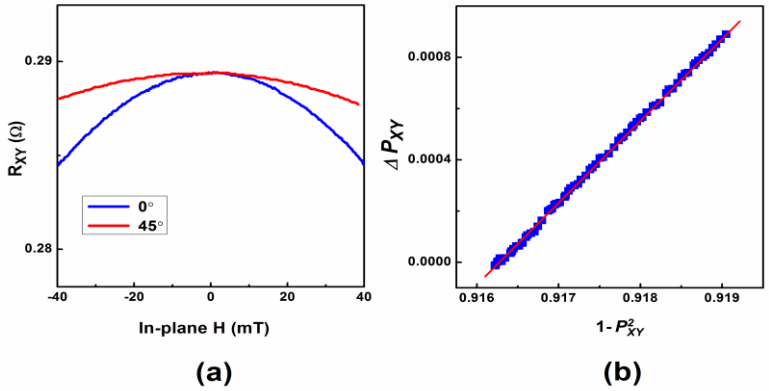

Fig. 4-16 (a) The dependence of Hall resistance R_{XY} on the in-plane magnetic field (H) oriented at $\varphi = 0°$ and $\varphi = 45°$ for Ta(3)/Pd(3)/$(CoFe/Pd)_8$/CoFe/Ru/Pd/$(CoFe/Pd)_9$/Ta(3) sample; (b) The dependence of ΔP_{XY} on 1- P_{XY}^2.

By using Eq. (4.7), we obtain the ΔH_L and ΔH_T under different charge current density (J) with a planar correction. Figure 4-17 (a) and (b) show the variation of ΔH_L and ΔH_T as function of J for Ta(3)/Pd(3)/$(CoFe/Pd)_{15}$/Ta(3) sample, respectively. The dependence of ΔH_L and ΔH_T on J can be used to evaluate the SOT.

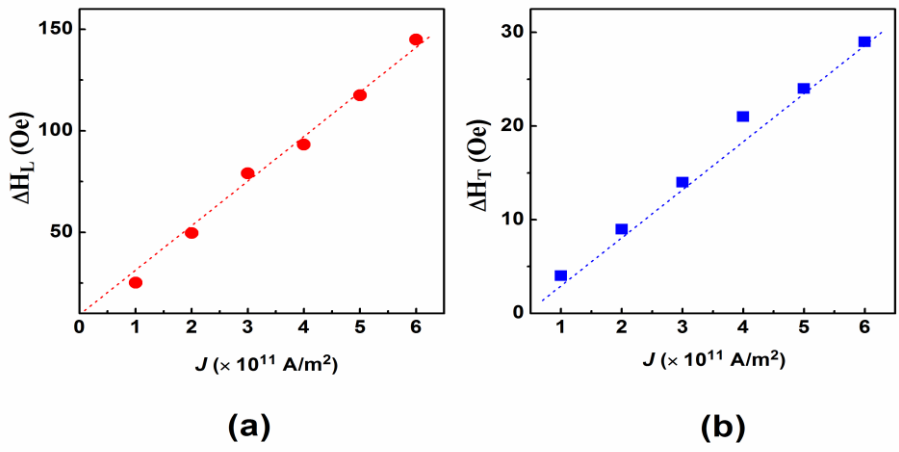

Fig. 4-17 (a) ΔH_L and (b) ΔH_T of the Ta(3)/Pd(3)/$(CoFe/Pd)_{15}$/Ta(3) samples, after planar Hall effect correction with different charge current density (J).

It is found that The magnitude of ΔH_L and ΔH_T increase linearly with J. We define the longitudinal (β_L) and transverse (β_T) SOT efficiencies [185, 188] as $\beta_{L(T)}$

$=\Delta H_{L(T)}/J$ and the $\beta_{L(T)}$ values can be obtained from the slope. The β_L (24 Oe $cm^2/10^7$ A) is around 5 times larger than the β_T (5 Oe $cm^2/10^7$ A), the damping-like torque arisen by the spin current from Ta layer should be the main source of the SOT in the CoFe/Pd multilayers [78]. In addition, these results indicate that although the thickness of top and bottom Ta layers is identical (3 nm), the top and bottom Ta layers generate non-identical SOTs on the CoFe/Pd multilayers. The effective spin Hall angle θ_{SH} is calculated from H_L using the formula [189] $H_L = \hbar\theta_{SH} J/(2eM_s t_F)$, with t_F is the ferromagnetic film thickness, e is the electron charge, and $\hbar$ is the Planck constant. The effective θ_{SH} = 0.02 is derived. Although the effective θ_{SH} in our CoFe/Pd multilayers is smaller than other reported Ta layer (θ_{SH} ~ 0.12) [78], the SOT generated by Ta layer also can promote the DW motion in the direction with electrons flow [75, 78]. Therefore, the combination of the SOT generated by Ta layer and the non-adiabatic STT torque is benefit to drive the DW motion and cause the enhancement of the spin-torque efficiency.

4.8 Summary

In summary, the $Co_{70}Fe_{30}$/Pd multilayers with strong perpendicular magnetic anisotropy and magnetic properties with variations of t_{CoFe}, t_{Pd} and repeated number n have been investigated. A small M_s value as low as 217 emu/cc and a maximum K_{eff} as large as 2.81×10^6 erg/cc are obtained when t_{CoFe} = 0.4 nm, t_{Pd} = 1.2 nm and n = 15. This high K_{eff} is beneficial to form narrow DW width, which can increase the capacity for data storage. By using XAS and XMCD measurements, spin polarization is

observed and estimated up to 60% in the thin CoFe/Pd multilayer films. Furthermore, the XAS and XMCD spectra reveal that the modification of electronic structure of CoFe/Pd interfacial magnetic moments by changing the Pd sublayer thickness contributes to the magnetic properties of the films. The motion of DWs manipulated by current with J_{th} = 1.4×10^{11} A/m^2 under H of 750 Oe has been observed in the CoFe/Pd multilayer nanowire at room temperature measurement. The depinning experiments show the spin-torque term works as an effective field with *J*, which indicates the non-adiabatic torque has the effect on the DW motion. In addition, a θ_{SH} = 0.02 is obtained in the CoFe/Pd multilayer nanowires show that the combination of the SOT and the non-adiabatic STT torque is the main contribution to the motion of the DW.

Chapter 5 Monatomic $(Co_{70}Fe_{30}/Pd)_n$ superlattice-like film and its application for DW motion

In chapter 4, we observe a threshold current density $J_{th} = 1.4\times10^{11}$ A/m^2 under H = 750 Oe and a maximum DW velocity v = 0.3 m/s with $J = 6.4\times10^{11}$ A/m^2 due to the high depinning field H_{dep} =755 Oe. However, these values of J_{th} and v are difficult to be used for commercial applications. In addition, the Pd-based multilayer suffers from PMA instability when the post-process temperature is above 300 ^{o}C due to Pd diffusion. It has been reported that the PMA of Co-based multilayers disappears when the post-annealing temperature (T_{pa}) is increased beyond 300 ℃ due to the intermixing of atoms at the interfaces of multilayers [190, 191]. This will suppress the stability of the nanowire device for long-time usage [192]. Therefore, the study of ultrathin films with large PMA, small H_{dep} and high temperature stability is important for the application of DW motion. In addition, the relatively high spin polarization (P ~ 60%), which is favorable to reduce the threshold current density for DW motion [34], is observed in CoFe/Pd multilayers. Moreover, the noble metal Pd used in the multilayers can improve the magnetic property of films because of longer spin-diffusion length compared with Pt [193, 194].

In this chapter, we show that a high PMA can be achieved in CoFe/Pd superlattice-like multilayers with total thickness as low as 1.5 nm using CoFe and Pd sublayers at monatomic layered thicknesses owing to the formation of an ordered superlattice-like structure [192, 195]. The superlattice-like structure can suppress the

interface intermixing and lead to small H_{dep} for DW motion. In addition, high temperature stability up to 350 ℃ is also demonstrated in these multilayers. The high thermal stability of superlattice-like structure films can enhance the stability of the device for long-time usage [192]. All these properties indicate that the ultrathin CoFe/Pd multilayer with alternative CoFe and Pd monatomic layers is a potential material for racetrack memory devices.

We have also investigated the current-induced DW motion under small magnetic field H and systematically studied the DW velocity dependence on H and current density in monoatomic (CoFe/Pd) multilayer nanowires to disclose the nature of DW motion. A small H_{dep} and low J_{th} are observed. The nonadiabatic spin transfer torque is proposed to be a dominant factor for the current-induced DW motion in ultrathin $[CoFe/Pd]_n$ multilayer.

5.1 Deposition conditions and magnetic characterization methods

The samples were grown on thermally oxidized Si (100) substrates using dc magnetron sputtering in an ultrahigh vacuum chamber with base pressure lower than 5.0×10^{-9} Torr at room temperature. All samples were deposited at a constant Ar pressure of 1.5 mTorr. Two series of experiments were conducted by alternating the thickness of CoFe monolayer (t_{CoFe}) and Pd monolayer (t_{Pd}) and then the number of $(Co_{70}Fe_{30}/Pd)_n$ bilayers (n) in due succession. The first set of experiment was designed to investigate the effects of the respective monolayer thickness on PMA.

The t_{CoFe} was varied from 0.12 to 0.26 nm and t_{Pd} was varied from 0.16 to 0.28 nm. The second set of experiment was carried out to examine the effects of the repeat number of bilayer on PMA. The stack structure was $Si/SiO_2/Ta(3)/Pd(3)/[CoFe(0.16)/Pd(0.22)]_n/Ta(3)$, where n is ranged from 3 to 30. All the number in bracket is the thickness of the layer with unit in nanometer. The thickness of CoFe and Pd monatomic layers were fixed at 0.16 nm and 0.22 nm, respectively. These thickness values were derived from the interplanar spacing of (111) plane of bulk $Co_{70}Fe_{30}$ and Pd crystal [196, 197]. For comparison, a series of $Co_{70}Fe_{30}$-Pd alloy samples with quantities of CoFe and Pd and the total thickness equivalent to that in the $(CoFe/Pd)_n$ multilayers were prepared by co-sputtering CoFe and Pd targets. The Ta(3)/Pd(3) was applied as a seed layer and Ta(3) was used as a capping layer to avoid oxidation [198]. The effective anisotropy (K_{eff}) was obtained by integrating the area involved between the M-H loops measured in both directions. The K_{eff} is determined [199] as

$$K_{eff} = H_k M_s/2 = K_u - 2\pi M_s^2 \quad (5.1)$$

where H_k is the anisotropy field which the hard axis and easy axis M-H loops superposed, K_u is the intrinsic anisotropy and the term $2\pi M_s^2$ is the demagnetization energy density. The K_{eff} can also be written [200] as

$$K_{eff} = \frac{K_i}{t} - 2\pi M_s^2 + K_v \quad (5.2)$$

where t is the total thickness of CoFe layer, K_i and K_v denote the interfacial and volume anisotropy energy densities, respectively. Generally, the $K_{eff}t$ is linearly dependent on t. The value of K_i can be derived from the intercept of the y axis. The

crystal structures of $(Co_{70}Fe_{30}/Pd)_n$ multilayers and $Co_{70}Fe_{30}$-Pd alloy films were characterized by TEM and XRD. The surface morphology was measured using AFM.

The nanowire with a pattern of 40 μm-long and 300 nm-wide was fabricated on the monoatomic (CoFe/Pd) multilayer films by electron beam lithography and Ar ion-milling. The nanowire structure was then modified with a triangular contact pad and one Hall cross with a width of 300 nm for magnetotransport measurements. The Au electrodes with thickness of 40 nm were deposited on the contact pad and then wired to inject the driving current into the nanowire. The DW motion in the nanowire was detected by means of anomalous Hall effect (AHE) and all measurements were performed at room temperature as mentioned in the previous chapter.

5.2 Characterization of monatomic $(Co_{70}Fe_{30}/Pd)_n$ superlattice-like film

5.2.1 Magnetic properties of ultrathin $(CoFe/Pd)_n$ multilayers dependent on the thickness of CoFe and Pd sublayers

Figure 5-1 (a) shows the magnetic hysteresis loops of co-sputtered CoFe-Pd alloy film with composition and thickness equivalent to that in the [CoFe (0.16 nm)/Pd (0.22 nm)]$_{10}$ multilayer in the as-deposited state. It is clearly observed that the in-plane loop has an easy-axis behavior whereas the out-of-plane loop displays a hard-axis behavior. Figure 5-1 (b) depicts the magnetization hysteresis (M-H) loops for the [CoFe (0.16)/Pd (0.22)]$_{10}$ multilayer with well-developed PMA property in the as-deposited state. Figure 5-2 shows the enlarged portion of the loops measured under

magnetic field (H) applied along the in-plane and out-of-plane directions. The in-plane M-H loop exhibits nearly linear variation of M with H below the saturation field. The loops measured with out-of-plane field show sharp magnetization reversal behavior and squareness with a remanence M_r nearly equals to M_s, indicating the easy axis is perpendicular to the plane.

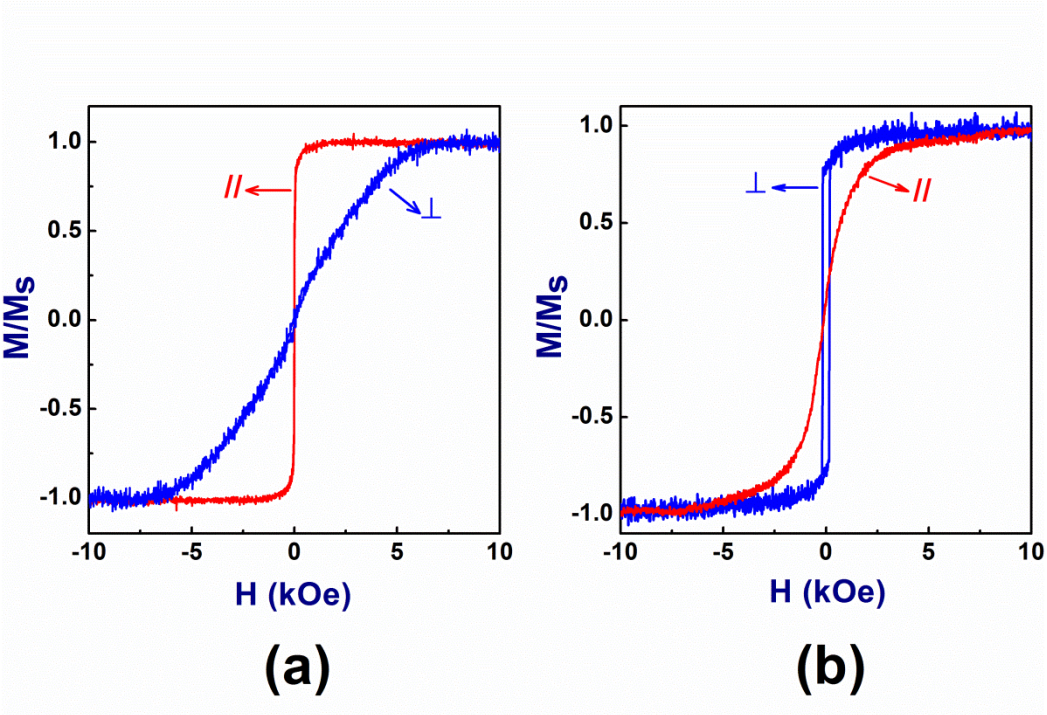

Fig. 5-1 Magnetic hysteresis (M–H) loops of (a) co-sputtered CoFe-Pd alloy films with the equivalent composition as [CoFe (0.16 nm)/Pd (0.22 nm)]$_{10}$ multilayer and (b) [(CoFe (0.16 nm)/Pd (0.22 nm)]$_{10}$ multilayers. The symbol // and ⊥ indicates the loops measured with magnetic field (*H*) in the plane of sample film and out of plane of the sample film, respectively.

To examine the temperature stability, the M–H loops of [(CoFe(0.16)/Pd (0.22)]$_{10}$ multilayers annealed at 350 ℃ for 1 hour are also shown in Fig. 5-2. It is found that the PMA remained unchanged after post-annealing temperature (T_{pa}) up to 350 ℃. This result is in contrast to the previous report of [CoFe/Pd] based multilayer, where the PMA of CoFe/Pd multilayers with thicker Pd sublayer (>1 nm) degraded when T_{pa} >300 ℃ due to Pd diffusion [201]. We infer that the interface diffusion is

suppressed and the post-annealing stability of our ultrathin $[(CoFe(0.16)/Pd\ (0.22)]_{10}$ film is attributed to the formation of an ordered superlattice-like structure [192, 202]. The ultrathin multilayer film can be considered to be an artificial superlattice-like structure since the thicknesses of the CoFe and Pd layers are monatomic.

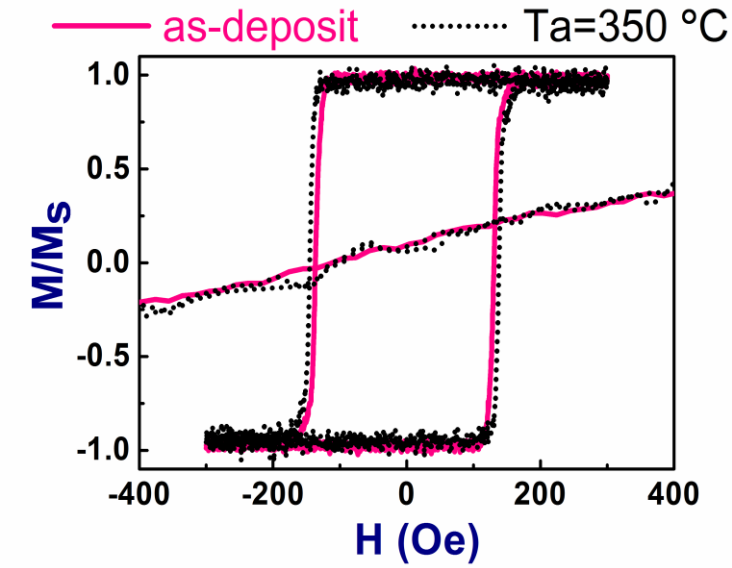

Fig. 5-2 The enlarged M–H loops of $[(CoFe\ (0.16\ nm)/Pd\ (0.22\ nm)]_{10}$ multilayers in the as-deposited state (solid lines) and annealed at 350 ℃ for 1 hour (dotted lines) at small fields.

The microstructure of the ultrathin $[CoFe\ (0.16)/Pd\ (0.22)]_{10}$ films with high PMA were further studied by TEM to investigate the ordered superlattice-like structure. Figure 5-3 (a) and (b) reveal the cross sectional images with selective area electron diffraction (SAED) of $[CoFe(0.16)/Pd\ (0.22)]_{10}$ film and co-sputtered CoFe-Pd alloy film with equivalent composition as CoFe/Pd multilayer deposited on the Ta/Pd seed layers, respectively. The d-spacing of Pd (111) obtained is ~0.223 nm for both of the Pd seed layers in two different cases. This means that the Pd seed layers have the same fcc (111) structure for both of the cases. For CoFe/Pd multilayer sample, fcc phases were formed in both ultrathin CoFe/Pd multilayer and Pd seed layer. The ultrathin film was deposited epitaxially on the Pd (111) seed layer,

resulting in a high-quality crystal structure, thus contributing to the strong PMA [21]. The d-spacing of Pd (111) obtained is ~0.223 nm, which is consistent with the result measured by XRD (to be discussed later). On the other hand, stacking faults were observed in the fcc phase of the CoFe-Pd alloy film. The poor crystallity would lead to a reduced K_{eff} and cause the formation of an in-plane easy axis in the CoFe-Pd alloy films [203]. It is difficult to observe the exact superlattice-like microstructure of ultrathin CoFe/Pd multilayers using TEM due to the limit of resolution. However, the PMA can be maintained with the post-annealing temperature up to 350 ℃ and maximum K_{eff} are achieved when thickness of CoFe (0.16 nm) and Pd (0.22 nm) sublayers are monatomic from the AGFM result indirect an ordered structure may exist in the CoFe/Pd multilayers with alternative Pd and CoFe monatomic layers, which will be discussed detailly in the following part.

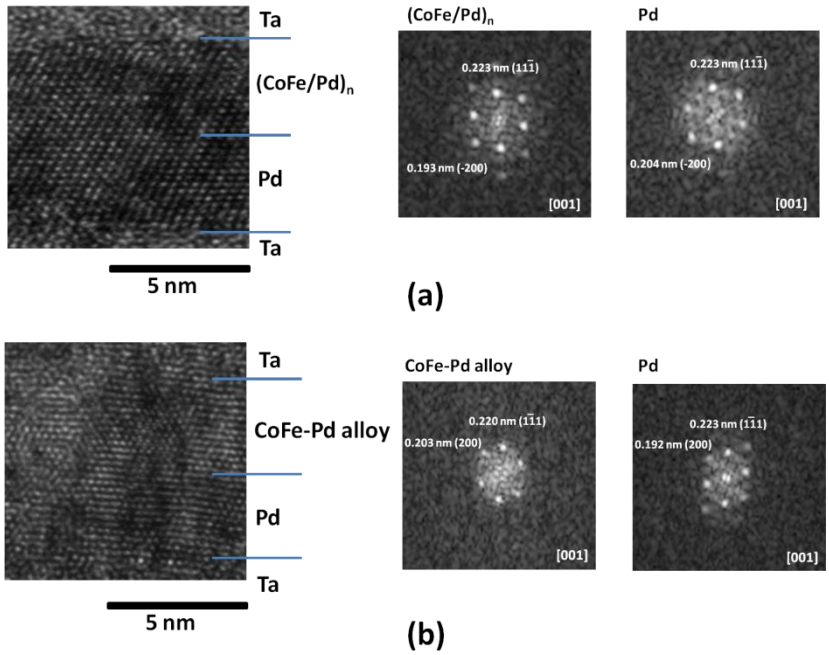

Fig. 5-3 The cross-sectional TEM images with selective area electron diffraction (SAED) of (a) Ta(3 nm)/Pd(3 nm)/[CoFe (0.16nm)/Pd (0.22nm)]$_{10}$/Ta(3 nm) multilayer sample and (b)Ta(3 nm)/Pd(3 nm)/equivalent composition of co-sputtered CoFe-Pd alloy /Ta(3 nm) film sample.

To further clarify the contribution of superlattice-like structure to the enhancement of PMA, K_{eff} and M_s of CoFe/Pd multilayers in the as-deposited state with different thickness of Pd and CoFe sublayers as well as different repeated number n were measured. Firstly, the number of CoFe/Pd multilayers was fixed at n = 10, while the thickness of respective CoFe sublayers and Pd sublayers were varied to investigate the variation of PMA among these fabricated multilayer samples.

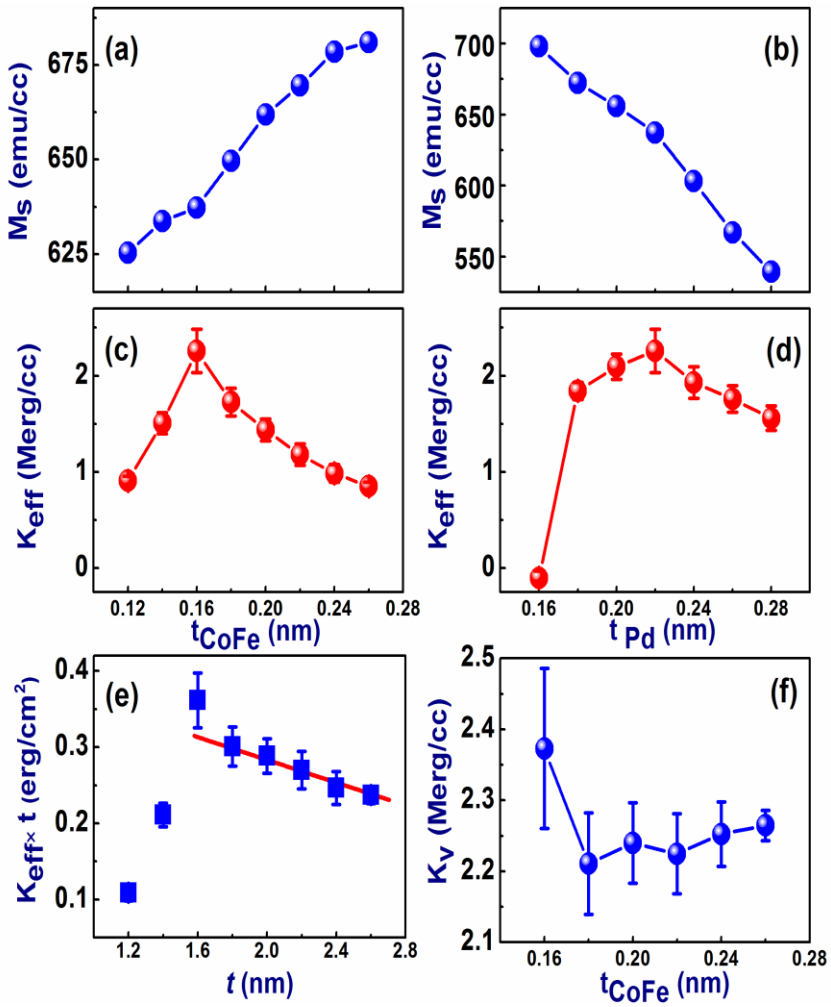

Fig. 5-4 M_s (a) and K_{eff} (c) in [CoFe (t_{CoFe})/Pd (0.22 nm)]$_{10}$ multilayer samples as a function of the thickness of CoFe monolayer (t_{CoFe}) ranging from 0.12 nm to 0.26 nm, respectively. The M_s (b) and K_{eff}(d) in [CoFe (0.16 nm)/Pd (t_{Pd})]$_{10}$ multilayer samples as a function of the thickness of Pd monolayer (t_{Pd}) ranging from 0.16 to 0.28 nm. (e) The K_{eff} t_{CoFe} in [CoFe (t_{CoFe})/Pd (0.22 nm)]$_{10}$ multilayer samples as a function of the total thickness of CoFe (t). (f) K_v in [CoFe (t_{CoFe})/Pd (0.22 nm)]$_{10}$ multilayer samples as a function of the thickness of CoFe monolayer (t_{CoFe}) ranging from 0.16 nm to 0.26 nm.

Figure 5-4 (a) and (c) show the variation of M_s and K_{eff} in the $[(CoFe(t_{CoFe})/Pd(0.22)]_{10}$ multilayers with t_{CoFe} while Fig. 5-4 (b) and (d) depict the variation of M_s and K_{eff} in $[(CoFe(0.16)/Pd(t_{Pd})]_{10}$ multilayers with t_{Pd}. The M_s value of $[(CoFe(t_{CoFe})/Pd(0.22)]_{10}$ multilayers increases by ~ 10% as t_{CoFe} increases from 0.12 to 0.22 nm, whereas M_s value of $[(CoFe(0.16)/Pd(t_{Pd})]_{10}$ multilayers decreases by ~ 30% as t_{Pd} increases from 0.16 to 0.28 nm. The remarkable increase in M_s with increasing t_{CoFe} can be ascribed to the contribution of magnetic moment of CoFe, whilst the reduced M_s with increasing t_{Pd} was caused by the expanded total volume of the multilayers due to a larger amount of Pd layers. In both sets of multilayer samples, K_{eff} increases with increasing t_{CoFe} (or t_{Pd}) to a maximum value and then decreases with increasing t_{CoFe} (or t_{Pd}) as shown in Fig. 5-4 (c) and (d). The maximum value of K_{eff} (2.26×10^6 erg/cc) is achieved at t_{CoFe} = 0.16 nm and t_{Pd} = 0.22 nm, which corresponds to the interplanar spacing of $Co_{70}Fe_{30}$ (111) and Pd (111) planes in the bulk samples, respectively. The variation of K_{eff} with t_{CoFe} (or t_{Pd}) suggests that the highest PMA could be obtained when layer by layer stacking of CoFe and Pd was conducted such that each sublayer is exactly monatomic. This result could be explained based on the formation of the superlattice-like structure as shown in Fig. 5-5 (a).

In Fig. 5-4 (d), a negative value of K_{eff} is observed when t_{Pd} is reduced to 0.16 nm, indicating an in-plane magnetic anisotropy (IMA) instead of the PMA because of the interfacial and crystalline anisotropy are not strong enough to overcome the demagnetizing anisotropy. Figure 5-5 (b) shows that when the thickness of CoFe is

larger than one monolayer, the redundant CoFe (Pd) adatoms will damage the interface structure between the CoFe and Pd sublayer, leading to the reduced PMA and K_{eff} . On the other hand, the reason for the decrease of K_{eff} with reducing t_{CoFe} in the region of $t_{CoFe} < 0.16$ nm and t_{Pd} in the region of $t_{Pd} < 0.22$nm can be explained as follows. When the CoFe (Pd) thickness is less than one monolayer, the bonded CoFe (Pd) adatoms are randomly distributed and formed isolated CoFe (Pd) spots in the film as shown in Fig. 5-5 (c). Between these spots, the CoFe (Pd) upper layer will grow directly onto the CoFe (Pd) bottom layer, which would disrupt the formation of CoFe/Pd interface and cause the reduction of PMA.

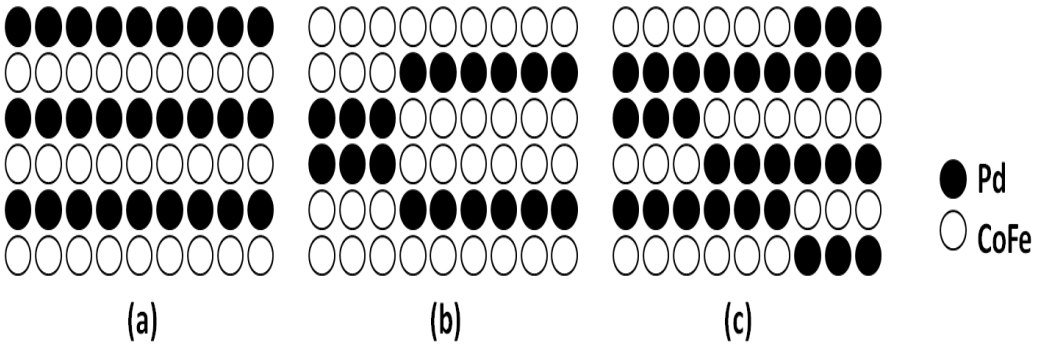

Fig. 5-5 The schematic diagram model showing the structure of the ultrathin multilayers with Pd sublayer thickness is monoatomic and CoFe sublayer thickness is (a) equal to monoatomic (b) larger than monoatomic and (c) less than monoatomic.

Figure 5-6 (a) and (b) show the K_{eff} in the $[(CoFe(t_{CoFe})/Pd(t_{Pd})]_{10}$ multilayers as functions of post-annealing temperature T_{pa} and as-deposited state for t_{CoFe} and t_{Pd} at various thicknesses, respectively. We find that for all the samples except the multilayers with CoFe and Pd sublayer thickness being monoatomic, the K_{eff} slightly increases as the T_{pa} increases from 200 ℃ to 300 ℃. Then K_{eff} start to reduce when the T_{pa} is increased up to 350 ℃ and after 400 ℃, PMA almost completely disappear. The improved PMA with T_{pa} up to 300 ℃ can be attributed to the enhanced fcc (111)

texture upon thermal annealing with T_{pa} > 350 ℃. It would cause excessive interfacial diffusion and destroy the PMA [204]. However, for multilayers with CoFe and Pd sublayer thickness is monoatomic, the K_{eff} remains almost constant for $T_{pa} \leq 350$ ℃ and starts to decrease after 370 ℃. This result confirms the ordered superlattice-like structure can suppress the interface diffusion and improve the texture stability with increasing T_{pa}.

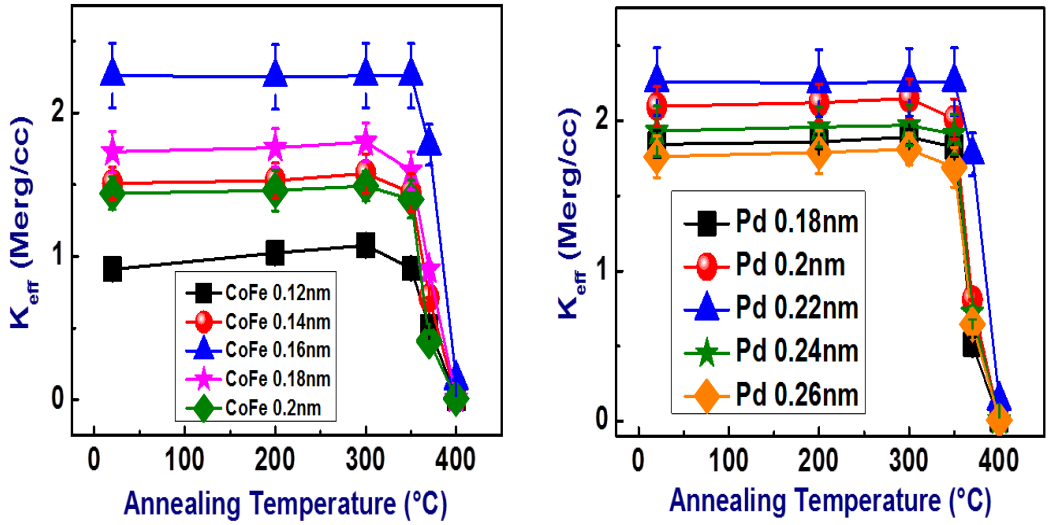

Fig. 5-6 K_{eff} as a function of the annealing temperature and the as-deposited state for (a) $[CoFe(t_{CoFe})/Pd(0.22\ nm)]_{10}$ multilayer samples with various t_{CoFe} and (b) $[CoFe(0.16\ nm)/Pd(t_{Pd})]_{10}$ multilayer samples with various t_{Pd}.

It would be interesting to evaluate the contribution of the interfacial and volume anisotropy using the obtained value of K_{eff}. In this study, it is found that the linear relationship can only be obtained with t_{CoFe} beyond one monolayer thickness as shown in Fig. 5-4 (e). The K_i is obtained to be 0.40 erg/cm^2, which is consistent with the value reported in Ref [205]. Figure 5-4 (f) shows the variation of K_v in the $[(CoFe(t_{CoFe})/Pd(0.22\ nm)]_{10}$ multilayers with t_{CoFe} calculated using the Eq. (5.2). We notice that K_v reached a maximum at t_{CoFe} = 0.16 nm, which is much larger than other

K_v with t_{CoFe} ranging from 0.18 to 0.26 nm. The highest K_{eff} observed when the thickness of CoFe and Pd is equal to monolayer thickness. This result is in contrast to the previous first-principles calculation result [206], in which PMA had a maxima when the $t_{Co(Fe)}$:t_{Pd} = 1:2 and PMA did not show any maxima at the ratio of 1:1. The difference between the experimental and calculation results can be attributed to the formation of a superlattice-like CoFe/Pd structure with monolayer thickness, which can enhance the PMA.

The superlattice-like structure may induce another magneto-crystalline anisotropy (K_c) contained in the K_v and promote K_v value to K_{eff} [207]. The K_c is estimated to be 1.41×10^5 erg/cc according to the Fig. 5-4 (f). The positive value of K_c indicates its influence on the enhancement of the PMA. This result confirms that the improvement in PMA is closely related to the formation of superlattice-like microstructure with monatomic CoFe and Pd sublayers, which agrees well with the report by S. Fukami *et al* [207]. In addition, by comparing with the previous thick CoFe/Pd multilayers (t_{Pd}>1nm) [46], a larger K_{eff} (2.26×10^6 erg/cc) and a smaller total thickness of CoFe/Pd multilayer (~ 3.8 nm) as well as the post-annealing stability up to 350 ℃ in the superlattice-like CoFe/Pd multilayers suggest that the ultrathin CoFe/Pd multilayer is a promising candidate to be used as the reference layer in the MTJs.

5.2.2 Magnetic properties of ultrathin $(CoFe/Pd)_n$ multilayers dependent on the repeated number *n*

The $[CoFe\ (0.16\ nm)/Pd\ (0.22\ nm)]_n$ multilayers with *n* ranging from 3 to 30 were deposited to study the effect of *n* on PMA. It is found that PMA is well established in $[CoFe\ (0.16\ nm)/Pd\ (0.22\ nm)]_n$ multilayers films with *n* as small as 4, which corresponds to a total thickness of 1.5 nm for the whole multilayers. Heretofore, this ultrathin CoFe/Pd multilayers with PMA has not been reported for the CoFe based multilayers, in which the PMA can only be observed with the total thickness larger than 5 nm [208]. The disappearance of PMA in CoFe/Pd multilayers with $n < 4$ is probably attributed to reduced number of interfaces and the formation of magnetic dead layers at the multilayer interfaces with the Pd seed layer and the Ta cap layer. This reduces the effective thickness of the CoFe/Pd multilayers [209]. Figure 5-7 (a) and (b) show M_s and K_{eff} of $[CoFe\ (0.16\ nm)/Pd\ (0.22\ nm)]_n$ multilayers as a function of *n*. It is noted that both M_s and K_{eff} gradually increase to their respective maximum values of 640 emu/cc and 2.33×10^6 erg/cc as *n* increases from 5 to 9 and decrease with further increasing *n*.

We further investigate the effect of *n* on PMA characteristics (M_s and K_{eff}) by performing AFM and XRD measurements. The dependence of surface roughness of ultrathin $[CoFe(0.16\ nm)/Pd(0.22\ nm)]_n$ multilayers as a function of *n* is shown in Fig. 5-7 (c). It is found that the root mean square (*RMS*) roughness remains unchanged as *n* increases from 6 to 10, and then monotonously increases from 0.240 to 0.295 nm when *n* further increases to 35. Since the grown CoFe and Pd monolayer thickness are

rather thin, the bonded adatoms from the target atoms impinging on the substrate surface are prone to form nuclei and thus lead to island growth during the deposition process. This may result in the damage of the flatness of the interface between CoFe and Pd monolayers and cause the increase in roughness. As *n* increases, the randomly distributed adatoms will accumulate and the roughness will be enhanced, resulting in a relaxation state and the destruction of the superlattice-like structure of the multilayers. The random nature of such fluctuations induced roughness is expected to lower the strength of PMA [210]. In addition, as the roughness increases, the fluctuating interface between CoFe and Pd atoms would induce the augment of in-plane magnetization components, which would effectively reduce K_{eff}.

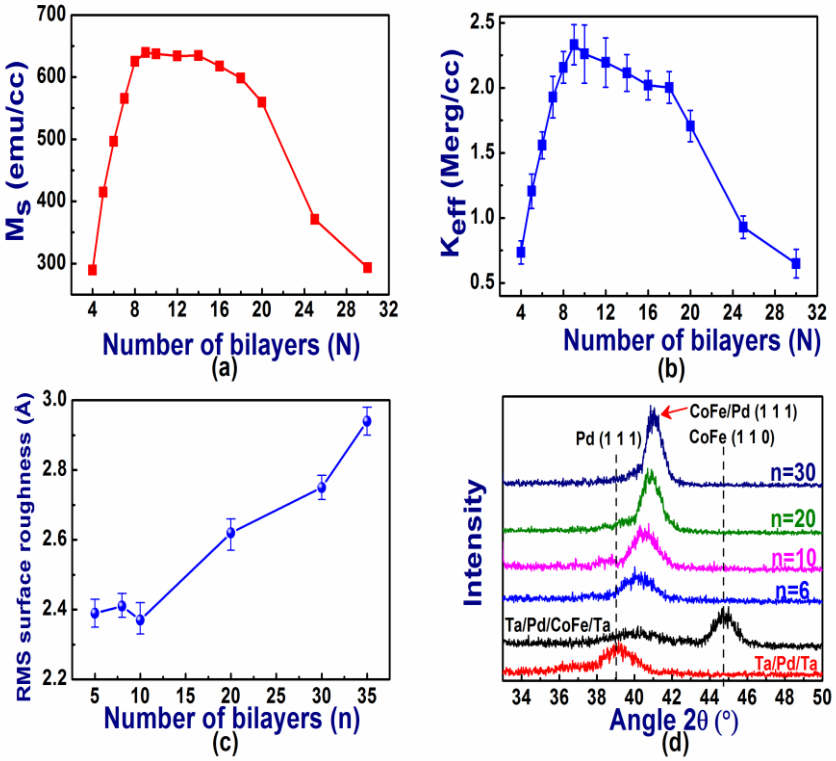

Fig. 5-7 M_s (a) and K_{eff} (b) of [CoFe (0.16 nm)/Pd (0.22 nm)]n multilayers as a function of n. (c) The surface roughness of ultrathin [CoFe (0.16 nm)/Pd (0.22 nm)]n multilayers as a function of n. (d) XRD of referenced Ta(3 nm)/Pd(3 nm)/Ta(3 nm), Ta(3 nm)/Pd(3 nm)/CoFe(8 nm)/Ta(3 nm)layers and ultrathin multilayers [CoFe (0.16 nm)/Pd (0.22 nm)]$_n$ as a function of n.

Figure 5-7 (d) reveals the XRD spectra for CoFe (0.16 nm)/Pd (0.22 nm) multilayers with n = 6, 10, 20, 30 and for reference samples with the following structures: Ta(3 nm)/Pd(3 nm)/Ta(3 nm) and Ta(3 nm)/Pd(3 nm)/CoFe(8 nm)/Ta(3 nm). It has been observed that the CoFe/Pd multilayer samples have primary fcc (111) texture which is well known as an important factor to induce the PMA in the ultrathin CoFe/Pd multilayers [46]. Another important feature shown in the $(CoFe/Pd)_n$ multilayer films is the shift of the CoFe/Pd (111) diffraction peak to higher 2θ angle with increasing n. In addition, the $Co_{100-x}Fe_x$ films deposited on Ta/Pd seed layer with Fe concentration above 22% exhibited body-centered cubic (bcc) (110) structure [211]. A CoFe (110) peak can be observed in the Ta(3 nm)/Pd(3 nm)/CoFe(8 nm)/Ta(3 nm) reference sample as shown in Fig. 5-7 (d). The CoFe/Pd (111) diffraction peak also shifts towards higher angle with increasing n. The shift in CoFe/Pd (111) peak with change in n is due to the lattice contraction normal to the $(CoFe/Pd)_n$ multilayer film plane increases with n [212]. This leads to the lattice spacing of the (111) plane of the CoFe/Pd multilayers ($d_{CoFe/Pd\ (111)}$) to decrease with n and thus causes the shift of CoFe/Pd (111) diffraction peak to higher 2θ angle. The increase in M_s and K_{eff} for n ranging from 4 to 9 can be ascribed to the increase in the number of interfaces and thus promote the superlattice-like structure. The maximum values for both M_s and K_{eff} of CoFe/Pd multilayers were obtained at n = 9. The subsequent decrease in M_s and K_{eff} at larger values of n originates from the deterioration of the flatness of interface and loss of the superlattice-like structure.

5.3 Current induced domain wall motion in the ultrathin $(Co_{70}Fe_{30}/Pd)_n$ -based nanowire

5.3.1 Depinning field of the ultrathin $(CoFe/Pd)_n$-based nanowire

Figure 5-8 shows the normalized Hall resistance hysteresis loops (R_H-H) of the ultrathin $(CoFe/Pd)_8$ multilayer nanowire with a width of 300 nm under a sweeping magnetic field (between -1000 Oe and 1000 Oe) perpendicular to the film plane (solid line with solid square symbol), which is similar to Fig. 4-11 shown in chapter 4. The stack structure was $Si/SiO_2/Ta(3)/Pd(3)/[CoFe(0.16)/Pd(0.22)]_8/Ta(3)$. The number in bracket is the thickness of the layer with unit in nanometer. We have measured the field-switching experiment 10 times for both positive and negative directions of magnetic field and the depinning field H_{dep} of 120 $\pm$ 0.6 Oe is derived and fixed for both directions in the 300 nm-width nanowires patterned on the ultrathin CoFe/Pd multilayers with alternative CoFe and Pd monatomic sublayers.

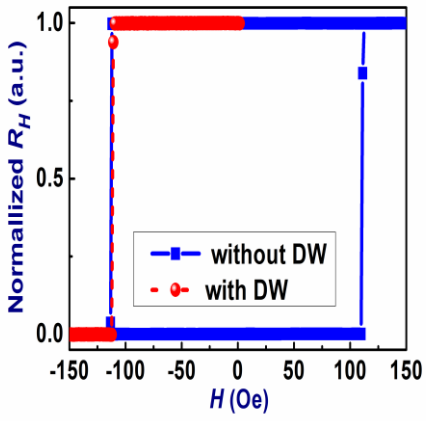

Fig. 5-8 Normalized Hall resistance hysteresis loops (R_H-H) of ultrathin $(CoFe/Pd)_8$ multilayer nanowire with a width of 300 nm under a sweeping magnetic field perpendicular to the film plane without the driving pulse current (solid line with solid square symbol); The variation of R_{Hall} under the magnetic field H sweeping from 0 to -200 Oe for the nanowire after DW injection process (dashed line with solid cycle symbol).

In order to further understand the small H_{dep} in the ultrathin CoFe/Pd multilayer, we have measured the H_{dep} in two sets of 300 nm-width nanowire samples. The stack structure of first set samples was Ta(3)/Pd(3)/[CoFe(t_{CoFe})/Pd(0.22)]$_8$/Ta(3) with t_{CoFe} ranging from 0.1 to 0.22 nm. The second set samples was Ta(3)/Pd(3)/ [CoFe(0.16)/Pd(t_{Pd})]$_8$/Ta(3) with t_{Pd} ranging from 0.16 to 0.28 nm. Figure 5-9 (a) and (b) show the variation of H_{dep} in the [(CoFe(t_{CoFe})/Pd(0.22 nm)]$_8$ multilayer nanowires with t_{CoFe} and [CoFe(0.16)/Pd(t_{Pd})]$_8$ multilayer nanowires with t_{Pd}, respectively. It is found that in both sets of multilayer nanowires, H_{dep} decreases with increasing t_{CoFe} (or t_{Pd}) to a maximum value and then increases with increasing t_{CoFe} (or t_{Pd}). The minimum value of H_{dep} (120 ± 0.6 Oe) is achieved at t_{CoFe} = 0.16 nm and t_{Pd} = 0.22 nm, which corresponds to one monoatomic layer thickness of CoFe and Pd, respectively. This result indicates that the ultrathin CoFe/Pd multilayer with one monoatomic sublayer thickness of CoFe and Pd possesses a smaller DW pinning strength, which may be attributed to a better ordering of ultrathin CoFe/Pd multilayers with alternate monoatomic layer deposition (AMLD). The ultrathin CoFe/Pd multilayers exhibit a maximum effective magnetic anisotropy when the thickness of CoFe and Pd sublayers are around one monoatomic layer thickness of CoFe and Pd, respectively. This is due to the formation of superlattice-like structure in the ultrathin CoFe/Pd multilayers with AMLD [192, 195]. The superlattice-like structure with better ordering can reduce the number of pinning sites and suppress the intermixing between CoFe and Pd sublayers.

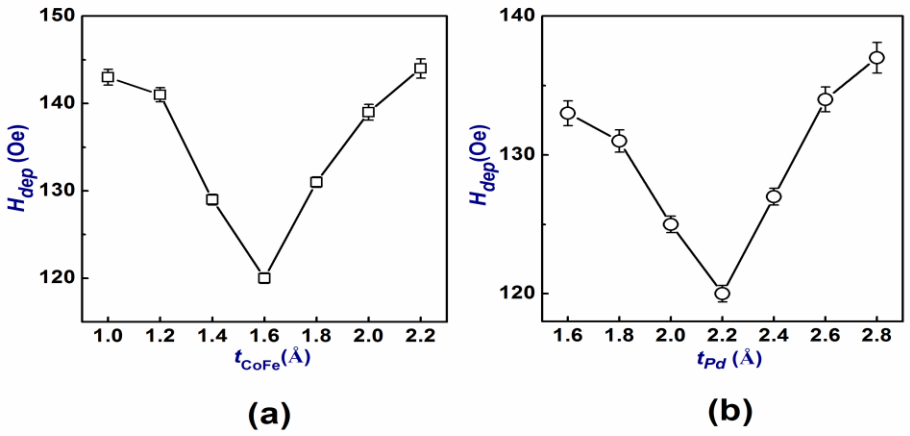

Fig. 5-9 (a) The H_{dep} in $[(CoFe(t_{CoFe})/Pd(0.22\ nm)]_8$ multilayer nanowires as a function of the thickness of CoFe sublayer (t_{CoFe}) ranging from 0.1 to 0.22 nm; (b) The H_{dep} in $[(CoFe(0.16\ nm)/Pd(t_{Pd})]_8$ multilayer nanowires as a function of the thickness of Pd sublayer (t_{Pd}) ranging from 0.16 to 0.28 nm.

5.3.2 The dependence of domain wall velocity on the magnetic field and threshold current density

In order to study the impact of the spin polarized current on the DW motion after DW injection, the R_{Hall} as a function of number of driving current pulses under fixed bias magnetic field ($H < H_{dep}$) are monitored as mentioned in chapter 4. Figure 5-10 shows the dependence of the averaged DW velocity (v) on driving current density (J) measured under different H from 75 to 115 Oe at 5 Oe intervals. It is known that a narrow DW can be formed in the nanowire because of high PMA of CoFe/Pd multilayers [184]. However, the narrow DW can be readily pinned due to the structure inhomogeneities. The pinning effect of structure defects on the narrow DW would cause a creep DW motion in the region of $H < H_{dep}$ [213]. As H is further increased beyond H_{dep}, the DW moves in a viscous flow region where the disorder becomes

irrelevant and can be ignored [131]. The current-driven DW motion in the creep region can be described by the following expression [34, 124] :

$$v = v_0 \exp\left[-\left(\frac{U_0}{k_B T_d}\right)\left(\frac{H_{dep}-H_J}{H}\right)^{\frac{1}{4}}\right] \quad (5.3)$$

where v is the DW velocity, v_0 is a velocity prefactor, U_0 is the scaling energy constant, k_B is the Boltzmann constant, T_d is the device temperature and H_J is the effective field from the spin transfer effect. The modified expression is valid in the limit $H_J < H_{dep}$. The linear dependence of $\ln(v)$ on $H^{-1/4}$ for all the different J as shown in Fig. 5-10 indicates that the DW motion is in the creep region.

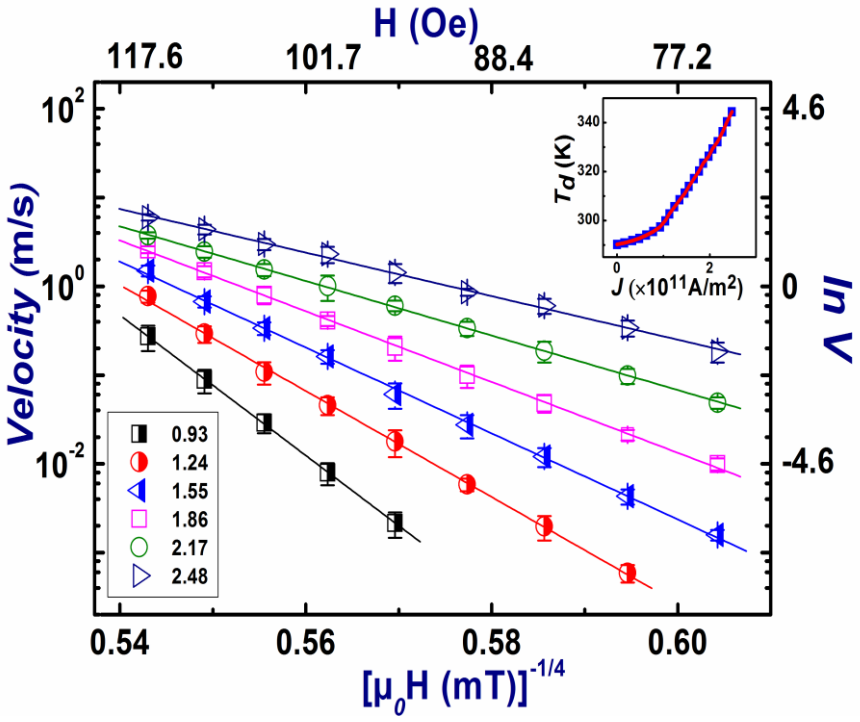

Fig. 5-10 The averaged DW velocity as a function of H for various driving current densities ranging from 0.93×10^{11} A/m^2 to 2.48×10^{11} A/m^2. Each data point is the average value of 10 measurements at each current density and magnetic field. The error bars denote the standard deviation of the mean value. The right vertical axis represents the logarithmic value of the DW velocity. The inset shows the dependence of the device temperature T_d on the pulsed current density *J*.

It is well known that the Joule heating also affects the DW motion besides the spin torque effect. The Joule heating would cause the variation of the device temperature (T_d) when the applied pulse current passing through the nanowire. Therefore, the enhancement of DW velocity with increasing *J* is mainly determined by two major factors, namely H_J due to spin torque effect and T_d caused by the Joule heating. The absolute value of k_v can be obtained from the slope (k_v) of $\ln(v)$ versus $H^{-1/4}$ as $k_v = \left(\frac{U_0}{k_B T_d}\right)(H_{dep} - H_J)^{\frac{1}{4}}$ in Fig. 5-10. Therefore, in order to extract the value of H_J resulted from the spin torque effect unambiguously, we have to determine T_d caused by the Joule heating separately. We have measured the variation of resistance in the nanowire as a function of pulsed current density and then converted the resistance into device temperature using the temperature coefficient of resistance (α_T) [214]. The value of $\alpha_T \sim 0.0045\ K^{-1}$ is derived from the resistance versus temperature measurement. The dependence of T_d on *J* is plotted in the inset of Fig. 5-10. The T_d increases nearly by 50 K above the ambient temperature as *J* increases from 0 to 2.48×10^{11} A/m^2. In addition, H_{dep} = 120 Oe and U_0 = 0.15 ± 0.01 eV are obtained from the DW velocity at H =120 Oe and *J* = 0 in Eq. (5.3). Hence, we can quantitatively derive H_J as a function of *J* as shown in Fig. 5-11 (a). It is seen that H_J increases almost linearly with *J* from 0.93×10^{11} to 2.48×10^{11} A/m^2. The spin-torque efficiency of ε = （1.68 ± 0.09)$\times10^{-14}$ T • m^2/A is obtained by a linear-fit of the data to $H_J = \varepsilon \cdot J$ according to Ref. [131].

It is found that there is no Hall resistance switching can be observed for a further reduction of bias field under centain current density, such as decreasing H to 90 Oe

for $J = 0.93\times10^{11}$ A/m^2. This suggests that the DW would not move towards the Hall cross because the effective field generated by both applied pulse current and H are not high enough to depin the DW. We therefore define threshold current density (J_{th}) as the lowest value of the spin current density to be sufficient enough to depin the DW from the pinning site and drive the DW to move along the nanowire [184]. The values of J_{th} are measured from the depinning experiment under different H. Figure 5-11 (b) shows the variation of J_{th} as a function of H. It is found that the J_{th} decreases linearly with H indicating the spin polarized current produces a field-like effect to assist DW depinning.

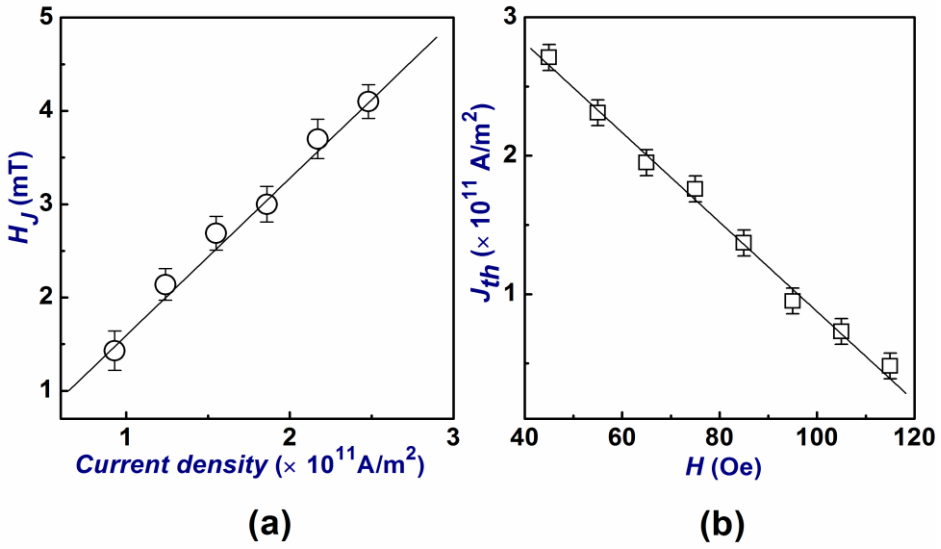

Fig. 5-11 (a) H_J as a function of pulsed current density J; (b) J_{th} as a function of magnetic field H.

5.3.3 Non-adiabatic torque and spin orbit torque of the ultrathin $(CoFe/Pd)_n$-based nanowire

The spin-transfer torque exerted on the DW is mainly attributed to two terms, i.e. the adiabatic torque [60] and the nonadiabatic torque [59, 62], which are strongly

dependent on the material, geometry and magnetic anisotropy (IMA or PMA). The adiabatic term is expected to be the main contribution to the DW motion in the Co/Ni multilayers [42] or CoFeB single layer [146] wire. In contrast, the non-adiabatic torque with a high non-adiabaticity factor β dominates the DW motion rather than the adiabatic term in Co/Pt [124], (Ga, Mn)As [215] and Pt/Co/AlO_x [93] PMA films. In PMA films with the adiabatic term being dominant in DW motion, J_{th} is only determined by the intrinsic pinning [42, 146]. This means that J_{th} is independent of the external magnetic field in films which are adiabatic-term dominated. On the other hand, the non-adiabatic term is usually characterized as an additional effective field associated with the DW motion. Thus J_{th} relies on H in the PMA films with non-adiabatic term governing the DW motion [34, 150].

From the microscopic point of view, the contribution of adiabatic and nonadiabatic terms depends on the DW characteristic width of a given material. When DW width is wide, the electron spin can adiabatically follow the local spin direction as the electrons transverse the DW. As DW width is narrow, the spatial magnetization gradient across the DW will become very large. This causes the formation of a finite mis-tracking angle between the electron spin and local spins and result in spin-flip scattering of the electrons and a nonadiabatic torque acted on the DW [63]. Therefore, it is expected that the non-adiabatic torque plays a dominant role in the narrow DWs due to higher magnetization gradient [184].

We estimated a narrow DW width ($\lambda \sim 4.8$ nm) in our nanowire using $\lambda = \sqrt{A_{ex}/K_{eff}}$, where the effective perpendicular magnetic anisotropy $K_{eff} = 4.3 \times 10^5$

J/m^3 and the exchange constant A_{ex} is assumed to be 1×10^{-11} J/m for CoFe/Pd multilayer thin films [46]. The value of λ in our nanowire is much smaller than those in in-plane magnetized films [216]. Therefore, the narrow λ and proportional variation of J_{th} dependence of H indicate that the non-adiabatic torque is the main contribution to the DW motion in the ultrathin CoFe/Pd multilayer films.

The spin-torque efficiency ε can be obtained from the slope of the linear dependence of H on J_{th} ($\epsilon = \Delta H/\Delta J_{th}$) [40]. A value of ε = (1.72 ± 0.08) $\times 10^{-14}$ T • m^2/A is derived from Fig. 5-11 (b). This value obtained from the depinning experiment is in well agreement with the result $\varepsilon \sim$（1.68 ± 0.09）$\times 10^{-14}$ T • m^2/A mentioned in the Sec. 5.3.2.

As mention in the section 4.7, the SOT genrated by the Ta layer need to be considered for the DW motion. Figure 5-12 (a) and (b) show the variation of ΔH_L and ΔH_T as function of J for Ta(3)/Pd(3)/[CoFe(0.16)/Pd(0.22))$_8$/Ta(3) sample, respectively using the same measurement methods in the section 4.7.

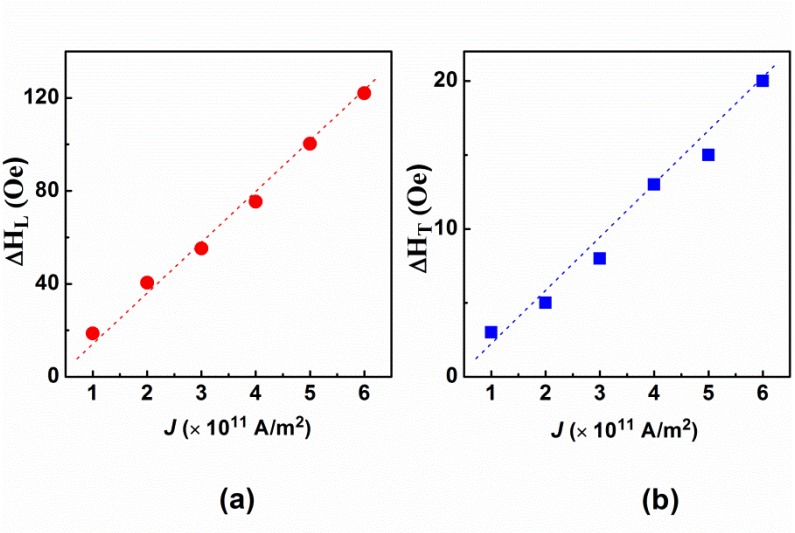

Fig. 5-12 (a) ΔH_L and (b) ΔH_T of the Ta(3)/Pd(3)/[CoFe(0.16)/Pd(0.22)]$_8$/Ta(3) samples, after planar Hall effect correction with different charge current density (J).

It is found that β_L ~ 21 Oe cm^2/10^7 A and the β_T ~ 3 Oe cm^2/10^7 A, in which the damping-like torque arisen by the spin current from Ta layer should be the main source of the SOT in the CoFe/Pd multilayers [78]. In addition, the effective spin Hall angle θ_{SH} = 0.015 is calculated from H_L using the formula [189] $H_L = \hbar\theta_{SH} J/(2eM_s t_F)$, which is slightly smaller than θ_{SH} ~ 0.02 in $(CoFe/Pd)_{15}$ multilayers in section 4.7.

A minimum J_{th} of 5.2×10^{10} A/m^2 is observed under the bias H of 115 Oe as shown in Fig. 5-11 (b) in our device. It is important to note that the DW can steadily propagate in the ultrathin $(CoFe/Pd)_8$ multilayer nanowire with a significantly lower J_{th} combined with a smaller H in comparison with other common Co-based multilayer nanowires, such as Co/Ni (J_{th}~5×10^{11} A/m^2, H~230 Oe) [36] and Co/Pt (J_{th}~1.5×10^{11} A/m^2, H~350 Oe) [40]. In addition, by extrapolating the linear behavior in Fig. 5-11 (b), we find J_{th} ~ 4×10^{11} A/m^2 when bias H = 0, which is still much smaller than other common Co-based multilayer nanowires, such as Co/Ni (J_{th}~1.3×10^{12} A/m^2 when H = 0) [98] and CoFe/Pt (J_{th}~1.43×10^{12} A/m^2 when H = 0) [145].

It is noted that J_{th} is proportional to $(H_{dep} - H)\frac{\alpha M_s \lambda}{P|\beta-\alpha|}$ in PMA films [34, 217], where α is the Gilbert damping and λ is the domain wall width, respectively. The J_{th} is proportional to λ but inversely proportional to β. A smaller J_{th} is observed with a lower strength of SOT compared with $(CoFe/Pd)_{15}$ multilayers in section 4.7. This results indicates a larger β value in ultrathin CoFe/Pd multilayers contribute to a smaller value of J_{th}. A smaller value of H_{dep} is also beneficial as it reduces J_{th}. In principle, CoFe/Pd multilayers would have a small damping as compared to CoFe/Pt

which has a strong spin-orbit coupling due to the presence of Pt. Additionally, a larger DW velocity (v_{max}= 8 m/s with J= 2.48×10^{11} A/m^2 and H = 115 Oe) in ultrathin CoFe/Pd multilayer is observed in Fig. 5-10 as compared to Co/Pt multilayers (v_{max}= 0.02 m/s with J= 5.4×10^{11} A/m^2 and H = 115 Oe) [124, 148].

As mention in Sec. 5.3.1, the formation of superlattice-like structure would lead to a smaller DW pinning strength and H_{dep} as well as the DW velocity can be enhanced in the ultrathin CoFe/Pd multilayer nanowires. Although the heat tolerance of the nanowire device needs to be further improved, all the advantages mentioned above suggest that the ultrathin CoFe/Pd multilayers with alternative CoFe and Pd monatomic sublayers is a promising candidate for the spin-torque DW devices.

5.4 Summary

In summary, a systematic study of effects of the thickness of CoFe and Pd sublayers and then the repeated number (n) on PMA has been carried out. The PMA and post-annealing stability up to 350 ℃ was observed in the ultrathin $(Co_{70}Fe_{30}/Pd)_n$ monatomic layer stacks. The formation of superlattice-like microstructure is a significant factor in enhancing PMA in the ultrathin $(CoFe/Pd)_n$ multilayers. Both saturation magnetization (M_s) and effective PMA constant (K_{eff}) went up proportionally to a maximum value and then decreased as n increased. The reduced PMA strength can be attributed to the destruction of the ordered superlattice-like structure. In addition, we have systematically studied the DW velocity dependence on magnetic field as well as current density in 300 nm-width ultrathin CoFe/Pd

multilayer nanowires. The low threshold current density and relatively high DW velocity are obtained in ultrathin CoFe/Pd multilayer nanowires due to the small depinning field of 120 Oe. The spin torque efficiency of $\varepsilon = (1.68 \pm 0.09) \times 10^{-14}$ T·m^2/A was obtained from two separate methods. The non-adiabatic factor β is estimated to be larger and plays an important role togther with spin orbit torque for current-induced DW motion in ultrathin $[CoFe/Pd]_n$ multilayer nanowires.

Chapter 6 Monatomic $(Co_{70}Fe_{30}/Pd)_n$ superlattice based synthetically antiferromagnetic structure (SAF)

In chapter 5, ultrathin CoFe/Pd multilayers with alternative CoFe and Pd monatomic sublayers is found to be a promising candidate for the spin-torque DW devices, such as racetrack memory (RM) [13]. However, there are still problems remained to be addressed for the application of RM with PMA materials. One of them is the dipolar fringing field from the neighbouring magnetic domains. As the lateral dimension of DW memory bites being scaled down for high-density capacity, the dipolar fringing field increases dramatically and results in strong interaction between adjacent DWs. This will degrade the performance of the device and limit the data density for RM. An efficient solution is to use a synthetic antiferromagnetic (SAF) structure, which consists of two ferromagnetic (FM) layers separated by a nonmagnetic spacer layer. The exchange bias field (H_{ex}) via the spacer layer leads to the magnetic moment in top and bottom FM layers are aligned antiparallel and the fringing field can be considerably reduced.

It is noted that the H_{ex} of the SAF structure is closely related to the exchange coupling strength and PMA strength.[218] The H_{ex} is determined by the antiferromagnetic (AFM) coupling through the spacer layer in SAF structure. The H_{ex} is expressed [219] through the interlayer exchange coupling theory as

$$\mathrm{H_{ex}} = J_{ex}/(M_s t) \tag{6.1}$$

where J_{ex}, M_s and t are AFM coupling strength, saturation magnetization and overall thickness of the top reference layer, respectively. In order to increase H_{ex}, the thickness of the top layer has to be reduced. On the other hand, in commonly used PMA multilayers such as [Co/Pd], [Co/Pt] or [Co/Ni], a large thickness of the multilayers is required to obtain a high PMA. Furthermore, a thicker bottom FM layer, which is further away from the FL than the top FM layer, has to be used to compensate the spatial loss of the magnetostatic field [220] in the SAF structure. This would result in the stack being too thick and cause degradation of device performance induced by etching process [221]. In order to suppress the stray field and shorten the etching time, it is of practical necessity to reduce the thickness of multilayer while keeping high PMA. Additionally, a post-annealing stability up to 350 ℃ for SAF structure is required in the fabrication process for long-time usage of the spin-DW devices [192]. Therefore the maintenance of H_{ex} and PMA of SAF structure after high temperature post annealing up to 350 ℃ are also of great importance.

In this chapter, we described the study of the variation of H_{ex} and PMA dependence on the thickness of Ru spacer layer and insertion of the Pd layer in ultrathin $(Pd/Co_{70}Fe_{30})_9/Ru/Pd/(Co_{70}Fe_{30}/Pd)_9$ SAF structure. The AFM coupling and PMA strength could be enhanced by inserting Pd layer with a suitable thickness between the Ru and ultrathin top $(CoFe/Pd)_9$ multilayers. The effect of annealing temperature on the PMA and AFM coupling was also discussed.

6.1 Characterization of monatomic $(Co_{70}Fe_{30}/Pd)_n$ based SAF structure film

6.1.1 Measurement method

The stack structure was $Si/SiO_2/Ta(3)/Pd(3)/[CoFe(0.16)/Pd(0.22)]_8/CoFe(0.16)/Ru(t_{Ru})/Pd(t_{Pd})/[CoFe(0.16)/Pd(0.22)]_9/Ta(3)$ (all the number in brackets is the layer thickness with unit in nanometer), where t_{Ru} ranged from 0.4 to 1.1 nm and t_{Pd} was varied from 0 to 0.5 nm. The thickness of CoFe and Pd monatomic layers were fixed at 0.16 nm and 0.22 nm, respectively. The samples were annealed at a vacuum of 5×10^{-9} Torr for 1 hour with different temperature ranging from 200 ℃ to 400 ℃. The magnetic hysteresis loops were measured at room temperature using alternating gradient force magnetometer (AGFM) under a maximum magnetic field of 1.5T applied perpendicular to the plane of the samples.

6.1.2 Characterization of as-deposited monatomic $(Co_{70}Fe_{30}/Pd)_n$ based SAF structure film

Figures 6-1 (a) and (b) show the typical magnetic hysteresis (M-H) loops for $[CoFe/Pd]_8/CoFe/Ru(0.7)/[CoFe/Pd]_9$ and $[CoFe/Pd]_8/CoFe/Ru(0.7)/Pd(0.2)/[CoFe/Pd]_9$ samples measured at room temperature under magnetic field (H) perpendicular to the plane of the film, respectively. Both loops demonstrate that magnetization reversal appears before the magnetic field reaches zero as the magnetic field reduces from saturation field. This result indicates that the two ferromagnetic [CoFe/Pd] multilayers

are antiferromagnetically coupled through the spacer in both SAF structured samples. Comparing the minor loops of both samples, the sample with 0.2 nm Pd insertion layer between Ru spacer and [CoFe/Pd] multilayers has a sharp magnetization reversal behavior, while the sample without Pd insertion shows a slant magnetization switching. The gradient M-H minor loops of the top [CoFe/Pd] multilayers in Fig. 6-1 (a) indicates the easy axis of the magnetization is not fully perpendicular to film plane when the [CoFe/Pd] multilayers are deposited on Ru. On the other hand, the squared minor loop for the sample in Fig. 6-1 (b) demonstrates the easy axis is perpendicular to the film plane. These results show that the top [CoFe/Pd] multilayer possess a higher PMA grown on Pd insertion layer than on Ru [222].

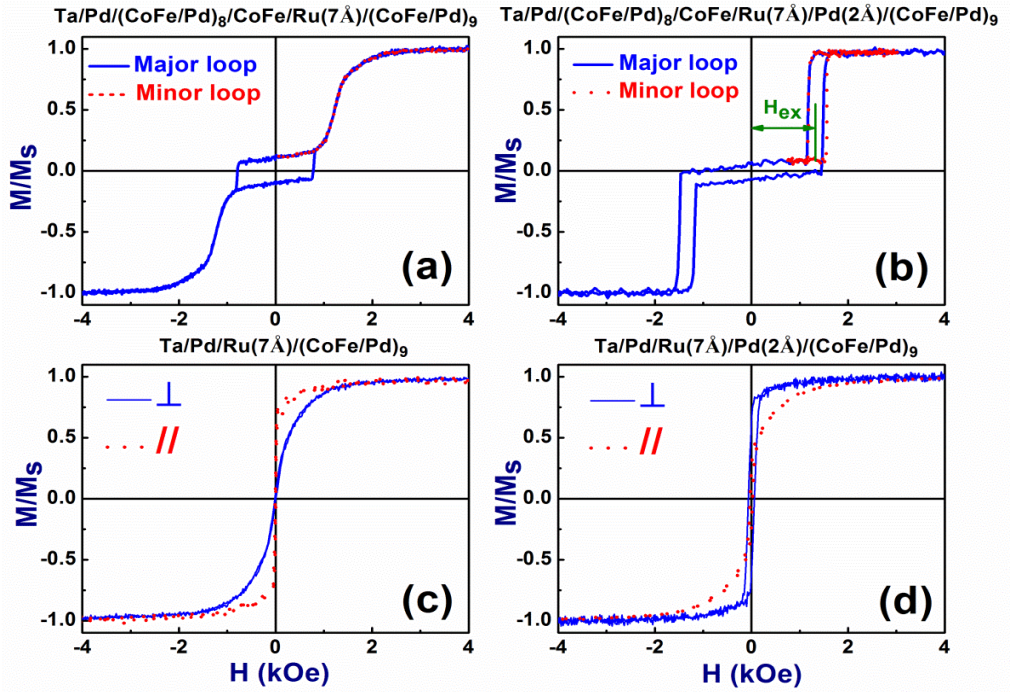

Fig. 6-1 Normalized out-of-plane hysteresis loop for samples of (a) Ta(3)/Pd(3)/[CoFe(0.16)/Pd(0.22)]$_8$/CoFe(0.16)/Ru(0.7)/[CoFe(0.16)/Pd(0.22)]$_9$ and (b) Ta(3)/Pd(3)/[CoFe(0.16)/Pd(0.22)]$_8$/CoFe(0.16)/Ru(0.7)/Pd(0.2)/[CoFe(0.16)/Pd(0.22)]$_9$. Normalized hysteresis (M–H) loops of (c) Ta(3)/Pd(3)/Ru(0.7)/[CoFe(0.16)/Pd(0.22)]$_9$ and (d) Ta(3)/Pd(3)/Ru(0.7)/Pd(0.2)/[CoFe(0.16)/Pd (0.22)]$_9$. The ∥ indicates the loops measured with magnetic field (*H*) in the plane of sample film and ⊥ indicates H is out of plane of the sample film. All the film thickness is measured in nm unit.

Figure 6-1 (c) and (d) show the M-H loops for the Ta(3)/Pd(3)/Ru(0.7)/ $[CoFe/Pd]_9$ and Ta(3)/Pd(3)/Ru(0.7)/Pd(0.2)/$[CoFe/Pd]_9$ samples measured under the applied magnetic field in two different directions. It can be observed in Fig. 6-1 (c) that the in-plane loop has an easy-axis behavior whereas the out-of-plane loop displays a hard-axis behavior. This indicates that the Ta/Pd/Ru/$[CoFe/Pd]_9$ sample has an in-plane magnetic anisotropy (IMA). Figure 6-1 (d) shows that the Ta/Pd/Ru/Pd/$[CoFe/Pd]_9$ sample exhibits a well-developed PMA because of the Pd insertion. Therefore, we can conclude that the minor loops in Fig. 6-1 (a) and (b) correspond to the switching behavior of the top $[CoFe/Pd]_9$ multilayer. Although the top and bottom multilayers have equal number of repeated bilayers (n) and same composition, the net magnetic moment is beyond zero at the remanent state as well as the magnetization reversal occurs in top $[CoFe/Pd]_9$ multilayers prior to the bottom ones. This suggests that the top multilayers have a smaller PMA than the bottom ones. The larger PMA in the bottom multilayers is attributed to the improvement of a better crystalline structure of $[CoFe/Pd]_9$ multilayers grown on a thicker Pd (3 nm) seed layer.

To further confirm that the thin Pd insertion together with Ru layer induces a higher PMA than a single Ru layer, the variation of the effective magnetic anisotropy (K_{eff}) as functions of the Ru thickness and inserted Pd layer thickness were studied. Figures 6-2 (a) and (b) show the respective K_{eff} in the Ta(3)/Pd(3)/Ru(t_{Ru})/ $[CoFe(0.16)/Pd(0.22)]_9$ as a function of t_{Ru} ranging from 0.4 to 1.5 nm and Ta(3)/Pd(3)/Ru(0.7)/Pd(t_{Pd})/$[CoFe(0.16)/Pd\ (0.22)]_9$ as a function of t_{Pd} from 0 to 0.5

nm. The results show that K_{eff} increases with increasing both t_{Ru} and t_{Pd}. The negative value of K_{eff} is observed when t_{Ru} is less than 1.2 nm in Fig. 6-2 (a) and t_{Pd} is smaller than 0.2 nm in Fig. 6-2 (b). This behavior indicates the existence of IMA which is attributed to the interfacial and crystalline anisotropy is not strong enough to overcome the demagnetizing anisotropy. When the t_{Ru} is larger than 1.2 nm or t_{Pd} is above 0.2 nm, the PMA dominates with the appearance of positive K_{eff}.

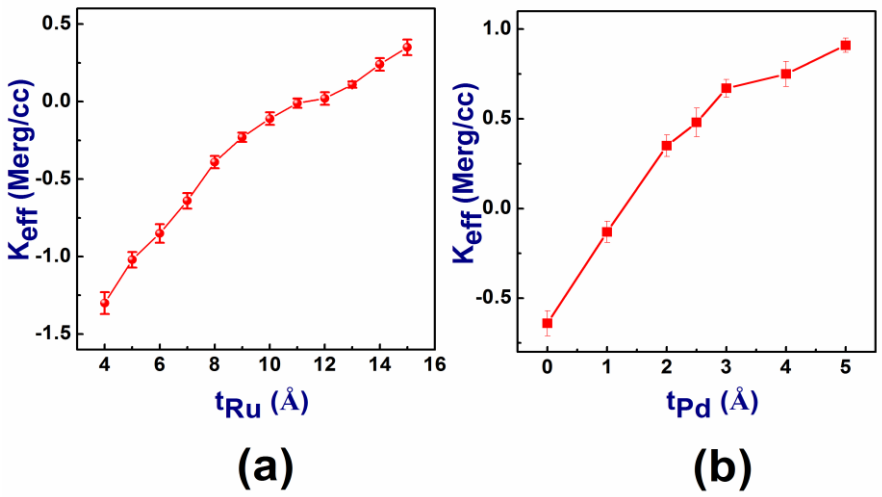

Fig. 6-2 The K_{eff} as a function of t_{Ru} in the Ta(3)/Pd(3)/Ru(t_{Ru})/[CoFe(0.16)/Pd(0.22)]$_9$ and (b) K_{eff} as a function of t_{Pd} in the Ta(3)/Pd(3)/Ru(0.7)/Pd(t_{Pd})/[CoFe(0.16)/Pd(0.22)]$_9$.

It is noteworthy that with the similar thickness of 0.9 nm, the composite Ru(0.7 nm)/Pd(0.2 nm) layer induces higher PMA than a single Ru layer. The XRD measurements are performed to further understand the mechanism of higher PMA induced by Ru(0.7)/Pd(0.2) layer. Figure 6-3 shows the XRD 2Θ scans for Ta(3)/Pd(3)/Ru(0.9)/[CoFe(0.16)/Pd(0.22)]$_9$ (solid line) and Ta(3)/Pd(3)/Ru(0.7) /Pd(0.2)/[CoFe(0.16)/Pd(0.22)]$_9$ (dashed line) samples. Both samples have the same total thickness but different spacer layers, which are Ru(0.9) and Ru(0.7)/Pd(0.2),

respectively. The diffraction peak can be observed at 2θ = 40.7° due to the fcc (111) texture of CoFe/Pd multilayers for both samples. The basic spectrum is unchanged for both samples. However, the peak intensity of fcc (111) reflection for the Ru(0.7)/Pd(0.2) sample increases by ~56% as compared with the peak intensity of the Ru(0.9) sample. In addition, the full peak width at half maximum height (FWHM) of Ru(0.7)/Pd(0.2) sample decreases by ~ 20% in comparison with that of the Ru(0.9) sample, showing that the Ru(0.7)/Pd(0.2) sample has a better fcc (111) orientation than the Ru(0.9) sample. All these results indicate that the enhanced PMA of CoFe/Pd multilayers deposited on the Ru(0.7)/Pd(0.2) can be attributed to the better fcc (111) texture induced by the inserted Pd layer.

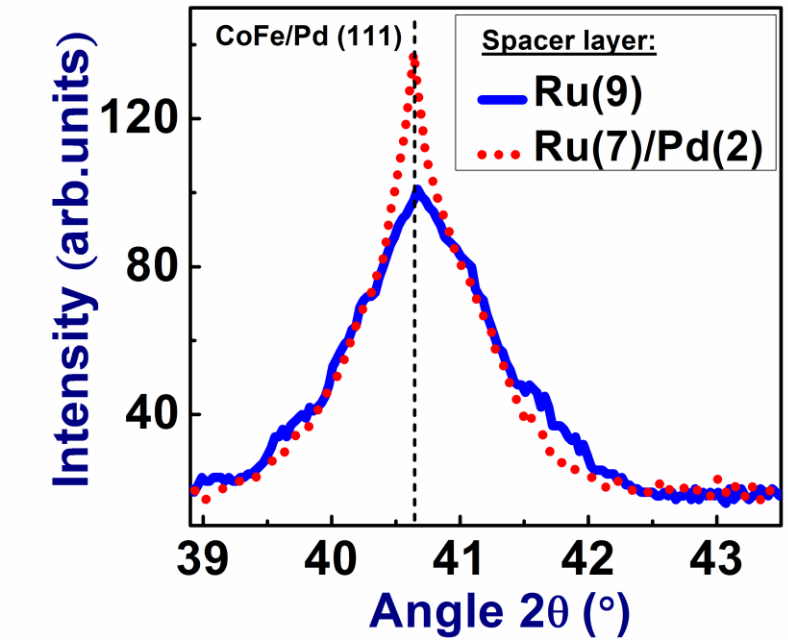

Fig. 6-3 The XRD 2Θ scans for Ta(3)/Pd(3)/ Ru(0.9)/[CoFe(0.16)/Pd(0.22)]$_9$ (solid and blue line) and Ta(3)/Pd(3)/Ru(0.7)/Pd(0.2)/[CoFe(0.16)/Pd(0.22)]$_9$ (dashed and red line) samples.

The H_{ex} is defined as the field shifts from the center of the minor hysteresis loop to zero [218, 219, 223] as shown in Fig. 6-1 (b). By comparing the minor loops in Fig. 6-1 (a) and (b), we found that the sample with 0.2 nm Pd insertion layer exhibits a

larger H_{ex} value (1.37 kOe) than the one without Pd insertion (1.23 kOe). As mentioned above, since the top $[CoFe/Pd]_9$ multilayers have the same saturation magnetization and total thickness in both samples, the larger H_{ex} in $[CoFe/Pd]_8$/CoFe/Ru/Pd(0.2 nm)/$[CoFe/Pd]_9$ indicates the sample with Pd insertion between Ru and top [CoFe/Pd] multilayers exhibits a larger interlayer coupling J_{ex} as compared with the sample without Pd insertion.

In order to further understand the mechanisms underlying PMA interlayer coupling, the H_{ex} in the $[CoFe/Pd]_8$/CoFe/Ru(t_{Ru})/Pd(t_{Pd})/$[CoFe/Pd]_9$ SAF structure samples with different thicknesses of Pd insertion layer (t_{Pd}) as well as Ru layer (t_{Ru}) were measured. Figure 6-5 shows the variation of H_{ex} as a function of Ru thickness for various thicknesses of Pd insertion layer. A maximum H_{ex} of 2.13 kOe is observed at t_{Ru} = 0.5 nm and t_{Pd} = 0.3 nm. We measured the M_s for the Ta(3)/Pd(3)/ Ru(0.5)/Pd(0.3)/$[CoFe(0.16)/Pd(0.22)]_9$ films using the AGM and M_s = 720 emu/cc for Ta(3)/Pd(3)/Ru(0.5)/Pd(0.3)/$[CoFe(0.16)/Pd(0.22)]_9$ is then obtained. By taking M_s = 720 emu/cc and the total top reference layer thickness of 3.42 nm, a strong interlayer coupling J_{ex} = 0.522 erg/cm^2 is obtained for the $[CoFe/Pd]_8$/CoFe/Ru(0.5)/ Pd(0.3)/$[CoFe/Pd]_9$ sample. The M_s is measured by taking the ratio of magnetic moment (m) of $[CoFe/Pd]_9$ multilayers and the total volume of CoFe/Pd multilayers. In comparison with other SAF structures with Co based multilayers such as CoFeB/Pt (H_{ex} ~ 1.1 kOe, J_{ex} ~ 0.09 erg/cm^2) [219], Co/Pd (H_{ex} ~ 1.05 kOe) [224], the larger H_{ex} and higher PMA are achieved in our sample with Pd insertion. These results suggest

that the SAF structure with two ultrathin [CoFe/Pd] multilayers separated by the Ru/Pd spacer is a promising candidate for DW application.

It is well known that the interlayer coupling between the top and bottom CoFe/Pd multilayers originates mainly via three different interactions, namely indirect exchange Ruderman-Kittel-Kasuya-Yosida (RKKY) coupling because of the conduction electron reflection at the spacer interfaces [7, 225], magnetostatic orange peel (Néel) coupling due to the roughness between the non-magnetic and magnetic interfaces [226], and the stray field induced the magnetostatic coupling rising from the multi-domain state in both the top and bottom multilayers [227]. The RKKY coupling oscillates and its amplitude decays with t_{Ru}, showing a behavior between ferromagnetic (FM) and anti-ferromagnetic (AFM) properties according to the space layer material and thickness whereas the orange peel coupling decreases with increasing the thickness of the spacer layer [225]. The previous report [226] shows that the perpendicular orange peel coupling favors FM coupling when the spacer layer thickness is less than 3.5 nm. In our study, the thickness of the spacer layer is in the range of 0.4 to 1.7 nm. This means the perpendicular orange peel coupling exhibits the FM coupling.

For the magnetostatic coupling, Fig. 6-4 depicts the MFM images of the demagnetized remanent magnetic domain structure for $[CoFe/Pd]_8$/CoFe/Ru(0.7)/ Pd(0.2)/$[CoFe/Pd]_9$ sample. A uniform magnetization state is clearly observed and the stripe domain structure (multi-domain state) does not exist at the remanent state in our SAF structure. This presents a uniform SAF structure that is ferromagnetically

correlated in the CoFe/Pd multilayers and antiferromagnetic coupling between the top and bottom CoFe/Pd multilayers [228]. The stripe domains are hardly observed; indicating that the stray field induced the magnetostatic coupling can be negligible in our experiment. Besides the interactions mentioned above, the strong hybridization appearing at the Pd/CoFe interface should also be considered. Firstly, the hybridization between 3d electrons of Fe (Co) and 4d electrons of Pd will cause the variation of the exchange splitting and polarization in the CoFe layer. The hybridization will induce the interfacial PMA anisotropy in $[CoFe/Pd]_n$ multilayers and form the FM coupling, which will influence the interlayer coupling in the SAF structure [229]. Therefore the interlayer coupling in the SAF structure is affected by the Pd thickness in $[CoFe/Pd]_n$ multilayers. Since the Pd thickness in $[CoFe/Pd]_n$ multilayers is fixed, the FM coupling generated from $[CoFe/Pd]_n$ multilayers is treated as a constant in our study. Secondly, the Pd insertion layer with Ru can work as a composite spacer layer in the SAF structure, which will affect the interlayer coupling and thus determine the H_{ex}. This will be discussed in detail in the following paragraph.

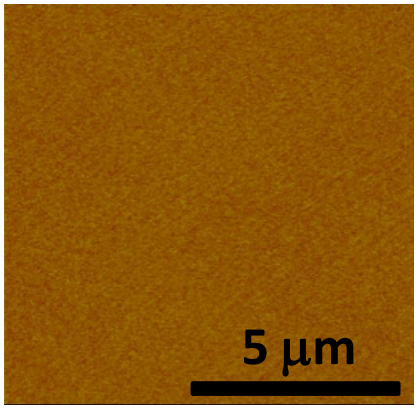

Fig. 6-4 The MFM image of the remanent magnetic domain structure for $[CoFe/Pd]_8$/CoFe/ Ru(0.7)/Pd(0.2)/$[CoFe/Pd]_9$ sample.

Figure 6-5 shows that H_{ex} exhibits an oscillatory-like behavior with increasing Ru thickness. In previous reported Co/Pt-multilayers-based SAF structures [219, 229-231], it is expected that RKKY coupling is AFM when the thickness of Ru spacer is in the range of 0.4 to 1.1 nm. The RKKY coupling shows a oscillating behavior and its amplitude decays exponentially with t_{Ru} [231].Therefore the oscillatory-like behavior of H_{ex} with t_{Ru} in the range of 0.4 to 1.1 nm can be attributed to the competition between the AFM RKKY coupling and the FM coupling from the orange peel as well as CoFe-Pd hybridization. All the samples with t_{Ru} in the range of 0.4 to 1.1 nm exhibit positive values of H_{ex}, indicating that the interlayer coupling is AFM. This shows that AFM RKKY coupling is dominant for the interlayer coupling in our samples rather than the FM coupling.

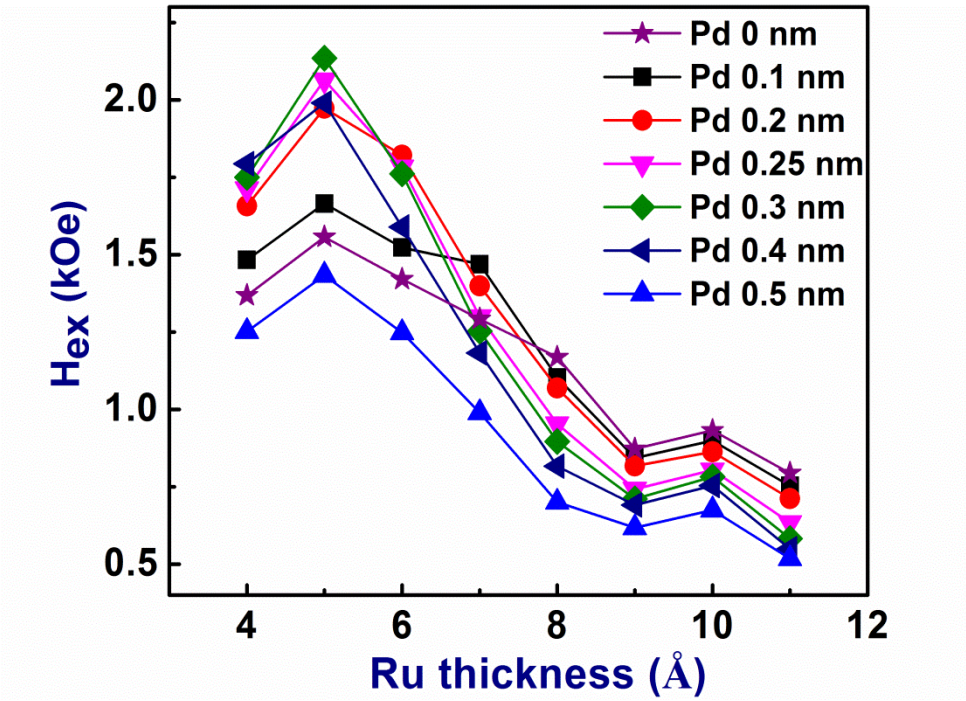

Fig. 6-5 The exchange coupling field H_{ex} in Ta(3)/Pd(3)/[CoFe(0.16)/Pd(0.22)]$_8$/ CoFe(0.16)/Ru(t_{Ru})/Pd(t_{Pd})/[CoFe(0.16)/Pd(0.22)]$_9$ (unit in nm) SAF structure samples as functions of the thickness of Ru (t_{Ru}) ranging from 0.4 nm to 1.1 nm for various Pd insertion layer thicknesses.

As shown in Fig. 6-5, there are two peaks for H_{ex} appearing at t_{Ru} = 0.5 nm and t_{Ru} = 1 nm. Additionally, the positions of these two peaks for H_{ex} remain unchanged with varying the insertion Pd layer. The first and second peak position with t_{Ru} is consistent with other Co-based SAF structures with PMA [218, 229, 232]. The two peaks of H_{ex} appearing in the AFM RKKY coupling region may be due to a superposition of two period oscillation behavior and the positions of two peaks are mainly related to the density of state of Ru [233]. This is because the Fermi level lies within the wide d band in Ru and the two Fermi wave vectors from both d and s(p) electrons generate the different periods of the oscillation behavior [229]. Thus, both d and s(p) electrons are considered to take part in the interferences and are accounted for the two long-period oscillation. On the other hand, in order to further understand the variation of H_{ex} dependent on t_{Pd}, we plotted the H_{ex} as a function of t_{Pd} for various t_{Ru}. Figure 6-6 depicts the H_{ex} as a function of Pd insertion layer thickness for the various Ru thicknesses (t_{Ru}). It reveals that H_{ex} exhibits a non-monotonic behavior with increasing t_{Pd} for t_{Ru} < 0.8 nm while the H_{ex} monotonically decreases with increasing t_{Pd} for $t_{Ru} \geqslant$ 0.8 nm. For t_{Ru} < 0.8 nm, the H_{ex} increases with increasing t_{Pd} to a maximum value and then decreases with further increasing t_{Pd}. It can be seen that the maximum peak position of H_{ex} shifts to a smaller t_{Pd} with increasing t_{Ru}. These results suggest the H_{ex} is not only dependent on the t_{Ru}, but also relied on the Pd insertion layer thickness.

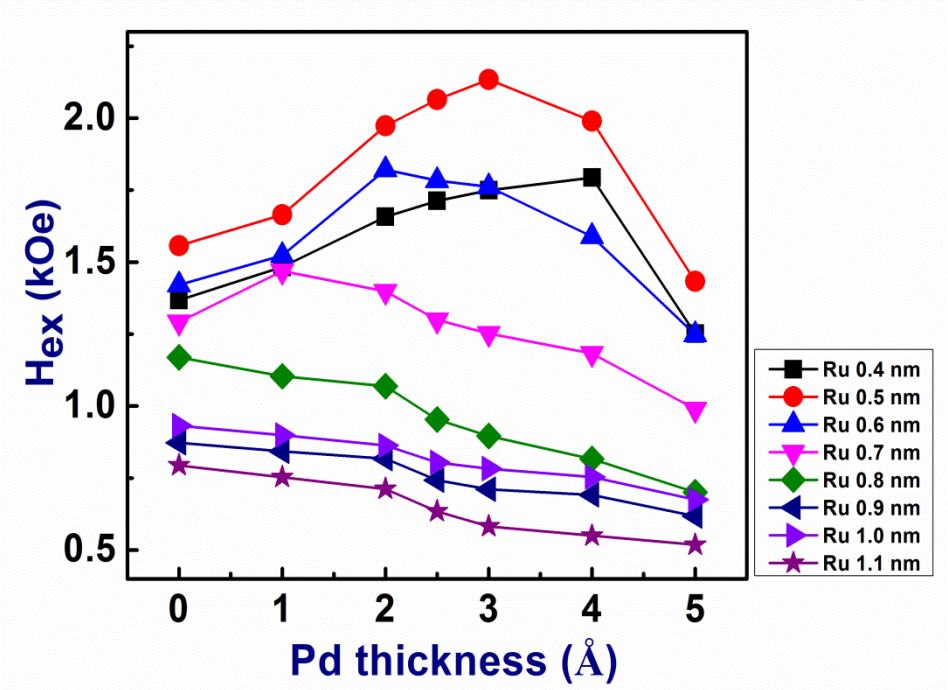

Fig. 6-6 The exchange coupling field H_{ex} in Ta(3)/Pd(3)/[CoFe(0.16)/Pd(0.22)]$_8$/CoFe(0.16)/Ru(t_{Ru})/Pd(t_{Pd})/[CoFe(0.16)/Pd(0.22)]$_9$ (unit in nm) SAF structure samples as functions of the thickness of Pd insertion layer ranging from 0 nm to 0.5 nm for various Ru thickness.

The maximum peaks of H_{ex} appears when the $t_{Pd} + t_{Ru}$ is around 0.8 nm (t_{Ru} = 0.5 nm and t_{Pd} = 0.3 nm) with fixed t_{Ru} ($t_{Ru} \leq$ 0.8 nm) as shown in Fig. 6-6. The non-monotonic variation of H_{ex} with t_{Pd} for t_{Ru} < 0.8 nm may be attributed to the thin Pd insertion between Ru and CoFe layers. For the SAF structure without Pd insertion, the Ru-CoFe interdiffusion will cause the top and bottom multilayers to form direct FM contact when t_{Ru} is small. Therefore, the Ru-CoFe interdiffusion will cause a FM coupling between top and bottom CoFe/Pd multilayers with decreasing t_{Ru}. However, the Pd insertion suppresses the Ru-CoFe interdiffusion, which will increase the AFM coupling. For a smaller t_{Ru}, the thicker Pd insertion layer is needed to suppress the Ru-CoFe interdiffusion and increase AFM coupling. For example, the maximum value of H_{ex} (1.47 kOe) was obtained at t_{Pd} = 0.1 nm when t_{Ru} is fixed at 0.7 nm whereas when t_{Ru}=0.4 nm, the H_{ex} increases to a maximum of 1.75 kOe with

increasing t_{Pd} to 0.4 nm. In addition, when the $t_{Ru} + t_{Pd}$ is increased beyond 0.8 nm, the Pd insertion may reduce the interfacial electron polarization and lead to a dramatically decrease in H_{ex} [230]. Therefore, the Pd insertion layer can work together with Ru layer as a composite Ru/Pd spacer to tune the interlayer coupling. Although the PMA of top CoFe/Pd multilayers can be enhanced with increasing thickness of Pd insertion layer up to 0.5 nm as shown in Fig. 6-2 (b), there is a trade-off between the RKKY coupling and PMA by varying the thickness of Ru and Pd insertion layer.

6.1.3 The post-annealing effect on the magnetic properties of monatomic $(Co_{70}Fe_{30}/Pd)_n$ based SAF structure film

Figure 6-7 shows a series of normalized out-of-plane hysteresis loops of $[CoFe/Pd]_8$/CoFe/Ru(0.8)/Pd(0.3)/$[CoFe/Pd]_9$ sample (unit in nm) as-deposited and annealed for 1 hour at various temperature ranging from T_a = 250 ℃ to 380 ℃ and the corresponding minor loops is shown in the inset. It is interesting to note that the H_{ex} increases with increasing T_a up to 350 ℃. This result is in contrast to the previous report of other SAF structures with Co based multilayers [219, 230, 234, 235], where the H_{ex} decreases with increasing T_a, which is due to the annealing-induced increase in interdiffusion between the different layers.

The increase in interface diffusion can cause the creation of pinholes and lead to the reduction of the interlayer coupling and H_{ex}. The behavior of H_{ex} increases with increasing T_a up to 350 ℃ is not completely understood yet. One possible reason could be due to the ultrathin $[(CoFe(0.16\ nm)/Pd(0.22\ nm)]_9$ multilayers which

possess a high post-annealing stability up to 350 ℃. The formation of an ordered superlattice-like structure [192, 202] and the PMA of the multilayers can be enhanced with increasing T_a up to 350 ℃. The superlattice-like structure can restrain the interface diffusion and decrease the creation of the pinholes through the spacer. Therefore, we infer that our result can be attributed to the interdiffusion between ultrathin [CoFe/Pd] multilayers and Ru is suppressed during annealing due to the existence of superlattice-like structure.

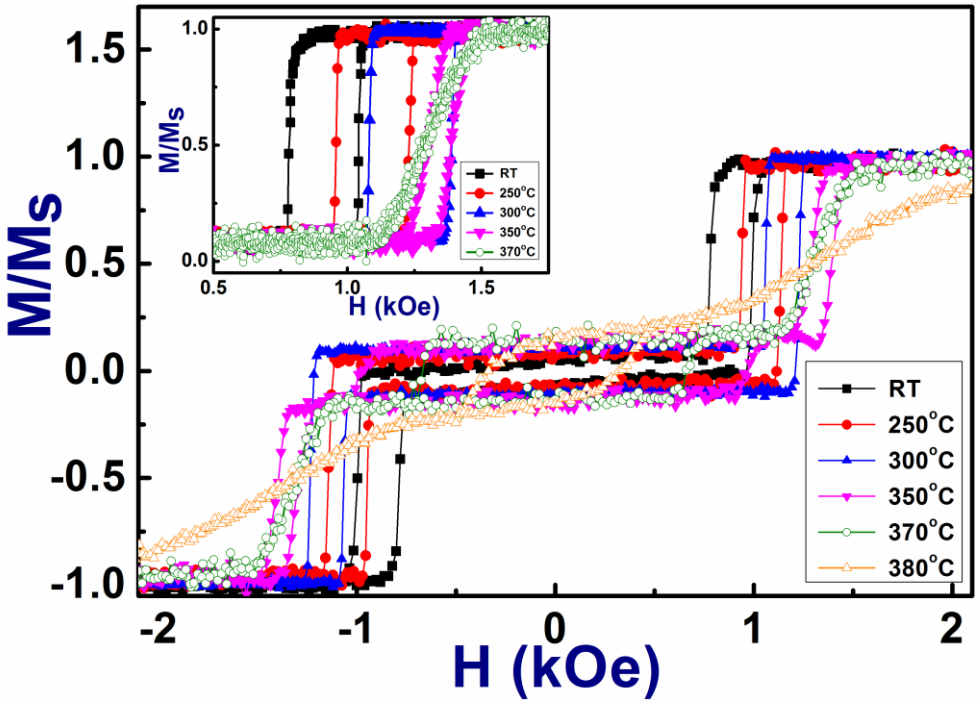

Fig. 6-7 Normalized out-of-plane hysteresis loops of $[CoFe(0.16)/Pd(0.22)]_8/CoFe(0.16)/Ru(0.8)/Pd(0.3)/[CoFe(0.16)/Pd(0.22)]_9$ (unit in nm) samples as-deposited and annealed at various T_a. The inset shows the minor loops of the same sample as-deposited and annealed at various T_a.

In addition, the electron mobility in Ru/Pd can be enhanced with increasing the T_a [236]. This feature may cause a change in the structural properties and has an advantage in enhancing the H_{ex} with increasing T_a. This is in agreement with the quantum interference model proposed by Bruno [237]. When the T_a is further increased to 370 ℃, the H_{ex} starts to reduce as the minor loop presents a canted

switching behavior. This indicates the magnetic anisotropy starts to change from PMA to IMA and possibly due to the destruction of the [CoFe/Pd] fcc (111) ordered structure at T_a > 370 ℃ and the reduction of H_{ex} caused by excessive interdiffusion.

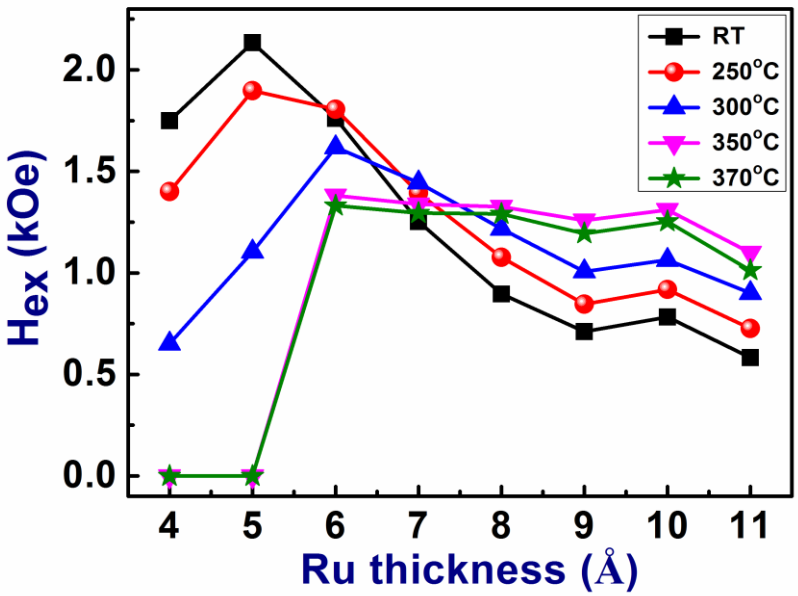

Fig. 6-8 The exchange coupling field H_{ex} in Ta(3)/Pd(3)/[CoFe(0.16)/Pd(0.22)]$_8$/CoFe(0.16)/ Ru(t_{Ru})/Pd(0.3)/[CoFe(0.16)/Pd(0.22)]$_9$ (unit in nm) SAF structure samples as functions of the Ru (t_{Ru}) thickness ranging from 0.4 nm to 1.1 nm for the as-deposited state and annealed at various T_a ranging from 250 ℃ to 370 ℃.

The theoretical model [238] predicts that H_{ex} would reduce with increasing T_a. Figure 6-8 shows the H_{ex} as a function of t_{Ru} in the [CoFe/Pd]$_8$/CoFe/Ru(t_{Ru})/ Pd(0.3)/[CoFe/Pd]$_9$ samples (unit in nm) for various T_a. Our results show that H_{ex} does not monotonically decrease with T_a as t_{Ru} varies from 0.4 to 1.1 nm. The H_{ex} of individual sample with t_{Ru} > 0.7 nm increase to a respective maximum value as T_a increases from room temperature to 350 ℃ and decrease with further increasing T_a to 370 ℃. We note that the maximum H_{ex} is achieved at T_a = 300 ℃ when t_{Ru} = 0.6 nm and H_{ex} has a maximum value at T_a = 250 ℃ for t_{Ru} = 0.5 nm. As the t_{Ru} is further

reduced to less than 0.5 nm, H_{ex} reaches a maximum value for the as-deposited sample. When $t_{Ru} \leqslant 0.7$ nm, the position of maximum H_{ex} shifts to a smaller T_a with decreasing t_{Ru}. In addition, $H_{ex} = 0$ is when T_a is above 300 ℃ for $t_{Ru} \leqslant 0.5$ nm, indicating the sample is completely ferromagnetic coupling after annealing. This result could be explained based on the formation of the pinholes.

The pinholes can induce the two ferromagnetically coupled magnetic layers and thus causing the reduction of AFM coupling strength. As the t_{Ru} is reduced which corresponds to a thinner spacer, the pinholes are more easily formed. In addition, the orange peel induced ferromagnetic coupling between the top and bottom CoFe/Pd multilayers will increase with reducing t_{Ru}, which will also cause the reduction of AFM coupling strength. Although maximum of H_{ex} (~ 1.5 kOe) and J_{ex} (~ 0.39 erg/cm^2) of our as-deposited SAF structure with $t_{Ru} \geq 0.7$nm are slightly smaller than those of the previous Co/Pt multilayers based SAF structure (H_{ex} ~ 1.8 kOe, J_{ex} ~ 0.46 erg/cm^2) [230], the post-annealing stability with high T_a is significantly improved in our ultrathin (CoFe/Pd) multilayers based SAF structure. It is found that PMA is maintained and H_{ex} is enhanced with increasing T_a ($t_{Ru} \geq 0.7$nm) in our samples, whereas H_{ex} dramatically decreases with increasing T_a up to 350 ℃ in the previous reported SAF structure [230].

6.2 Summary

In summary, the effects of the Pd insertion and annealing temperature on the interlayer exchange field H_{ex} and PMA in ultrathin (CoFe/Pd) multilayers based SAF

structure have been systematically studied. The H_{ex} exhibits an oscillatory decay behavior with a period of 0.5 nm and H_{ex} is dependent on the thickness of both Ru layer and Pd insertion layer. A maximum J_{ex} of 0.522 erg/cm^2 is achieved at room temperature and H_{ex} presents a strong dependence on annealing temperature T_a. The enhancement of H_{ex} and PMA with Pd insertion and increase in T_a up to 350 ℃ for t_{Ru} >0.7 nm in this SAF structure can be attributed to the suppression of the creation of pinholes due to Ru/Pd spacers and a better ordered [CoFe/Pd] multilayer structure.

Chapter 7 Current induced domain wall motion in SAF structure based nanowires

Besides reducing the dipolar fringing field from the neighbouring magnetic domains for high-density capacity as discussed in chapter 6, a reasonably low current density to control the DW motion and high DW velocity for high speed devices are also needed to fulfill the requirements of practical devices. D. Ravelosona *et al.* [34] found that J_{th} for DW motion is proportional to net saturation magnetization in PMA films. In the SAF structure, as the top and bottom FM layers are aligned antiparallel, the net M_s equals to $|M_{s1} - M_{s2}|$, where M_{s1} and M_{s2} are the saturation magnetization of the top and bottom FM layers, respectively. Thus the net magnetization of this SAF structure is considerably reduced and decreased J_{th}. On the other hand, the simulation result predicts that antiferromagnetically (AFM) coupled magnetic nanowire exhibit larger DW velocity in comparison with a single-phase-ferromagnetic nanowire [239]. All these factors indicate that the SAF structure is a promising candidate for spin-torque DW devices. Furthermore, we show that ultrathin $(Pd/Co_{70}Fe_{30})_9$/Ru/Pd/ $(Co_{70}Fe_{30}/Pd)_9$ SAF structure possesses high interlayer exchange coupling. The high interlayer coupling field (H_{ex}) and PMA are maintained after high temperature post-annealing up to 350 ℃ in this SAF structure, which would enhance the stability of the device for a long-time usage.

In this chapter, we have investigated the current induced DW motion in $(Pd/Co_{70}Fe_{30})_9$/Ru/Pd/$(Co_{70}Fe_{30}/Pd)_9$ SAF structure and systematically studied the

variation of J_{th} and DW velocity dependent on $|M_{s1} - M_{s2}|$. A smaller J_{th} of 9.2×10^{10} A/m^2 and a maximum v of 150 m/s under J = 1.5×10^{12} A/m^2 for DW motion were observed, which can be attributed to a smaller net magnetization in the SAF structure nanowire.

7.1 Current induced domain wall motion in the SAF structure based nanowires

7.1.1 Measurement methods

The stacks of SAF structures experiment was Si/SiO_2/Ta(3)/Pd(3)/[CoFe (0.16)/Pd(0.22)]$_8$/CoFe(0.16)/Ru(0.8)/Pd(0.2)/[CoFe(0.16)/Pd(0.22)]$_N$/Ta(3) (all the number in brackets is the thickness of the layer with unit in nanometer), where N ranged from 4 to 9. The 25 μm-long and 300 nm-wide nanowires were fabricated by means of electron beam lithography and Ar ion-milling process. The Au electrodes with the thickness of 40 nm were deposited on the contact pad and wire to inject current along the nanowire and detect the DW motion by anomalous Hall effect (AHE). All measurements were performed at room temperature. The nucleation of single DW was imaged using magnetic force microscopy (MFM) measurement at the remanent state. The duty cycle and pulse width (t_p) of each pulse current in the DW velocity (v) measurements were fixed at 1/1000 and 5 ns, respectively.

7.1.2 Threshold current density of DW motion in the SAF structure based nanowires

Figure 7-1 shows the normalized perpendicular magnetization hysteresis loops (*M-H*) for 300 nm-width nanowire with a structure of $[CoFe/Pd]_8/CoFe/Ru/Pd/[CoFe/Pd]_N$ with N=5, 6 and 7. The schematic diagrams present the magnetization configuration in SAF structure. All the M-H loops show sharp reversal behavior, indicating that the CoFe/Pd multilayers exhibit typical PMA. When H reaches the saturation field (> 2000 Oe), the magnetic moments of top (FM1) and bottom (FM2) multilayers are aligned parallel and the magnetization of the SAF structure equals to $M_s = |M_{s1} + M_{s2}|$ at this state, where M_{s1} and M_{s2} are the saturation magnetization of the top and bottom FM layers, respectively. As H reduces from the saturation field, all the M-H loops show the magnetization reversal appears before H reaches zero. This result indicates that two ferromagnetic [CoFe/Pd] multilayers are antiferromagnetically coupled through the spacer layer Ru in all SAF structured samples. At the remanent state, the magnetic moments of FM1 and FM2 are aligned antiparallel and the net magnetization of the SAF structure is $M_n = |M_{s2} - M_{s1}|$. When H is reversed, FM1 and FM2 couple together and operate as a single magnet to switch with H in the range of ± 1 kOe. This is due to the large antiferromagnetic coupling strength between FM1 and FM2 that dominate the net magnetic moment reversal [240]. We can define $m_r = \frac{|M_{s2} - M_{s1}|}{|M_{s1} + M_{s2}|}$. The equation $M_n = |M_{s2} - M_{s1}| = \frac{2m_r}{1+m_r}M_{s2}$ is then obtained. Since the bottom CoFe/Pd multilayers is fixed, a constant M_{s2} = 452 emu/cc is measured by taking the ratio of magnetic moment of bottom CoFe/Pd

multilayers and the total volume of bottom CoFe/Pd multilayers. Additionally, m_r can be obtained from the M-H loops.

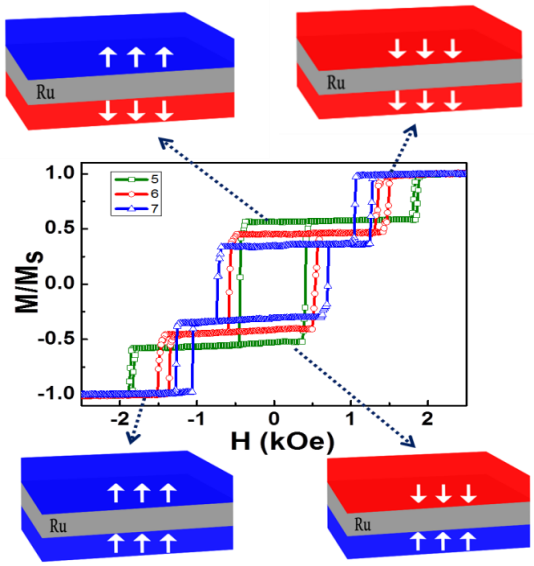

Fig. 7-1 Normalized Hall resistance hysteresis loops (R_H-H) for 300 nm-width nanowire. The structure is Ta(3)/Pd(3)/[CoFe(0.16)/Pd(0.22)]$_8$/CoFe(0.16)/Ru(0.8)/Pd(0.2)/[CoFe(0.16)/Pd(0.22)]$_N$/Ta(3) with N=5, 6 and 7. The R_H-H loops are measured under H perpendicular to the film plane and no pulse current is driven through the nanowire. The schematic diagrams present the magnetization configuration in SAF structure.

Figure 7-2 (a) shows the dependence of M_n on N. The M_n decreases as N varies from 4 to 9, which is attributed to the difference in magnetization between the top and bottom [CoFe/Pd]$_N$ multilayers that reduces with N. The smallest M_n = 79 emu/cc is achieved when N = 9, which is due to the identical nominal total thickness (1.44 nm) of CoFe magnetic layer in the top and bottom CoFe/Pd multilayers. The exchange coupling strength J_{ex} between the two FM layers is expressed as $J_{ex} = H_{ex}M_s t$ [241], where M_s and t are saturation magnetization and overall thickness of the top FM layer, respectively. The J_{ex} as a function of N is shown in Fig. 7-2 (b). It is found that J_{ex} increases with N, which is mainly due to the $M_s t$ of top CoFe/Pd multilayers increases with N. In the following discussion, we shall focus on the current induced DW

displacement in the region that magnetization of top and bottom FM layers are aligned antiparallel as to study the effect of ECT on the DW motion.

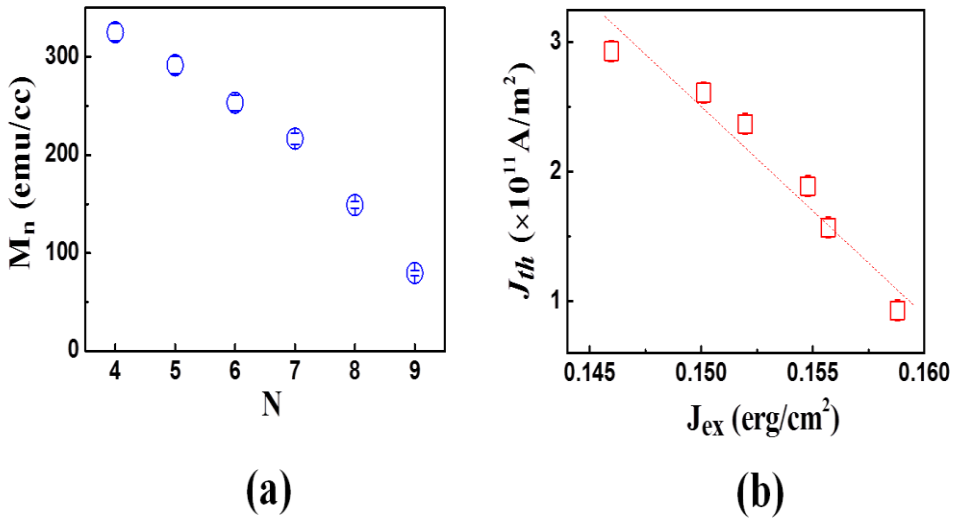

Fig. 7-2 The variation of (b) net magnetization M_n (= $|M_{s2} - M_{s1}|$) and (c) J_{ex} of $[CoFe/Pd]_8/CoFe/Ru/Pd/[CoFe/Pd]_N$ SAF structure as functions of N.

Prior to each measurement, DW was first nucleated at the joint between the triangular contact pad and nanowire (see MFM image in Fig. 7-3 (a)). The DW is pinned in the wire due to the intrinsic pinning strength after its nucleation [242]. Subsequently, a pulsed current is injected into the nanowire to induce the DW motion. The bottom of Fig. 7-3 (a) confirms the DW displacement after applying the pulsed current with current density $J > J_{th}$. The R_H is measured after each pulse to detect the DW motion [43]. Figure 7-3 (b) shows R_H as a function of the integrated pulse duration t with $J = +0.93\times10^{11}$ A/m^2, $+0.85\times10^{11}$ A/m^2 and -0.93×10^{11} A/m^2 under H = 0. The positive and negative signs of J denote the electrons are flowing along and opposite to the direction of DW motion, respectively. For $J = +0.93\times10^{11}$ A/m^2, a sudden jump of R_{Hall} in Fig. 7-3 (b) indicates that the DW driven by the current has passed through the Hall cross. As the pulse width is 5 ns for each pulse, the swtching

is occured when the pulse number equal to around 1800. The value of R_H changes around 0.2 Ω, which is almost the same as the variation of R_H for different orientation of $|M_{s1} - M_{s2}|$ in $[CoFe/Pd]_8/CoFe/Ru/Pd/[CoFe/Pd]_9$ SAF structure. This confirms that current induced DW motion occurs when magnetization of top and bottom FM layers are aligned antiparallel. On the other hand, no switching is observed when $J = -0.93\times10^{11}$ A/m^2, indicating that the DW moves in the direction of electron flow. Additionally, no switching of R_H is observed when the J is decreased to 0.85×10^{11} A/m^2. This suggests that the driving force generated by applied pulse current is not strong enough to drive the DW motion. Notably, the low threshold current density J_{th} for driving the DW motion is of importance to device applications.

Figure 7-3 (c) shows J_{th} of the $[CoFe/Pd]_8/CoFe/Ru/Pd/[CoFe/Pd]_N$ SAF structure nanowire as a function of N. All measurements were performed at zero field. The J_{th} decreases with N and a smallest $J_{th} = 9.3\times10^{10}$ A/m^2 is obtained for N = 9. This value is significantly lower in comparison with other perpendicularly Co-based-ferromagnetic multilayer nanowires, such as Co/Ni (J_{th}~$4-5\times10^{11}$ A/m^2) [42, 144], Co/Pt (J_{th}~1×10^{12} A/m^2) [77], CoFe/Pt (J_{th}~1.43×10^{12} A/m^2) [145] and CoFe/Pd (J_{th}~1.44×10^{11} A/m^2) [184]. To further understand the small value of J_{th} in our samples, we investigate the pinning effect on the J_{th} and measure the depinning field (H_{dep}) for SAF structure nanowires with different N. Figure 7-3 (d) shows the dependence of H_{dep} on N. The variation of H_{dep} is in the range of 40 to 70 mT and H_{dep} has a local maximum of 70 mT at N = 7. This excludes the possibility of the reduction of J_{th} due to the lowering of H_{dep}.

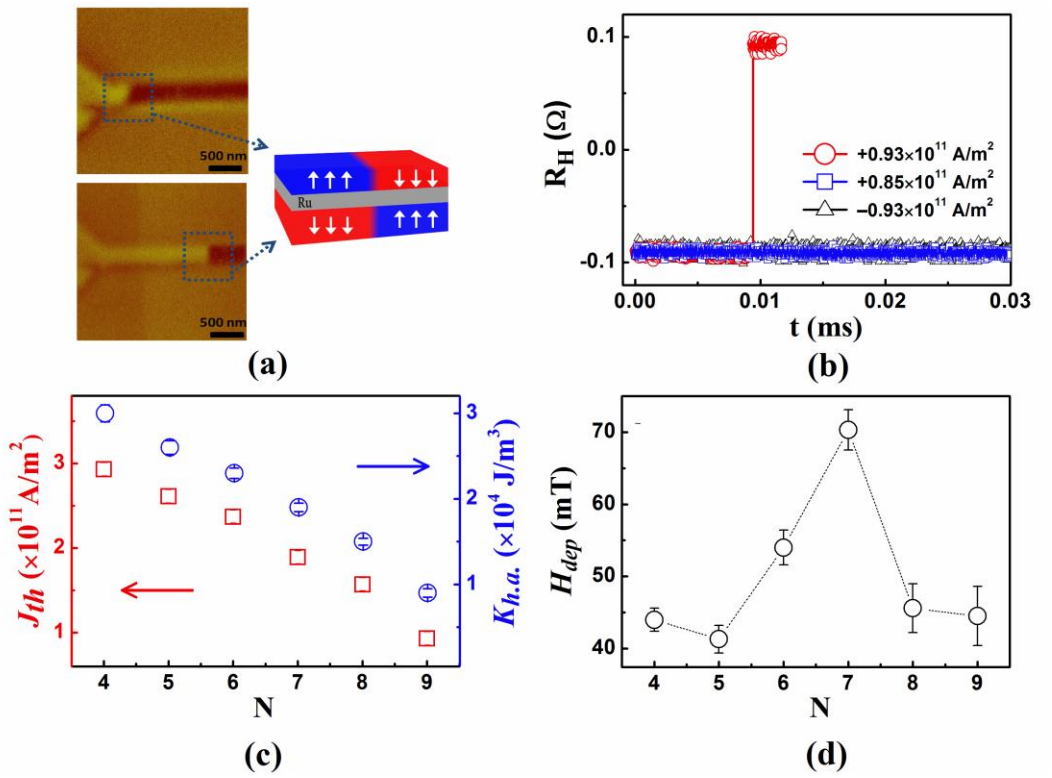

Fig. 7-3 The (a) The top MFM image shows that DW was formed by the local Oersted field of injected pulse current at the joint between contact pad and the nanowire in the $[CoFe(0.16)/Pd(0.22)]_8/CoFe(0.16)/Ru(0.8)/Pd(0.2)/[CoFe(0.16)/Pd(0.22)]_4$ SAF structure sample. The bottom MFM image shows that DW position is changed after flowing the pulsed current with the $J > J_{th}$ along the nanowire. A schematic diagram presents the domain and DW configuration in SAF structure. The red and blue regions represent areas that are oppositely magnetized; (b) The Hall resistance R_{Hall} as a function of integrated pulse duration t measured with driving pulse current densities $J = +0.93\times10^{11}$ A/m^2 (opened cycle), $+0.85\times10^{11}$ A/m^2 (opened rectangle) and -0.93×10^{11} A/m^2 (opened triangle) under zero magnetic field, respectively. The SAF structure of the nanowire device is $[CoFe(0.16)/Pd(0.22)]_8/CoFe(0.16)/Ru(0.8)/Pd(0.2)/[CoFe(0.16)/Pd(0.22)]_9$; (c) The threshold current density (J_{th}), hard axis anisotropy ($K_{h.a.}$) and (d) depinning field (H_{dep}) as functions of repeated number N for the $[CoFe/Pd]_8/CoFe/Ru/Pd/[CoFe/Pd]_N$ SAF structure nanowire.

Returning back to Fig. 7-3 (c), it shows that J_{th} dramatically decreases from 2.8×10^{11} to 9.3×10^{10} A/m^2 by a factor of 3 as N increases from 5 to 9. There are two important factors determining the J_{th}, which are the energy barrier and the driving force [31]. The DW has to overcome the energy barrier arising from the hard-axis anisotropy energy ($K_{h.a.}$) [33, 230] for motion [53]. Fig. 7-3 (c) shows that the $K_{h.a.}$ decreases with N in our SAF samples, which indicates the height of the energy barrier

decreases with N. On the other hand, previous simulation [243] and experimental [4, 244] results show that an exchange coupling torque (ECT) proportional to J_{ex} can be generated in a SAF structure. The ECT works as a driving force to help in depinning DWs in the two different layers [244, 245] and J_{th} can be decreased with reducing J_{ex}. As J_{ex} increases with N (changing from 5 to 9), the driving force increases with N. Therefore the dramatic reduction of J_{th} can be attributed to the reduction of the energy barrier and the increase in driving force.

7.1.3 Domain wall velocity in the SAF structure based nanowires

Figure 7-4 shows the averaged DW velocity (v) as a function of J for N ranging from 4 to 9. For a given sample, as J is increased from J_{th}, v increases linearly with J till J_w. Above J_w, the v slightly changes with J and subsequently increases linearly as J is further increased. The dependence of v on J can be explained by considering the *Walker breakdown* model.[59, 246] In this model, three regimes of the DW motion are predicted for Walker breakdown limit in SAF structure. Firstly, a steady-state DW motion occurs at low J, in which a linear dependence between v and J is expected. Then the v slightly decreases in the Walker breakdown regime of $J_w \leq J \leq J_p$, where J_w is defined as the Walker breakdown current density. The Walker breakdown limit originates from the demagnetization field that generates a torque on the magnetization. This torque has an opposite direction with the magnetization, resulting in the DW structure undergoes periodic configurations.[31] In the third region for high current density, v increases linearly as J is further increased above J_p and the DW motion

changes to a precessional regime.[31, 215, 247] The J_p is defined as the lowest J, above which the DW starts a processional motion. These predictions are in good agreement with our results of v dependent on J in the SAF structure nanowires.

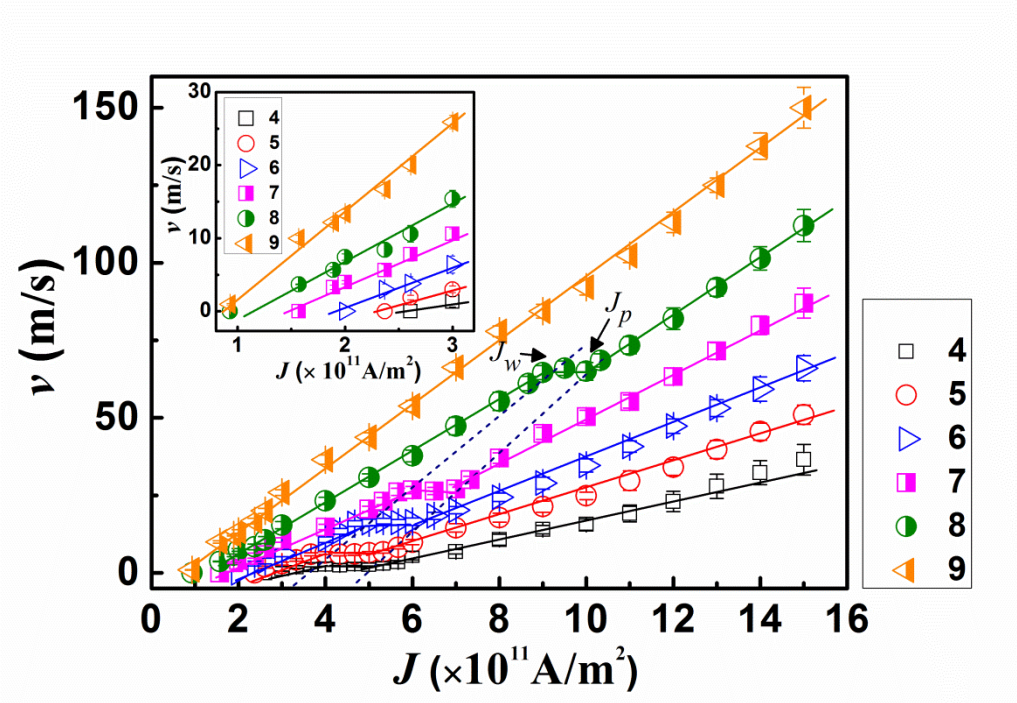

Fig. 7-4 The variation of the v as functions of J under zero applied field for the $[CoFe/Pd]_8/CoFe/Ru/Pd/[CoFe/Pd]_N$ SAF structure nanowires with N ranging from 4 to 9. The inset is the enlarged portion with J is in the range of 0.93×10^{11} A/m^2 to 3×10^{11} A/m^2. Each data point is the averaged value of 10 measurements at fixed current density. The error bars indicate the standard deviation.

In comparing the DW velocity among the different samples under the same driven current density, v increases with N and correspondingly the J_{ex} value. The maximum velocity v_{max} = 150 m/s in the SAF structure nanowire is significantly larger in comparison with our previous work using the same material but without SAF structure and other common Co-based multilayer nanowires, such as CoFe/Pd (v_{max} ~ 8 m/s) [43], Co/Ni (v_{max} ~ 60 m/s) [144] and CoFe/Pt (v_{max} ~ 1.5 m/s) [145]. These observations again agree with the prediction of ECT promote domain wall motion.

7.1.4 Discussion of exchange coupling torque (ECT) and spin orbit torque (SOT) in the SAF structure based nanowires

We note that ECT is dependent on the spin-orbit torque (SOT) originating from the adjacent heavy metal layer [244]. The SOTs will cause the magnetization of top and bottom FM in SAF to rotate to the spin accumulation direction (transverse to the length of nanowire). This will further result in an exchange field on the top and bottom FM, driving them back to their equilibrium state [244]. ECT is then generated through exchange field, which drive the DWs in the two different layers to move in the same direction. The SOTs could arise from spin Hall effect (SHE) and Rashba field as a consequence of breaking of structure inversion symmetry and the interfaces. It is expected that the heavy metal Ta [78, 84, 187], Pd and Ru [79] have nonzero spin Hall angle, which will generate the SOT due to SHE and influence the amplitude of ECT in Ta/Pd/$(CoFe/Pd)_8$/CoFe/Ru/Pd/$(CoFe/Pd)_N$/Ta structure samples. Thus, the SOT and ECT need to be further considered. Ru has smaller spin Hall conductivity compared with Ta, which may result in a smaller spin Hall effect for Ru than for Ta [79, 248]. Ru is inserted into the $(CoFe/Pd)_n$ multilayers to induce the antiferromagnetic coupling. In order to understand the major contribution to the ECT, we compare the v as function of J for three nanowire samples with different SAF structures, which are Ta(3)/Pd(3)/$(CoFe/Pd)_8$/CoFe/Ru/Pd/$(CoFe/Pd)_9$/Ta(3) (sample A), Ta(3)/Cu(3)/$(CoFe/Pd)_8$/CoFe/Ru/Pd/$(CoFe/Pd)_9$/Ta(3) (sample B) and Ta(3)/ Pd(3)/$(CoFe/Pd)_8$/CoFe/Ru/Pd/$(CoFe/Pd)_9$/Cu(3) (sample C) as shown in Fig. 7-5 (a). The Ta/Cu seed layer (Cu cap layer) is used to replace the Ta/Pd seed layer (top Ta

layer) to exclude the effect of SOT generated by Pd seed layer (top Ta layer). The Ta/Cu seed layer can also induce the $(CoFe/Pd)_n$ fcc (111) texture for high PMA [249]. The dependence of v on J for the sample A and B are almost the same, indicating the SHE of Pd seed layer has little effect on the DW motion due to the small spin Hall angle [250]. However, the v of sample C dramatically decreases as compared with sample A and B. This result indicates the high v is mainly dependent on the top Ta layer. The Ta has a large spin Hall angle and can generate strong SOT [78], which will directly influence the amplitude of ECT and the v value.

In order to quantify the SOT generated by Ta, the harmonic Hall voltage measurement with planar Hall effect correction [140, 141, 185-188] were performed for obtaining the effective fields along the longitudinal (ΔH_L) or the transverse (ΔH_T) direction for sample A and C, respectively. The dependence of effective fields ΔH_L and ΔH_T on J are plotted in Fig. 7-5 (b) and (c) for sample A and C, respectively. The magnitude of ΔH_L and ΔH_T increase linearly with J. We define the longitudinal (β_L) and transverse (β_T) SOT efficiencies [185, 188] as $\beta_{L(T)} = \Delta H_{L(T)}/J$ and the $\beta_{L(T)}$ values can be obtained from the slope. The β_L (β_T) is enhanced from 0.9 mT $cm^2/10^7$ A (0.2 mT $cm^2/10^7$ A) for sample C to 4 mT $cm^2/10^7$ A (0.7 mT $cm^2/10^7$ A) for sample A. These result indicate that although the thickness of top and bottom Ta layers is identical (3 nm), the top and bottom Ta layers generate non-identical SOTs on the SAF structure due to the Pd insertion in the bottom. The small SOT in sample C originates from the bottom Ta/Pd and the SAF structure [251]. It also shows that the top Ta layer produces much larger SOT than the bottom one. This structure

asymmetric leads to the enhancement of spin injection efficiency from the Ta to $(CoFe/Pd)_n$ multilayers based SAF structure [187].

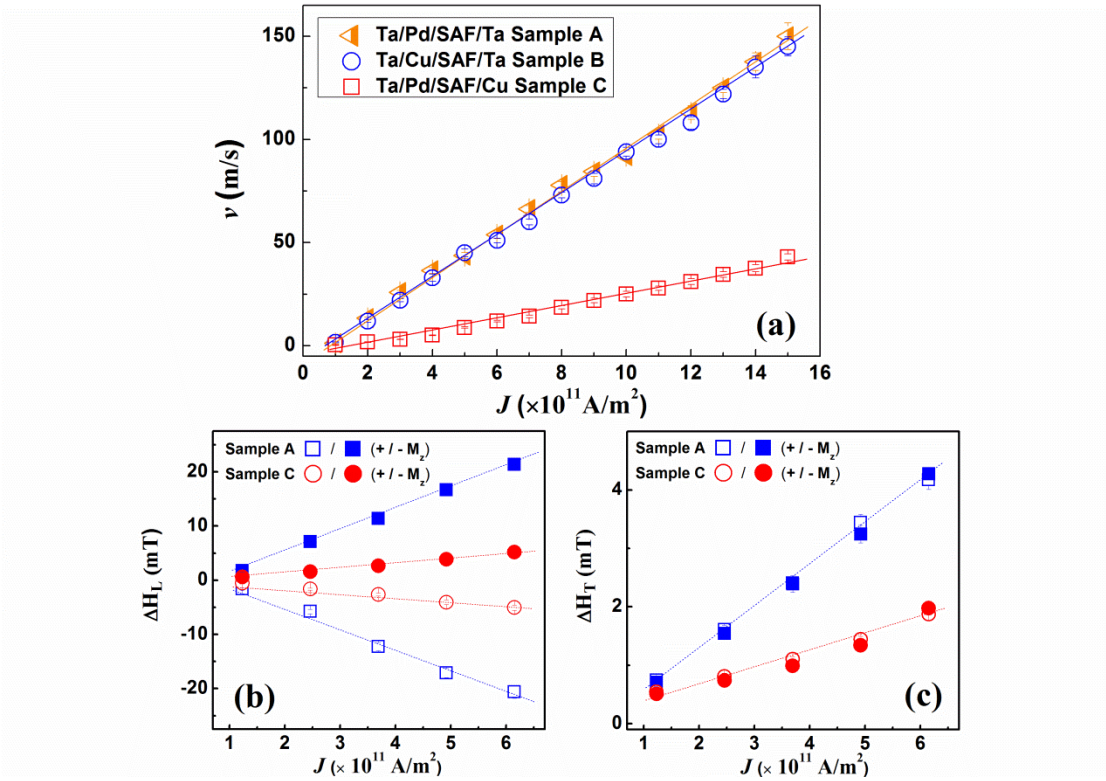

Fig. 7-5 (a) The v as functions of J for three nanowire sample A, B and C with different SAF structures; (b) and (c) show the dependence of ΔH_L and ΔH_T after planar Hall effect correction on J for sample A and C, respectively. The +/− M_z indicates the positive/negative initial magnetization states. The layered structures for sample A, B, and C are described in the text.

We note that v = 150 m/s at $J = 1.5\times10^{12}$A/m^2 achieved in this study is smaller than v ~ 380 m/s with identical J in Ref. [239]. One possible reason for the smaller v in our sample is that the SOT generated by the top Ta is smaller than Pt in Ref. [239]. Additionally, the SOT will be attenuated through the thickness of $(CoFe/Pd)_n$ multilayer based SAF structure. Our SAF structure thickness (~ 8 nm) is larger than in the Co/Ni/Co based SAF structure (~ 4 nm)[8], which will lead to smaller ECT and v.

7.2 Summary

In summary, we have systematically studied the threshold current density (J_{th}) and DW velocity (v) in ultrathin CoFe/Pd multilayer based SAF structure nanowires. A low J_{th} = 9.3×10^{10} A/m^2 and a maximum v = 150 m/s are achieved for the sample with J_{ex} of 0.0158 J/m^3. The small J_{th} and high v is due to an exchange coupling torque (ECT) generated in SAF structure. The amplitude of ECT is dependent on the spin-orbit torque from Ta and J_{ex}. The results suggest that SAF structure nanowires based on ultrathin [CoFe/Pd] multilayers with large spin orbit torque is beneficial for the spin-torque DW devices.

Chapter 8 Conclusions

8.1 Summary of results

The manipulation of magnetic domain wall (DW) motion using spin polarized current is important for scalable low-power devices in novel memory-storage applications, such as racetrack memory (RM). It is convenient to manipulate the magnetization of storage cell in RM using current-induced DW motion (CIDWM). Therefore, the high capacity density, small current density to drive the DW motion and enhanced current-driven DW dynamics are the primarily technological concerns for practical application. The PMA thin films are of great importance for RM because they possess higher magnetic storage density and lower driving current density for DW motion as compared with the in-plane magnetized materials. Taking advantage of strong interaction between the spin-polarized current and the local magnetization in PMA thin films is an essential method to produce robust current-induced torques.

We found that the CoFe/Pd multilayers, especially the multilayers with monoatomic thickness sublayers, have relatively high spin polarization (~ 60%), small domain wall width (~ 4.8 nm) and tunable saturation magnetization. In addition, high temperature post-annealing stability has been found in the CoFe/Pd superlattice-like multilayers, which is beneficial for the long time usage of the devices. Moreover, the noble metal Pd used in the multilayers can improve the magnetic property of films because of longer spin-diffusion length compared with Pt. These factors are favorable to reduce the threshold current density and improve the dynamics for DW motion.

In this thesis, we study the DW motion in a nanowire of CoFe/Pd multilayer with strong PMA. A small J_{th} of 1.44×10^{11} A/m^2 under magnetic field H of 750 Oe has been observed in the normal CoFe/Pd multilayer nanowire at room temperature measurements. The combination of non-adiabatic spin-transfer-torque and spin orbit torque generated by Ta layer is found to be the main contribution to the current induced DW motion.

To improve the DW efficiency and J_{th}, we study the DW motion in the nanowires patterned on CoFe/Pd superlattice-like multilayers. A smaller driving current density $J = 2.8\times10^{11}$ A/m^2 under H = 115 Oe has been achieved with a maximum DW velocity v = 8 m/s. A larger non-adiabatic coefficient is deduced from the CoFe/Pd superlattice-like multilayers.

Furthermore, the magnetization reversal and magnetic interlayer coupling in $(CoFe/Pd)_n$ superlattice-like based synthetic antiferromagnetic (SAF) structure have been studied. We have investigated the current induced DW motion in PMA nanowires patterned on the $(CoFe/Pd)_n$ superlattice-based synthetic antiferromagnetic (SAF) structure. A much smaller $J_{th} = 9.2\times10^{10}$ A/m^2 without bias H is observed and a maximum v = 150 m/s with $J = 1.5\times10^{12}$ A/m^2 for DW motion is achieved in the SAF structure nanowires. This is due to an exchange coupling torque (ECT) generated in SAF structure. The amplitude of ECT is dependent on the spin-orbit torque from Ta and J_{ex}. This indicates that ultrathin CoFe/Pd multilayer based SAF structure has better performances for future spin-torque devices.

8.2 Recommendation for future work

Besides the high efficiency of current-driven DW motion, there is renewed interest in domain wall based devices following the observation of spin Hall effect [78, 84] in multilayer films consisting of a nonmagnetic heavy metal and a ferromagnet. The effective spin Hall field acting on DWs has a similar symmetry as an out-of-plane driving magnetic field [148]. Therefore, it is possible to decrease the threshold current density required to move DWs by reducing the pinning field or defects in the nanowires. But the spin Hall effect is still under debate because the magnitude of spin Hall effect efficiency acquired is higher than the theoretical limit imposed by the efficiencies in two separate materials, Pt and Ta [75, 78, 84, 187]. At the same time, it is highly controversial that whether spin orbit torques (SOTs) induced by Rashba effect and spin Hall effect are pure material-dependent or interface-mediated in the spintronics community. The magnitude of SOT efficiencies has been reported with a lack of consistency. To effectively manipulate spin orbit torques for device applications, therefore, a solid understanding on spin orbit torques needs be established. Therefore, the spin Hall effect of Ta or Pt on the DW motion in the CoFe/Pd multilayers based nanowires need to be further understood in the following study.

References

[1] S. D. Sarma, American Scientist **89** (6), 516 (2001).

[2] S. Wolf, D. Awschalom, R. Buhrman, J. Daughton, S. Von Molnar, M. Roukes, A. Y. Chtchelkanova and D. Treger, Science **294** (5546), 1488-1495 (2001).

[3] J. Åkerman, Science **308** (5721), 508-510 (2005).

[4] S. Parkin and S.-H. Yang, Nature Nanotechnology **10** (3), 195-198 (2015).

[5] M. N. Baibich, J. M. Broto, A. Fert, F. N. Van Dau, F. Petroff, P. Etienne, G. Creuzet, A. Friederich and J. Chazelas, Physical Review Letters **61** (21), 2472 (1988).

[6] B. Dieny, V. S. Speriosu, S. S. Parkin, B. A. Gurney, D. R. Wilhoit and D. Mauri, Physical Review B **43** (1), 1297 (1991).

[7] S. Parkin, N. More and K. Roche, Physical Review Letters **64** (19), 2304 (1990).

[8] S. Parkin, X. Jiang, C. Kaiser, A. Panchula, K. Roche and M. Samant, Proceedings of the IEEE **91** (5), 661-680 (2003).

[9] T. Miyazaki, T. Yaoi and S. Ishio, Journal of Magnetism and Magnetic Materials **98** (1), L7-L9 (1991).

[10] W. Butler, X.-G. Zhang, T. Schulthess and J. MacLaren, Physical Review B **63** (5), 054416 (2001).

[11] D. Tang, P. Wang, V. Speriosu, S. Le and K. Kung, Magnetics, IEEE Transactions on **31** (6), 3206-3208 (1995).

[12] S. Parkin, K. Roche, M. Samant, P. Rice, R. Beyers, R. Scheuerlein, E. O'sullivan, S. Brown, J. Bucchigano and D. Abraham, Journal of Applied Physics **85** (8), 5828-5833 (1999).

[13] S. S. Parkin, M. Hayashi and L. Thomas, Science **320** (5873), 190-194 (2008).

[14] B. D. Cullity and C. D. Graham, *Introduction to magnetic materials*. (John Wiley & Sons, 2011).

[15] D. Claudio Gonzalez, PhD thesis, University of Southampton, 2008.

[16] S. S. Parkin, Patents US 7551469 B1,2009.

[17] L. Berger, Journal of Applied Physics **55** (6), 1954-1956 (1984).

[18] J. C. Slonczewski, Journal of Magnetism and Magnetic Materials **159** (1), L1-L7 (1996).

[19] M. Johnson, P. Bloemen, F. Den Broeder and J. De Vries, Reports on Progress in Physics **59** (11), 1409 (1996).

[20] P. Carcia, A. Meinhaldt and A. Suna, Applied Physics Letters **47** (2), 178-180 (1985).

[21] W. Zeper, F. Greidanus, P. Carcia and C. Fincher, Journal of Applied Physics **65** (12), 4971-4975 (1989).

[22] F. Den Broeder, D. Kuiper, A. Van de Mosselaer and W. Hoving, Physical Review Letters **60** (26), 2769 (1988).

[23] M. Sakurai, T. Takahata and I. Moritani, IEEE Translation Journal on Magnetics in Japan **7** (2), 176-182 (1992).
[24] M. De Santis, R. Baudoing-Savois, P. Dolle and M. Saint-Lager, Physical Review B **66** (8), 085412 (2002).
[25] R. Sbiaa, H. Meng and S. Piramanayagam, Physica Status Solidi **5** (12), 413-419 (2011).
[26] P. Xu, K. Xia, C. Gu, L. Tang, H. Yang and J. Li, Nature Nanotechnology **3** (2), 97-100 (2008).
[27] H. Meng and J.-P. Wang, Applied Physics Letters **88** (17), 2506 (2006).
[28] S. Mangin, D. Ravelosona, J. Katine, M. Carey, B. Terris and E. E. Fullerton, Nature Materials **5** (3), 210-215 (2006).
[29] T. Seki, S. Mitani, K. Yakushiji and K. Takanashi, Applied Physics Letters **88** (17), 172504 (2006).
[30] H. Yoda, T. Kishi, T. Nagase, M. Yoshikawa, K. Nishiyama, E. Kitagawa, T. Daibou, M. Amano, N. Shimomura and S. Takahashi, Current Applied Physics **10** (1), e87-e89 (2010).
[31] O. Boulle, G. Malinowski and M. Kläui, Materials Science and Engineering: R: Reports **72** (9), 159-187 (2011).
[32] S.-W. Jung, W. Kim, T.-D. Lee, K.-J. Lee and H.-W. Lee, Applied Physics Letters **92** (20), 202508 (2008).
[33] S. Fukami, T. Suzuki, N. Ohshima, K. Nagahara and N. Ishiwata, Journal of Applied Physics **103** (7), 07E718 (2008).
[34] D. Ravelosona, S. Mangin, J. Katine, E. E. Fullerton and B. Terris, Applied Physics Letters **90** (7), 072508 (2007).
[35] M. Johnson, J. De Vries, N. McGee, J. Aan de Stegge and F. Den Broeder, Physical Review Letters **69** (24), 3575 (1992).
[36] C. Burrowes, D. Ravelosona, C. Chappert, S. Mangin, E. E. Fullerton, J. Katine and B. Terris, Applied Physics Letters **93** (17), 172513 (2008).
[37] M. Hayashi, L. Thomas, R. Moriya, C. Rettner and S. S. Parkin, Science **320** (5873), 209-211 (2008).
[38] H. Fangohr, D. S. Chernyshenko, M. Franchin, T. Fischbacher and G. Meier, Physical Review B **84** (5), 054437 (2011).
[39] K.-J. Kim, J.-C. Lee, S.-B. Choe and K.-H. Shin, Applied Physics Letters **92** (19), 192509 (2008).
[40] J. Heinen, O. Boulle, K. Rousseau, G. Malinowski, M. Kläui, H. J. Swagten, B. Koopmans, C. Ulysse and G. Faini, Applied Physics Letters **96** (20), 202510 (2010).
[41] A. Barman, S. Wang, O. Hellwig, A. Berger, E. E. Fullerton and H. Schmidt, Journal of Applied Physics **101** (9), 9D102 (2007).
[42] T. Koyama, D. Chiba, K. Ueda, K. Kondou, H. Tanigawa, S. Fukami, T. Suzuki, N. Ohshima, N. Ishiwata and Y. Nakatani, Nature Materials **10** (3), 194-197 (2011).
[43] Z. Meng, S. He, J. Qiu, T. Zhou, G. Han and K.-L. Teo, Journal of Applied Physics **119** (8), 083905 (2016).

[44] Z. L. Meng, D. T. Ngo, M. Kumar, J. J. Qiu, G. C. Han and K. L. Teo, J. Phys. D: Appl. Phys. (accepted).
[45] Z. Meng, J. Qiu, G. Han and K. L. Teo, Journal of Applied Physics **118** (24), 243903 (2015).
[46] D.-T. Ngo, Z. Meng, T. Tahmasebi, X. Yu, E. Thoeng, L. Yeo, A. Rusydi, G. Han and K.-L. Teo, Journal of Magnetism and Magnetic Materials **350**, 42-46 (2014).
[47] A. Brataas, A. D. Kent and H. Ohno, Nature Materials **11** (5), 372-381 (2012).
[48] S. Emori, PhD thesis, Massachusetts Institute of Technology, 2013.
[49] N. L. Schryer and L. R. Walker, Journal of Applied Physics **45** (12), 5406-5421 (1974).
[50] G. Beach, M. Tsoi and J. Erskine, Journal of Magnetism and Magnetic Materials **320** (7), 1272-1281 (2008).
[51] G. S. Beach, C. Nistor, C. Knutson, M. Tsoi and J. L. Erskine, Nature Materials **4** (10), 741-744 (2005).
[52] L. Berger, Journal of Applied Physics **49** (3), 2156-2161 (1978).
[53] G. Tatara and H. Kohno, Physical Review Letters **92** (8), 086601 (2004).
[54] J. Xiao, A. Zangwill and M. Stiles, Physical Review B **73** (5), 054428 (2006).
[55] X. Waintal and M. Viret, EPL (Europhysics Letters) **65** (3), 427 (2004).
[56] Y. Ban and G. Tatara, Physical Review B **80** (18), 184406 (2009).
[57] A. Vanhaverbeke and M. Viret, Physical Review B **75** (2), 024411 (2007).
[58] J. Zhang, P. M. Levy, S. Zhang and V. Antropov, Physical Review Letters **93** (25), 256602 (2004).
[59] A. Thiaville, Y. Nakatani, J. Miltat and Y. Suzuki, EPL (Europhysics Letters) **69** (6), 990 (2005).
[60] Z. Li and S. Zhang, Physical Review B **70** (2), 024417 (2004).
[61] G. Beach, C. Knutson, M. Tsoi and J. Erskine, Journal of Magnetism and Magnetic Materials **310** (2), 2038-2040 (2007).
[62] S. Zhang and Z. Li, Physical Review Letters **93** (12), 127204 (2004).
[63] G. Beach, C. Knutson, C. Nistor, M. Tsoi and J. Erskine, Physical Review Letters **97** (5), 057203 (2006).
[64] E. Martinez, L. Lopez-Diaz, L. Torres, C. Tristan and O. Alejos, Physical Review B **75** (17), 174409 (2007).
[65] M. Lucassen, H. Van Driel, C. M. Smith and R. Duine, Physical Review B **79** (22), 224411 (2009).
[66] R. Duine, A. Núñez and A. MacDonald, Physical Review Letters **98** (5), 056605 (2007).
[67] G. Tatara, E. Saitoh, M. Ichimura and H. Kohno, Applid Physics Letters **86** (6), 232504 (2005).
[68] C. Schieback, D. Hinzke, M. Kläui, U. Nowak and P. Nielaba, Physical Review B **80** (21), 214403 (2009).
[69] D. Garanin, Physical Review B **55** (5), 3050 (1997).
[70] S. Lemerle, J. Ferré, C. Chappert, V. Mathet, T. Giamarchi and P. Le Doussal, Physical Review Letters **80** (4), 849 (1998).

[71] F. Cayssol, D. Ravelosona, C. Chappert, J. Ferré and J. Jamet, Physical Review Letters **92** (10), 107202 (2004).
[72] R. Duine and C. M. Smith, Physical Review B **77** (9), 094434 (2008).
[73] I. M. Miron, T. Moore, H. Szambolics, L. D. Buda-Prejbeanu, S. Auffret, B. Rodmacq, S. Pizzini, J. Vogel, M. Bonfim and A. Schuhl, Nature Materials **10** (6), 419-423 (2011).
[74] I. M. Miron, K. Garello, G. Gaudin, P.-J. Zermatten, M. V. Costache, S. Auffret, S. Bandiera, B. Rodmacq, A. Schuhl and P. Gambardella, Nature **476** (7359), 189-193 (2011).
[75] L. Liu, O. Lee, T. Gudmundsen, D. Ralph and R. Buhrman, Physical Review Letters **109** (9), 096602 (2012).
[76] X. Fan, H. Celik, J. Wu, C. Ni, K.-J. Lee, V. O. Lorenz and J. Q. Xiao, Nature Communications **5** (2014).
[77] I. M. Miron, G. Gaudin, S. Auffret, B. Rodmacq, A. Schuhl, S. Pizzini, J. Vogel and P. Gambardella, Nature Materials **9** (3), 230-234 (2010).
[78] L. Liu, C.-F. Pai, Y. Li, H. Tseng, D. Ralph and R. Buhrman, Science **336** (6081), 555-558 (2012).
[79] A. Hoffmann, IEEE Transactions on Magnetics **49** (10), 5172-5193 (2013).
[80] M. D'yakonov and V. Perel, Soviet Journal of Experimental and Theoretical Physics Letters **13**, 467 (1971).
[81] J. Hirsch, Physical Review Letters **83** (9), 1834 (1999).
[82] Y. Kato, R. Myers, A. Gossard and D. Awschalom, Science **306** (5703), 1910-1913 (2004).
[83] K.-S. Ryu, L. Thomas, S.-H. Yang and S. Parkin, Nature Nanotechnology **8** (7), 527-533 (2013).
[84] S. Emori, U. Bauer, S.-M. Ahn, E. Martinez and G. S. Beach, Nature Materials **12** (7), 611-616 (2013).
[85] A. Crépieux and C. Lacroix, Journal of Magnetism and Magnetic Materials **182** (3), 341-349 (1998).
[86] E. H. Hall, American Journal of Mathematics **2** (3), 287-292 (1879).
[87] E. Hall, Philos Mag **12**, 157-172 (1881).
[88] N. Nagaosa, J. Sinova, S. Onoda, A. MacDonald and N. Ong, Reviews of Modern Physics **82** (2), 1539 (2010).
[89] D. Ravelosona, D. Lacour, J. Katine, B. Terris and C. Chappert, Physical Review Letters **95** (11), 117203 (2005).
[90] C. Hurd, *The Hall effect in metals and alloys*. (Springer Science & Business Media, 2012).
[91] M. Van Kooten, S. De Haan, J. Lodder and T. J. Popma, Journal of Applied Physics **75** (10), 5508-5510 (1994).
[92] J. Wunderlich, D. Ravelosona, C. Chappert, F. Cayssol, V. Mathet, J. Ferre, J. Jamet and A. Thiaville, Magnetics, IEEE Transactions on **37** (4), 2104-2107 (2001).
[93] I. Miron, P.-J. Zermatten, G. Gaudin, S. Auffret, B. Rodmacq and A. Schuhl, Physical Review Letters **102** (13), 137202 (2009).

[94] A. Yamaguchi, T. Ono, S. Nasu, K. Miyake, K. Mibu and T. Shinjo, Physical Review Letters **92** (7), 077205 (2004).
[95] A. Yamaguchi, S. Nasu, H. Tanigawa, T. Ono, K. Miyake, K. Mibu and T. Shinjo, Applied Physics Letters **86** (1), 012511 (2005).
[96] M. Yamanouchi, D. Chiba, F. Matsukura, T. Dietl and H. Ohno, Physical Review Letters **96** (9), 096601 (2006).
[97] H. Tanigawa, K. Kondou, T. Koyama, K. Nakano, S. Kasai, N. Ohshima, S. Fukami, N. Ishiwata and T. Ono, Applied Physics Express **1** (1), 011301 (2008).
[98] T. Koyama, G. Yamada, H. Tanigawa, S. Kasai, N. Ohshima, S. Fukami, N. Ishiwata, Y. Nakatani and T. Ono, Applied Physics Express **1** (10), 101303 (2008).
[99] T. Schrefl, J. Fidler, K. Kirk and J. Chapman, Journal of Magnetism and Magnetic Materials **175** (1), 193-204 (1997).
[100] H. Hopster and H. P. Oepen, *Magnetic microscopy of nanostructures*. (Springer Science & Business Media, 2006).
[101] T. Kasama, R. E. Dunin-Borkowski and W. Eerenstein, Physical Review B **73** (10), 104432 (2006).
[102] C. Brownlie, S. McVitie, J. Chapman and C. Wilkinson, Journal of Applied Physics **100** (3), 033902 (2006).
[103] M. Kläui, H. Ehrke, U. Rüdiger, T. Kasama, R. E. Dunin-Borkowski, D. Backes, L. J. Heyderman, C. A. Vaz, J. A. C. Bland and G. Faini, Applied Physics Letters **87** (10), 102509 (2005).
[104] D. McGrouther, S. McVitie, J. Chapman and A. Gentils, Applied Physics Letters **91** (2), 022506 (2007).
[105] M. Mansuripur, *The physical principles of magneto-optical recording*. (Cambridge University Press, 1998).
[106] C. Chappert, H. Bernas, J. Ferré, V. Kottler, J.-P. Jamet, Y. Chen, E. Cambril, T. Devolder, F. Rousseaux and V. Mathet, Science **280** (5371), 1919-1922 (1998).
[107] M. Yamanouchi, D. Chiba, F. Matsukura and H. Ohno, Nature **428** (6982), 539-542 (2004).
[108] T. Devolder, C. Chappert, Y. Chen, E. Cambril, H. Bernas, J. Jamet and J. Ferré, Applied Physics Letters **74** (22), 3383-3385 (1999).
[109] C. Nistor, G. S. Beach and J. L. Erskine, Review of Scientific Instruments **77** (10), 103901 (2006).
[110] Z. Li and S. Zhang, Physical Review Letters **92** (20), 207203 (2004).
[111] L. Heyne, J. Rhensius, Y.-J. Cho, D. Bedau, S. Krzyk, C. Dette, H. Körner, J. Fischer, M. Laufenberg and D. Backes, Physical Review B **80** (18), 184405 (2009).
[112] T. A. Moore, M. Kläui, L. Heyne, P. Möhrke, D. Backes, J. Rhensius, U. Rüdiger, L. J. Heyderman, J.-U. Thiele and G. Woltersdorf, Physical Review B **80** (13), 132403 (2009).

[113] L. Heyne, J. Rhensius, A. Bisig, S. Krzyk, P. Punke, M. Kläui, L. J. Heyderman, L. Le Guyader and F. Nolting, Applied Physics Letters **96** (3), 032504 (2010).
[114] G. Meier, M. Bolte, R. Eiselt, B. Krüger, D.-H. Kim and P. Fischer, Physical Review Letters **98** (18), 187202 (2007).
[115] H. Kronmüller and S. S. Parkin, *Handbook of magnetism and advanced magnetic materials*. (John Wiley & Sons, 2007).
[116] M. Kläui, C. A. Vaz, J. A. C. Bland, W. Wernsdorfer, G. Faini, E. Cambril, L. J. Heyderman, F. Nolting and U. Rüdiger, Physical Review Letters **94** (10), 106601 (2005).
[117] M. Hayashi, L. Thomas, C. Rettner, R. Moriya, Y. B. Bazaliy and S. S. Parkin, Physical Review Letters **98** (3), 037204 (2007).
[118] H. Kronmüller and S. Parkin, Spintronics and Magnetoelectronics **5** (2008).
[119] M. Tsoi, R. Fontana and S. Parkin, Applied Physics Letters **83** (13), 2617-2619 (2003).
[120] P. Ho, J. Zhang, J. A. Currivan-Incorvia, D. C. Bono and C. Ross, Magnetics Letters, IEEE **6**, 1-4 (2015).
[121] A. D. Kent, Nature Materials **9** (9), 699-700 (2010).
[122] M. Kläui, P.-O. Jubert, R. Allenspach, A. Bischof, J. A. C. Bland, G. Faini, U. Rüdiger, C. A. Vaz, L. Vila and C. Vouille, Physical Review Letters **95** (2), 026601 (2005).
[123] L. Heyne, M. Kläui, D. Backes, T. Moore, S. Krzyk, U. Rüdiger, L. J. Heyderman, A. F. Rodríguez, F. Nolting and T. O. Mentes, Physical Review Letters **100** (6), 066603 (2008).
[124] L. S. E. Alvarez, K.-Y. Wang, S. Lepadatu, S. Landi, S. J. Bending and C. Marrows, Physical Review Letters **104** (13), 137205 (2010).
[125] N. Watanabe and H. Awano, Japanese Journal of Applied Physics **51** (9R), 093002 (2012).
[126] K. Ikeda and H. Awano, Applied Physics Express **4** (9), 093002 (2011).
[127] C. Leroux, M. Cadeville, V. Pierron-Bohnes, G. Inden and F. Hinz, Journal of Physics F: Metal Physics **18** (9), 2033 (1988).
[128] J. Ferré, in *Spin Dynamics in Confined Magnetic Structures I* (Springer, 2002), pp. 127-165.
[129] J. Hong, S. Sankar, A. Berkowitz and W. Egelhoff, Journal of Magnetism and Magnetic Materials **285** (3), 359-366 (2005).
[130] T. Thomson, G. Hu and B. Terris, Physical Review Letters **96** (25), 257204 (2006).
[131] P. Metaxas, J. Jamet, A. Mougin, M. Cormier, J. Ferré, V. Baltz, B. Rodmacq, B. Dieny and R. Stamps, Physical Review Letters **99** (21), 217208 (2007).
[132] F. Garcia-Sanchez, H. Szambolics, A. Mihai, L. Vila, A. Marty, J.-P. Attané, J.-C. Toussaint and L. Buda-Prejbeanu, Physical Review B **81** (13), 134408 (2010).

[133] O. Boulle, J. Kimling, P. Warnicke, M. Kläui, U. Rüdiger, G. Malinowski, H. J. Swagten, B. Koopmans, C. Ulysse and G. Faini, Physical Review Letters **101** (21), 216601 (2008).
[134] S. Fukami, Y. Nakatani, T. Suzuki, K. Nagahara, N. Ohshima and N. Ishiwata, Applied Physics Letters **95** (23), 2504 (2009).
[135] M. Feigenson, J. W. Reiner and L. Klein, Journal of Applied Physics **103** (7), 7E741 (2008).
[136] M. Laufenberg, W. Bührer, D. Bedau, P.-E. Melchy, M. Kläui, L. Vila, G. Faini, C. A. Vaz, J. A. C. Bland and U. Rüdiger, Physical Review Letters **97** (4), 046602 (2006).
[137] C. Burrowes, A. Mihai, D. Ravelosona, J.-V. Kim, C. Chappert, L. Vila, A. Marty, Y. Samson, F. Garcia-Sanchez and L. Buda-Prejbeanu, Nature Physics **6** (1), 17-21 (2010).
[138] M. Feigenson, J. W. Reiner and L. Klein, Physical Review Letters **98** (24), 247204 (2007).
[139] U. H. Pi, K. W. Kim, J. Y. Bae, S. C. Lee, Y. J. Cho, K. S. Kim and S. Seo, Applied Physics Letters **97** (16), 162507 (2010).
[140] J. Kim, J. Sinha, M. Hayashi, M. Yamanouchi, S. Fukami, T. Suzuki, S. Mitani and H. Ohno, Nature Materials **12** (3), 240-245 (2013).
[141] K. Garello, I. M. Miron, C. O. Avci, F. Freimuth, Y. Mokrousov, S. Blügel, S. Auffret, O. Boulle, G. Gaudin and P. Gambardella, Nature Nanotechnology **8** (8), 587-593 (2013).
[142] P. Haazen, E. Murè, J. Franken, R. Lavrijsen, H. Swagten and B. Koopmans, Nature Materials **12** (4), 299-303 (2013).
[143] C. Hassel, M. Brands, F. Lo, A. Wieck and G. Dumpich, Physical Review Letters **97** (22), 226805 (2006).
[144]H. Tanigawa, T. Suzuki, S. Fukami, K. Suemitsu, N. Ohshima and E. Kariyada, Applied Physics Letters **102** (15), 152410 (2013).
[145] K.-J. Kim, J.-C. Lee, Y. J. Cho, C.-W. Lee, K.-H. Shin, S. Seo, K.-J. Lee, H.-W. Lee and S.-B. Choe, Magnetics, IEEE Transactions on **45** (10), 3773-3775 (2009).
[146] S. Fukami, T. Suzuki, Y. Nakatani, N. Ishiwata, M. Yamanouchi, S. Ikeda, N. Kasai and H. Ohno, Applied Physics Letters **98** (8), 082504 (2011).
[147] T. A. Moore, I. Miron, G. Gaudin, G. Serret, S. Auffret, B. Rodmacq, A. Schuhl, S. Pizzini, J. Vogel and M. Bonfim, Applied Physics Letters **93** (26), 262504 (2008).
[148] R. Lavrijsen, P. Haazen, E. Mure, J. Franken, J. Kohlhepp, H. Swagten and B. Koopmans, Applied Physics Letters **100** (26), 262408 (2012).
[149] D. Bang, J. Yu, X. Qiu, Y. Wang, H. Awano, A. Manchon and H. Yang, Physical Review B **93** (17), 174424 (2016).
[150] S. Li, H. Nakamura, T. Kanazawa, X. Liu and A. Morisako, Magnetics, IEEE Transactions on **46** (6), 1695-1698 (2010).

[151] J.-C. Lee, K.-J. Kim, J. Ryu, K.-W. Moon, S.-J. Yun, G.-H. Gim, K.-S. Lee, K.-H. Shin, H.-W. Lee and S.-B. Choe, arXiv preprint arXiv:1006.1216 (2010).
[152] A. Brataas, Nature Nanotechnology **8** (7), 485-486 (2013).
[153] D. Bang and H. Awano, Japanese Journal of Applied Physics **52** (12R), 123001 (2013).
[154] D. E. Harrison Jr, Physical Review B **102** (6), 1473 (1956).
[155] R. Behrisch and K. Wittmaack, *Sputtering by particle bombardment*. (Springer Berlin, 1983).
[156] D. Maurya, A. Sardarinejad and K. Alameh, Coatings **4** (4), 756-771 (2014).
[157] http://archive.cnx.org/contents/517f8f37-f619-4408-a8b4-2ef8a53e8c29@2/wide-angle-x-ray-diffraction-studies-of-liquid-crystals.
[158] B. L. Dutrow and C. M. Clark, http://serc.carleton.edu/research_education/geochemsheets/techniques/XRD.html.
[159] http://www.slideshare.net/chem_engine/x-ray-diffraction-39221133.
[160] http://education.mrsec.wisc.edu/nanoquest/afm/.
[161] http://blog.brukerafmprobes.com/guide-to-spm-and-afm-modes/magnetic-force-microscopy-mfm/.
[162] B. Fultz and J. M. Howe, *Transmission electron microscopy and diffractometry of materials*. (Springer Science & Business Media, 2012).
[163] M. Farle, Reports on Progress in Physics **61** (7), 755 (1998).
[164] X. Yu, O. Wilhelmi, H. O. Moser, S. V. Vidyaraj, X. Gao, A. T. Wee, T. Nyunt, H. Qian and H. Zheng, Journal of Electron Spectroscopy and Related Phenomena **144**, 1031-1034 (2005).
[165] http:/llgmicro.home.mindspring.com/.
[166] S. Piramanayagam, M. Liau, J. Shi and B. Lim, Journal of Magnetism and Magnetic Materials **303** (2), e152-e155 (2006).
[167] S. Okamoto, O. Kitakami and Y. Shimada, Magnetics, IEEE Transactions on **35** (5), 3031-3033 (1999).
[168] M. Bersweiler, K. Dumesnil, D. Lacour and M. Hehn, Journal of Physics: Condensed Matter **28** (33), 336005 (2016).
[169] L. Li, Y. Lu, Z. Liu, Y. Lv, Y. Zhang, S. Liu, C. Hao and W. Lv, Journal of Magnetism and Magnetic Materials **325**, 117-121 (2013).
[170] R. Shull, Y. Iunin, Y. Kabanov, V. Nikitenko, O. Skryabina and C. Chien, Journal of Applied Physics **113** (17), 17C101 (2013).
[171] M. Yamanouchi, A. Jander, P. Dhagat, S. Ikeda, F. Matsukura and H. Ohno, Magnetics Letters, IEEE **2**, 3000304-3000304 (2011).
[172] C.-X. Ji, L. Feng, Y. A. Chang, J. J. Yang and M. Rzchowski, Applied Physics Letters **92** (2) (2008).
[173] P. Aitchison, J. Chapman, V. Gehanno, I. S. Weir, M. Scheinfein, S. McVitie and A. Marty, Journal of Magnetism and Magnetic Materials **223** (2), 138-146 (2001).
[174] C. Marrows, Advances in Physics **54** (8), 585-713 (2005).

[175] M. Viret, Y. Samson, P. Warin, A. Marty, F. Ott, E. Sønderg ård, O. Klein and C. Fermon, Physical Review Letters **85** (18), 3962 (2000).
[176] J. M. Coey, *Magnetism and magnetic materials*. (Cambridge University Press, 2010).
[177] A. Rusydi, S. Dhar, A. R. Barman, D.-C. Qi, M. Motapothula, J. Yi, I. Santoso, Y. Feng, K. Yang and Y. Dai, Philosophical Transactions of the Royal Society of London A: Mathematical, Physical and Engineering Sciences **370** (1977), 4927-4943 (2012).
[178] B. Thole, P. Carra, F. Sette and G. van der Laan, Physical Review Letters **68** (12), 1943 (1992).
[179] P. Carra, B. Thole, M. Altarelli and X. Wang, Physical Review Letters **70** (5), 694 (1993).
[180] P. Krüger, presented at the Journal of Physics: Conference Series, 2009 (unpublished).
[181] R. Soulen, J. Byers, M. Osofsky, B. Nadgorny, T. Ambrose, S. Cheng, P. R. Broussard, C. Tanaka, J. Nowak and J. Moodera, Science **282** (5386), 85-88 (1998).
[182] A. Rajanikanth, S. Kasai, N. Ohshima and K. Hono, Applied Physics Letters **97** (2), 022505 (2010).
[183] D. Smith, V. Parekh, E. Chunsheng, S. Zhang, W. Donner, T. R. Lee, S. Khizroev and D. Litvinov, Journal of Applied Physics **103** (2), 23920-23920 (2008).
[184] Z. Meng, M. Kumar, J. Qiu, G. Han and K.-L. Teo, Journal of Physics D: Applied Physics **47** (34), 345001 (2014).
[185] M. Jamali, K. Narayanapillai, X. Qiu, L. M. Loong, A. Manchon and H. Yang, Physical Review Letters **111** (24), 246602 (2013).
[186] M. Hayashi, J. Kim, M. Yamanouchi and H. Ohno, Physical Review B **89** (14), 144425 (2014).
[187] S. Woo, M. Mann, A. J. Tan, L. Caretta and G. S. Beach, Applied Physics Letters **105** (21), 212404 (2014).
[188] K.-F. Huang, D.-S. Wang, H.-H. Lin and C.-H. Lai, Applied Physics Letters **107** (23), 232407 (2015).
[189] A. Khvalkovskiy, V. Cros, D. Apalkov, V. Nikitin, M. Krounbi, K. Zvezdin, A. Anane, J. Grollier and A. Fert, Physical Review B **87** (2), 020402 (2013).
[190] S. Sumi, Y. Kusumoto, Y. Teragaki, K. Torazawa, S. Tsunashima and S. Uchiyama, Journal of Applied Physics **73** (10), 6835-6837 (1993).
[191] G. Bertero and R. Sinclair, Journal of Magnetism and Magnetic Materials **134** (1), 173-184 (1994).
[192] K. Yakushiji, T. Saruya, H. Kubota, A. Fukushima, T. Nagahama, S. Yuasa and K. Ando, Appl. Phys. Lett. **97** (23), 232508 (2010).
[193] J. Foros, G. Woltersdorf, B. Heinrich and A. Brataas, Journal of Applied Physics **97** (10, Pa), 10A714 (2005).
[194] K. Kondou, H. Sukegawa, S. Mitani, K. Tsukagoshi and S. Kasai, Applied Physics Express **5** (7), 073002 (2012).

[195] S. Girod, M. Gottwald, S. Andrieu, S. Mangin, J. McCord, E. E. Fullerton, J.-M. Beaujour, B. Krishnatreya and A. Kent, Applied Physics Letters **94** (26), 262504 (2009).
[196] M. Shiga, State Comunication **10**, 1233 (1972).
[197] S. M. Foiles, M. I. Baskes and M. S. Daw, Phys. Rev. B **33** (12), 7983-7991 (1986).
[198] Z. Meng, M. Kumar, J. Qiu, G. Han, K. L. Teo and D.-T. Ngo, arXiv preprint arXiv:1405.7164 (2014).
[199] S. Fukami, T. Suzuki, Y. Nakatani, N. Ishiwata, M. Yamanouchi, S. Ikeda, N. Kasai and H. Ohno, Appl. Phys. Lett. **98** (8), 082504 (2011).
[200] B. N. Engel, C. D. England, R. A. Van Leeuwen, M. H. Wiedmann and C. M. Falco, Physical Review Letters **67** (14), 1910 (1991).
[201] H. Yamane, Y. Maeno and M. Kobayashi, Applied Physics Letters **62** (13), 1562-1564 (1993).
[202] M. Gottwald, K. Lee, J. Kan, B. Ocker, J. Wrona, S. Tibus, J. Langer, S. Kang and E. Fullerton, Applied Physics Letters **102** (5), 052405 (2013).
[203]C. J. Aas, L. Szunyogh, R. F. L. Evans and R. W. Chantrell, Journal of Physics: Condensed Matter **25** (29), 296006 (2013).
[204] Y. Zhu, Z. Zhang, B. Ma and Q. Jin, Journal of Applied Physics **111** (7), 07C106 (2012).
[205] F. Den Broeder, W. Hoving and P. Bloemen, Journal of Magnetism and Magnetic Materials **93**, 562-570 (1991).
[206] G. Daalderop, P. Kelly and M. Schuurmans, Physical Review B **42** (11), 7270 (1990).
[207] S. Fukami, H. Sato, M. Yamanouchi, S. Ikeda and H. Ohno, Applied Physics Express **6** (7), 073010 (2013).
[208] J. Feng and J. Coey, presented at the Journal of Physics: Conference Series, 2011 (unpublished).
[209] S. Y. Jang, C. Y. You, S. H. Lim and S. R. Lee, J. Appl. Phys. **109** (1), 013901 (2011).
[210] A. S. H. Rozatian, C. H. Marrows, T. P. A. Hase and B. K. Tanner, J. Phys.: Condens. Matter. **17** (25), 3759-3770 (2005).
[211] S. N. Piramanayagam, M. J. Liau, J. Z. Shi and B. C. Lim, IEEE Trans. Magn. **42** (10), 2369-2371 (2006).
[212] Y. Hodumi, J. Shi and Y. Nakamura, Applied Physics Letters **90** (21), 212506 (2007).
[213] L. Thomas and S. Parkin, Handbook of Magnetism and Advanced Magnetic Materials (2007).
[214] A. Naeemi and J. D. Meindl, Electron Device Letters, IEEE **28** (2), 135-138 (2007).
[215] J.-P. Adam, N. Vernier, J. Ferré, A. Thiaville, V. Jeudy, A. Lemaître, L. Thevenard and G. Faini, Physical Review B **80** (19), 193204 (2009).

[216] M. Eltschka, M. Woetzel, J. Rhensius, S. Krzyk, U. Nowak, M. Kläui, T. Kasama, R. E. Dunin-Borkowski, L. J. Heyderman and H. van Driel, Physical Review Letters **105** (5), 056601 (2010).
[217] A. Mougin, M. Cormier, J. Adam, P. Metaxas and J. Ferré, EPL (Europhysics Letters) **78** (5), 57007 (2007).
[218] S. Chen, Y. Xiao, W. Xie, Z. Zhang, B. Ma and Q. Jin, Applied Physics Letters **105** (26), 262403 (2014).
[219] Y. Xiao, S. Chen, Z. Zhang, B. Ma and Q. Jin, Journal of Applied Physics **113** (17), 17A325 (2013).
[220] G. Han, M. Tran, C. H. Sim, J. C. Wang, K. Eason, S. Ter Lim and A. Huang, Journal of Applied Physics **117** (17), 17B515 (2015).
[221] H. Gan, R. Malmhall, Z. Wang, B. K. Yen, J. Zhang, X. Wang, Y. Zhou, X. Hao, D. Jung and K. Satoh, Applied Physics Letters **105** (19), 192403 (2014).
[222] M. P. R. Sabino, M. Tran, C. H. Sim, Y. J. Feng and K. Eason, Journal of Applied Physics **115** (17), 17C512 (2014).
[223] R. Sbiaa, S. Piramanayagam and R. Law, Applied Physics Letters **95** (24), 2502 (2009).
[224] M. Ranjbar, R. Sbiaa, R. Dumas, J. Åkerman and S. Piramanayagam, Journal of Applied Physics **115** (17), 17C103 (2014).
[225] G. Han, C. Wang, J. Qiu, P. Luo and V. Ko, Applied Physics Letters **98** (19), 192502 (2011).
[226] J. Moritz, F. Garcia, J. Toussaint, B. Dieny and J. Nozieres, EPL (Europhysics Letters) **65** (1), 123 (2004).
[227] B. Rodmacq, V. Baltz and B. Dieny, Physical Review B **73** (9), 092405 (2006).
[228] O. Hellwig, A. Berger and E. E. Fullerton, Journal of Magnetism and Magnetic Materials **290**, 1-7 (2005).
[229] J. Zhao, Y. Wang, Y. Liu, X. Han and Z. Zhang, Journal of Applied Physics **104** (2), 023911-023911-023914 (2008).
[230] S. Bandiera, R. Sousa, S. Auffret, B. Rodmacq and B. Dieny, Applied Physics Letters **101** (7), 072410 (2012).
[231] S. Parkin and D. Mauri, Physical Review B **44** (13), 7131 (1991).
[232] E. Girt and H. J. Richter, Magnetics, IEEE Transactions on **39** (5), 2306-2310 (2003).
[233] F. Himpsel, K. Christmann, P. Heimann and D. Eastman, Physical Review B **23** (6), 2548 (1981).
[234] N. Persat and A. Dinia, Physical Review B **56** (5), 2676 (1997).
[235] R. Sbiaa, I. Al-Omari, P. Kharel, M. Ranjbar, D. Sellmyer, J. Åkerman and S. Piramanayagam, Journal of Applied Physics **118** (6), 063902 (2015).
[236] R. Dormaier, Q. Zhang, Y.-C. Chou, M. Lange, J. Yang, A. Oki and S. Mohney, Journal of Vacuum Science & Technology B **27** (5), 2145-2152 (2009).
[237] P. Bruno, Physical Review B **52** (1), 411 (1995).

[238] C.-L. Lee, J. A. Bain, S. Chu and M. E. McHenry, Journal of Applied Physics **91** (10), 7113-7115 (2002).
[239] D. IONESCU and M. KOVACI. "Improving the data storage performances with layered nanowires for synthetic antiferromagnetic racetrack memories."
[240] Y. Xiao, Z. Zhang, B. Ma, Q. Jin and Y. Liu, Applied Physics Letters **104** (7), 072403 (2014).
[241] S. S. Parkin, Physical Review Letters **67** (25), 3598 (1991).
[242] J. H. Franken, M. Hoeijmakers, R. Lavrijsen and H. J. Swagten, Journal of Physics: Condensed Matter **24** (2), 024216 (2011).
[243] H. Saarikoski, H. Kohno, C. H. Marrows and G. Tatara, Physical Review B **90** (9), 094411 (2014).
[244] S.-H. Yang, K.-S. Ryu and S. Parkin, Nature Nanotechnology **10** (3), 221-226 (2015).
[245] O. Gomonay, T. Jungwirth and J. Sinova, Physical Review Letters **117** (1), 017202 (2016).
[246] M. Kuteifan, M. Lubarda, S. Fu, R. Chang, M. Escobar, S. Mangin, E. Fullerton and V. Lomakin, AIP Advances **6** (4), 045103 (2016).
[247] E. Martinez, Journal of Physics: Condensed Matter **24** (2), 024206 (2012).
[248] T. Tanaka, H. Kontani, M. Naito, T. Naito, D. S. Hirashima, K. Yamada and J. Inoue, Physical Review B **77** (16), 165117 (2008).
[249]D. Wu, S. Chen, Z. Zhang, B. Ma and Q. Jin, Applied Physics Letters **103** (24), 242401 (2013).
[250] K.-S. Ryu, S.-H. Yang, L. Thomas and S. S. Parkin, Nature Communications **5** (2014).
[251] T. Shiino, S.-H. Oh, P. M. Haney, S.-W. Lee, G. Go, B.-G. Park and K.-J. Lee, arXiv preprint arXiv:1604.01473 (2016).